Monthly Notices of the ROYAL ASTRONOMICAL SOCIETY

MNRAS **498,** 430–463 (2020) doi:10.1093/mnras/staa2150
Advance Access publication 2020 July 25

The diversity and variability of star formation histories in models of galaxy evolution

Kartheik G. Iyer [1,2★] Sandro Tacchella [3★] Shy Genel,[4,5] Christopher C. Hayward [4] Lars Hernquist,[3] Alyson M. Brooks,[1] Neven Caplar [6] Romeel Davé [7,8,9] Benedikt Diemer [3,10] John C. Forbes,[4] Eric Gawiser,[1] Rachel S. Somerville[1,4] and Tjitske K. Starkenburg[4,11]

[1]*Department of Physics and Astronomy, Rutgers, The State University of New Jersey, 136 Frelinghuysen Road, Piscataway, NJ 08854, USA*
[2]*Dunlap Institute for Astronomy and Astrophysics, University of Toronto, 50 St George Str, Toronto, ON M5S 3H4, Canada*
[3]*Center for Astrophysics, Harvard & Smithsonian, 60 Garden Str, Cambridge, MA 02138, USA*
[4]*Center for Computational Astrophysics, Flatiron Institute, 162 5th Ave, New York, NY 10010, USA*
[5]*Columbia Astrophysics Laboratory, Columbia University, 550 West 120th Str, New York, NY 10027, USA*
[6]*Department of Astrophysical Sciences, Princeton University, 4 Ivy Ln., Princeton, NJ 08544, USA*
[7]*South African Astronomical Observatories, Observatory, Cape Town 7925, South Africa*
[8]*University of the Western Cape, Bellville, Cape Town 7535, South Africa*
[9]*Institute for Astronomy, Royal Observatory, University of Edinburgh, Edinburgh EH9 3HJ, UK*
[10]*NHFP Einstein Fellow, Department of Astronomy, University of Maryland, College Park, MD 20742, USA*
[11]*Department of Physics & Astronomy and CIERA, Northwestern University, 2145 Sheridan Rd., Evanston, IL 60208, USA*

Accepted 2020 July 16. Received 2020 July 14; in original form 2020 May 18

ABSTRACT

Understanding the variability of galaxy star formation histories (SFHs) across a range of time-scales provides insight into the underlying physical processes that regulate star formation within galaxies. We compile the SFHs of galaxies at $z = 0$ from an extensive set of models, ranging from cosmological hydrodynamical simulations (Illustris, IllustrisTNG, Mufasa, Simba, EAGLE), zoom simulations (FIRE-2, g14, and Marvel/Justice League), semi-analytic models (Santa Cruz SAM) and empirical models (UniverseMachine), and quantify the variability of these SFHs on different time-scales using the power spectral density (PSD) formalism. We find that the PSDs are well described by broken power laws, and variability on long time-scales ($\gtrsim$1 Gyr) accounts for most of the power in galaxy SFHs. Most hydrodynamical models show increased variability on shorter time-scales ($\lesssim$300 Myr) with decreasing stellar mass. Quenching can induce $\sim$0.4−1 dex of additional power on time-scales >1 Gyr. The dark matter accretion histories of galaxies have remarkably self-similar PSDs and are coherent with the *in situ* star formation on time-scales >3 Gyr. There is considerable diversity among the different models in their (i) power due to star formation rate variability at a given time-scale, (ii) amount of correlation with adjacent time-scales (PSD slope), (iii) evolution of median PSDs with stellar mass, and (iv) presence and locations of breaks in the PSDs. The PSD framework is a useful space to study the SFHs of galaxies since model predictions vary widely. Observational constraints in this space will help constrain the relative strengths of the physical processes responsible for this variability.

Key words: galaxies: evolution – galaxies: fundamental parameters – galaxies: general – galaxies: statistics – galaxies: star formation.

1 INTRODUCTION

Galaxies in the observable universe show a remarkable diversity in their structure and properties. This diversity can be understood in the context of the many different pathways that exist for galaxies to form stars, grow and eventually cease their star formation ('quench').

The broad features of galaxy assembly have been found to correlate with the assembly of their dark matter haloes (see reviews by Wechsler & Tinker 2018). Galaxy growth can happen through the smooth accretion of gas, through gas-rich and gas-poor mergers, and can be prolonged by inefficient star formation due to turbulence and feedback in the interstellar medium (ISM) and circum-galactic medium (CGM) (White & Rees 1978; Somerville et al. 2008; Tacchella et al. 2018; Behroozi et al. 2019). Galaxy quenching, on the other hand, involves mechanisms that either heat the gas in galaxies or remove it entirely, so that it can no longer form stars. The processes involved in this are thought to be a combination of 'halo quenching', arising from halo gas being shock heated over time, stellar feedback, winds from exploding supernovae, thermal and kinetic feedback from active galactic nuclei (AGNs), as well as external factors such as mergers and interactions (Scannapieco, Silk & Bouwens 2005; Dekel & Birnboim 2006; Kaviraj et al. 2007; Bell 2008; Bundy et al. 2008; Kereš et al. 2009; Kimm et al. 2009; Woo et al. 2012; Weinberger et al. 2017). In between these states, galaxies are affected by the

★ E-mail:kartheik.iyer@dunlap.utoronto.ca (KGI); sandro.tacchella@cfa.harvard.edu (ST)

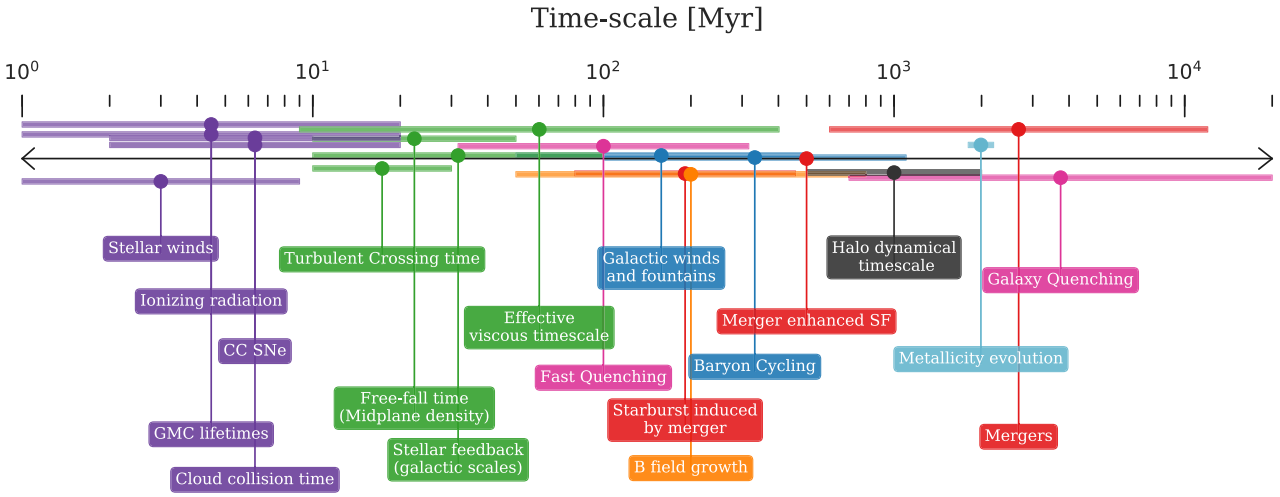

Figure 1. A summary of current estimates in the literature for the time-scales on which different physical processes regulate the growth of galaxies. These time-scales are estimated from theoretical models and simulations of galaxy evolution, with the corresponding references listed in Appendix C. The different colours highlight the different scales and types of physical processes, ranging from processes regulating the creation and destruction of GMCs (purple; Leitherer et al. 1999; Tan 2000; Tasker 2011; Faucher-Giguère 2018; Benincasa et al. 2020), dynamical processes within galaxies (green; Krumholz & Burkert 2010; Forbes et al. 2014b; Hopkins et al. 2014; Semenov, Kravtsov & Gnedin 2017, the cycling of baryons in the ISM and CGM (blue; Marcolini, Brighenti & D'Ercole 2004; Anglés-Alcázar et al. 2017a), the growth of magnetic fields (yellow; Hanasz et al. 2004; Pakmor et al. 2017), metallicity evolution (cyan; Torrey et al. 2018), mergers and merger-induced star formation (red; Robertson et al. 2006b; Jiang et al. 2008; Boylan-Kolchin, Ma & Quataert 2008; Hani et al. 2020), environmental factors (grey; Mo, van den Bosch & White 2010; Lilly et al. 2013), and galaxy quenching (pink; Sales et al. 2015; Nelson et al. 2018b; Rodríguez Montero et al. 2019; Wright et al. 2019). While the figure shows the large range of estimated time-scales for different processes, it also encodes the diversity in the estimated time-scales of individual processes (e.g. quenching time-scales) across different models in the literature. While this is not an exhaustive list of time-scales, it is intended to be a fairly representative subset of the range and diversity in current estimates.

interplay of these different processes and are also found to rejuvenate after periods of relative quiescence (Fang et al. 2012; Pandya et al. 2017).

The spatial and temporal scales involved in these processes differ by several orders of magnitude, and yet all we see in galaxy surveys are their cumulative effects on the entire observable population of galaxies at any given epoch. These processes act over time-scales ranging from <1 Myr to over a Hubble time, and can regulate star formation either locally within a giant molecular cloud or across the entire galaxy. Fig. 1 shows a summary of various physical processes and estimates of the time-scales they are estimated to act upon in contemporary literature at $z \sim 0$. As the figure shows, while different physical processes are estimated to act over characteristic time-scales, they can extend over multiple orders of magnitude and overlap with other processes. This enormously complicates the process of understanding the effect of any individual process on galaxy evolution. Even within a model where it is possible to turn a certain process off or modulate its strengths, the corresponding effects are difficult to generalize, and might change in response to other variables.

Explaining the observed diversity of galaxies today is thus one of the key challenges facing theories of how galaxies form and evolve. Since physical processes regulate star formation over characteristic time-scales, it should be possible to study their effects on galaxy evolution using the imprints they leave on the star formation histories (SFHs) of galaxies. Specifically, studying the variability of galaxy SFHs over different time-scales provides a useful space to quantify and understand the cumulative effects of different processes driving or suppressing star formation on that time-scale. The key open questions can therefore be phrased in terms of SFH variability on different time-scales as follows:

(i) What drives the variability of galaxy SFHs on different time-scales? Do different models of galaxy evolution predict different amounts of variability at a given time-scale?

(ii) Is there a relation between the variability on different time-scales? How does this change as a function of galaxy properties?

This approach towards understanding galaxy evolution through time-scales is particularly informative since the SFHs of galaxies contain a wealth of observationally accessible information about the time-scales of mergers, of bursts of star formation and quenching, baryon cycling and short-time-scale burstiness[1] – relating them to the strengths of AGN and stellar feedback as well as the dark matter accretion histories (DMAHs) of their parent galaxies. This information is encoded in the form of the overall SFH shape, as well as fluctuations on different time-scales. The strength of SFH fluctuations on short time-scales is tied to the formation and destruction of giant molecular clouds (GMCs) due to supernovae explosions, cosmic rays and photoionization feedback (Gnedin, Kravtsov & Chen 2008; Parrish, Quataert & Sharma 2009; Hopkins et al. 2014; Faucher-Giguère 2018; Tacchella, Forbes & Caplar 2020). On intermediate time-scales it is thought to arise from a variety of sources, like mergers, stellar winds, and AGN feedback (Mihos & Hernquist 1994; Thomas & Kauffmann 1999; Di Matteo, Springel & Hernquist 2005; Robertson et al. 2006a; McQuinn et al. 2010; Robaina et al. 2010; Tacchella et al. 2016). On the largest time-scales it is dictated by the behaviour of their parent haloes, and

[1]The term 'burstiness' is loosely used to denote variability in SFR across a range of time-scales in the literature (Weisz et al. 2011b; Guo et al. 2016; Matthee & Schaye 2019; Wang & Lilly 2020b). With this in mind, we preface the term with an appropriate time-scale range whenever used.

by processes like AGN feedback that drive quenching (Scannapieco et al. 2005; Kaviraj et al. 2007; Bell 2008; Kimm et al. 2009; Woo et al. 2012; Bundy et al. 2008; Weinberger et al. 2017; Anglés-Alcázar et al. 2017b). While the longest and shortest time-scales have been extensively studied in theory and have observational constraints, the strength of fluctuations on intermediate time-scales remains of prime interest since they are difficult to constrain observationally and experience contributions from a variety of different processes with overlapping time-scales.

As observations continue to grow in quality, techniques that reconstruct the SFHs from observations are able to extract more robust constraints on the SFHs of individual galaxies and ensembles (Pacifici et al. 2012; Smith & Hayward 2015; Leja et al. 2017; Carnall et al. 2018; Iyer et al. 2019). We now approach the point where we can compare observational distributions of galaxy SFHs to those from simulations to obtain constraints on intermediate-to-long time-scales. Performing this analysis for mass-complete samples across a range of redshifts will allow us to understand and constrain the strengths of the various feedback processes that regulate star formation within and across galaxies.

On shorter time-scales, a multitude of papers study the 'burstiness' of star formation (Weisz et al. 2011b; Domínguez et al. 2015; Sparre et al. 2015; Guo et al. 2016; Sparre et al. 2017; Broussard et al. 2019; Caplar & Tacchella 2019; Emami et al. 2019; Hahn, Tinker & Wetzel 2019a). There exist many definitions for burstiness in the literature, with most using some ratio of H α or UV-based star formation rate (SFR) measurements, which are averaged over time-scales of $\sim$4−10 and $\sim$20–100 Myr, respectively. Comparing distributions of SFRs measured using these two indicators affords a probe of the increase or decrease in the SFR over the recent past, with a distribution therefore affording a statistical view of how the galaxy population is behaving. However, such analysis is extremely difficult due to inherent uncertainties in SFR measurements, assumptions about the monotonicity of SFRs over different time-scales, and degeneracies with a stochastic IMF and dust properties (Johnson et al. 2013; Shivaei et al. 2018). Caplar & Tacchella (2019) undertook an effort to quantify the variability of the SFH on short, intermediate, and long time-scales by constraining the power spectral density (PSD) from the scatter of the star-forming sequence (SFS). Wang & Lilly (2020a, 2020b) complement this by using the PSD formalism to obtain constraints on the ratio of the burstiness of SFRs on 10 Myr to 1 Gyr time-scales using resolved SDSS-IV MaNGA observations.

In this paper, we build on this to establish a framework for understanding the fluctuations in galaxy SFHs using the PSD formalism (Caplar & Tacchella 2019). The PSD at any time-scale is a measure of the amount of power contained in SFR fluctuations on that time-scale, and therefore encodes the variability or 'burstiness' on that time-scale. This provides us with a view of the relative power across different frequencies (and therefore across different time-scales) in a galaxy's SFH, and therefore a first step towards tying the signatures in SFHs to the underlying physical implementations of feedback in the different models. Using this formalism, we compare the SFHs of galaxies across different models, ranging from empirical models to full numerical magnetohydrodynamical (MHD) simulations. This is important towards understanding how the SFHs of galaxies may be affected by the input numerical methods, sub-grid prescriptions, and resolution effects, and can be seen in comparisons between different models that are calibrated to reproduce the same observations. In the current work, we consider five cosmological hydrodynamical simulations (Illustris, Vogelsberger et al. 2014a, b; Genel et al. 2014; Nelson et al. 2015; IllustrisTNG, Mufasa, Davé, Thompson & Hopkins 2016; Marinacci et al. 2018; Naiman et al. 2018; Pillepich et al. 2018b; Springel et al. 2018; Weinberger et al. 2018; Nelson et al. 2019; Simba, Davé et al. 2019; EAGLE, Crain et al. 2015; Schaye et al. 2015; McAlpine et al. 2016), three suites of zoom simulations [FIRE-2, Hopkins et al. 2014, 2018; g14 Governato et al. (2012), Munshi et al. (2013), Brooks & Zolotov (2014) and Marvel/Justice League Munshi et al. in preparation; Bellovary et al. 2019], a semi-analytic model (Santa Cruz SAM, Somerville et al. 2008; Somerville, Popping & Trager 2015; Brennan et al. 2017; Yung et al. 2019) and an empirical model (UniverseMachine, Behroozi, Wechsler & Conroy 2013; Behroozi et al. 2019).

While this paper introduces and applies the PSD formalism to galaxy SFHs from simulations, it is outside the scope of the current work to conclusively correlate PSD features with their underlying physical mechanisms. The main focus of this work lies in comparing PSDs of different models. Future work will examine individual models in more detail and introduce observational constraints in PSD space, using the full extent of observationally recoverable temporal information to validate and constrain theories of galaxy evolution.

Section 2 briefly describes the various models we consider in the current analysis, how we extract SFH information from these models and compute their PSDs. Section 3 presents the SFHs and corresponding PSDs of galaxies from the various models as a function of stellar mass. It also considers the effects of galaxy quenching on PSDs, and the ties between SFHs and the DMAHs of their parent haloes. Section 4 ties the results from this paper to estimates from the current literature of the time-scales on which physical processes affect galaxy growth, and sources of observational constraints in PSD space. We summarize and conclude in Section 5. The appendices provide additional tailored validation tests for the shortest time-scale that can be probed by the PSD of a simulation with a given resolution (Appendix A), plot SFH parameters and covariances at $z \sim 0$ for the various models (Appendix B), and collect references for various time-scales estimated in the literature (Appendix C).

2 DATA SET AND METHODOLOGY

In this section, we set ourselves up to compute the PSDs of galaxy SFHs from different models and provide context for interpreting them. Section 2.1 describes the various models for galaxy evolution we consider in the current analysis. Section 2.2 describes how we extract SFHs from these models, and Section 2.3 describes the PSD and how we compute it. Sections 2.3.1 and 2.3.2 address the problems due to quenching and discrete star particles in computing the PSDs for SFHs from hydrodynamical simulations, with a more detailed forward-modelling approach given in Appendix A.

2.1 Models simulating galaxy evolution

We consider the SFHs from a wide range of galaxy evolution models, ranging from hydrodynamical simulations (Illustris, IllustrisTNG, Mufasa, Simba, EAGLE), a semi-analytic model (Santa-Cruz SAM), an empirical model tuned to match observations across a range of observations (UniverseMachine), and three suites of zoom simulations (FIRE-2, g14 and Marvel/Justice League) with a higher resolution and more explicit prescriptions for the ISM and stellar feedback (see reviews by Somerville & Davé 2015; Vogelsberger et al. 2020, for a summary of the individual components of these various models).

For simplicity, in the current analysis we limit ourselves to (i) considering only a fiducial run from each model, since some models have multiple runs varying the parameters of various sub-grid recipes, (ii) considering the SFHs of only central galaxies above a stellar mass threshold of $10^9 M_\odot$ to partially mitigate resolution effects, and (iii)

Table 1. Details of the various models compared in this paper. The box length for UniverseMachine denotes the subset of the full 250 h^{-1} Mpc box used in the current analysis. The number of galaxies reported is the subset of central galaxies with stellar masses $>10^9 M_\odot$. References for each simulation from which these parameters are taken can be found in Section 2.1. m_{DM} and m_{sp} denote the masses of DM and stellar particles, respectively, at the time of formation. $n_{galaxies}$ is the number of galaxies in our $z = 0$ sample above $M_* \sim 10^9 M_\odot$ used in the current analysis, and $f_{SFR \leq 10^{-3} M_\odot\ yr^{-1}}$ is the fraction of the total sample for which SFR = 0 due to discrete star particles in the hydrodynamical simulations and is set to $10^{-3} M_\odot$ to compute PSDs in log SFR space, and the fraction of time when SFR $< 10^{-3} M_\odot$ for the SAM and empirical model, with SFHs binned in 100 Myr intervals.

Simulation name	Type	Box length (Mpc)	m_{DM} (10^6 $M_\odot$)	m_{sp} (10^6 $M_\odot$)	$n_{galaxies}$ ($M_* > 10^9$ $M_\odot$)	$f_{SFR \leq 10^{-3} M_\odot/yr}$ ($\Delta t = 100$ Myr)
Illustris	Hydro	106.5	6.26	1.26	19354	0.02
IllustrisTNG	Hydro	110.7	7.5	1.4	12220	0.03
Mufasa	Hydro	73.5	96	48	3042	0.18
Simba	Hydro	147	96	18	11300	0.13
EAGLE	Hydro	147.5	9.7	1.81	7482	0.04
Santa-Cruz SAM	SAM	100	203.7	N/A	12821	0.04
UniverseMachine	Empirical	70.3	203.7	N/A	7361	0.05
FIRE-2	Zoom	N/A	$1.3(10^{-3})$–0.28	$2.5(10^{-4})$–$5.6(10^{-2})$	14	0.0
g14	Zoom	N/A	0.126	$8.0(10^{-3})$	8	0.0
MARVEL-ous dwarfs	Zoom	N/A	0.0067	$4.23(10^{-4})$	1	0.0
DC Justice League	Zoom	N/A	0.042	$8.0(10^{-3})$	4	0.0

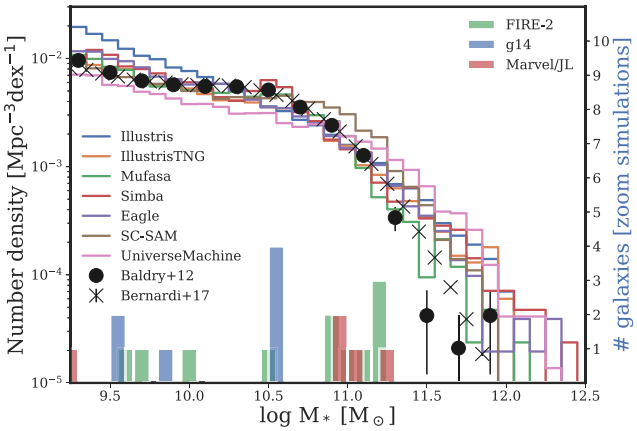

Figure 2. The stellar mass function of $z \sim 0$ galaxies from the large-volume models we consider: Illustris, IllustrisTNG, Mufasa, Simba, EAGLE, the Santa Cruz semi-analytic model, and UniverseMachine. The black points with error bars provide a comparison to observations. The solid histograms in the bottom and the corresponding y-axis on the right show the distribution of stellar masses for the 14 galaxies from FIRE-2 (green), 8 galaxies from g14 (blue), and 5 galaxies from Marvel/Justice League (red) that we consider.

studying galaxies at $z \sim 0$, with model variants and redshift evolution to be considered in further work. Fig. 2 shows the normalized distributions of stellar mass for galaxies from each model at $z \sim 0$, used in the current analysis. The FIRE-2, g14, and Marvel/JL zoom simulations have a much smaller sample of 14, 8, and 5 galaxies, respectively, spanning a range of stellar masses from $\sim 10^9 M_\odot$ to $\sim 10^{11.5} M_\odot$. While these zoom simulations allow us to probe SFH fluctuations to shorter time-scales compared to the large-volume models due to their much finer spatiotemporal resolution, which allows them to resolve GMC-scale structures and treat feedback more explicitly, these galaxies are not representative of a cosmological sample. Caution should therefore be employed in generalizing trends in their variability.

Each model of galaxy evolution is described briefly below, with references to relevant papers containing more detailed descriptions. Since the current analysis deals with galaxy SFHs, the descriptions focus on how each simulation implements star formation and feedback, and Table 1 contains a summary of the resolution, box size, and number of galaxies from each simulation:

(i) **Illustris** (Genel et al. 2014; Vogelsberger et al. 2014b): The Illustris project[2] is a large-scale hydrodynamical simulation of galaxy formation using the moving mesh code AREPO (Springel 2010). The model includes recipes for primordial and metal-line cooling, stellar evolution and feedback, gas recycling, chemical enrichment, supermassive black hole (BH) growth, and AGN feedback (Springel & Hernquist 2003; Vogelsberger et al. 2013). Given the spatial resolution of $\simeq 1$ kpc, giant molecular clouds are not resolved. A sub-resolution model for an effective equation of state (Springel & Hernquist 2003) is implemented where a star particle is stochastically produced above the critical hydrogen number density of $n_{SF} = 0.13$ cm^{-3} on a density-dependent time-scale that reproduces the observed Kennicutt–Schmidt relation (Schmidt 1959; Kennicutt 1989). Star formation results in supernovae, which release kinetic winds that expel gas from their surroundings and chemically enrich the ISM. These winds are implemented by launching hydrodynamically decoupled 'wind particles' that recouple to the gas when they leave the dense local ISM and reach a cell with a density $<0.05 n_{SF}$ (Springel & Hernquist 2003; Pillepich et al. 2018b). This results in a non-local coupling of the stellar wind feedback to the gas in contrast to the local feedback from AGN. Feedback from AGN can be either thermal or kinetic, following the model of Springel, Di Matteo & Hernquist (2005) and Sijacki et al. (2007). Galaxies in the simulation are quenched primarily due to radio mode feedback from AGN, with an expanding jet-induced bubble transferring energy from the BH to the halo and heating the gas. Parameters of the Illustris model have been chosen to roughly reproduce the cosmic star formation rate density (SFRD), and the galaxy stellar mass function (SMF), the stellar mass–halo mass relation (SMHM), and the stellar mass–black hole mass relation (SMBH) at $z = 0$.

(ii) **IllustrisTNG** (Weinberger et al. 2017; Pillepich et al. 2018b): A significantly updated version of the original Illustris project, IllustrisTNG[3] carries over recipes for star formation and evolution, chemical enrichment, cooling, feedback with outflows, growth and multimode feedback from Illustris with substantial updates

[2] https://www.illustris-project.org/
[3] https://www.tng-project.org/

(Weinberger et al. 2017; Nelson et al. 2018a; Pillepich et al. 2018b). In addition to this, it incorporates new black hole driven kinetic feedback at low accretion rates, magnetohydrodynamics, and improvements to the numerical scheme. Unlike Illustris, TNG injects winds isotropically with a modified wind speed that depends on the local 1D dark matter (DM) velocity dispersion, with a redshift dependence that matches the growth of the virial halo mass. AGN feedback is modelled using two modes: a pure thermal mode at high accretion rate (quasar mode) and a pure kinetic mode at low accretion rate (radio mode), with a kinetic wind feedback model (Weinberger et al. 2017) responsible for quenching galaxies (Weinberger et al. 2018). In addition to the observations used with Illustris, the TNG simulation parameters are also chosen to reproduce galaxy sizes and halo gas fractions at $z = 0$. In the current work, we use the TNG100 simulation as described in Pillepich et al. (2018b) and Weinberger et al. (2018).

(iii) **Mufasa** (Davé et al. 2016): The Mufasa meshless hydrodynamic simulations use the GIZMO code (Hopkins 2015), prescriptions for cooling and heating with Grackle (Smith et al. 2017), and star formation and feedback from massive stars using scalings from FIRE (Hopkins et al. 2014; Muratov et al. 2015). Star formation is implemented stochastically from gas particles using the Krumholz, McKee & Tumlinson (2009) formalism to estimate the H_2 formation at coarse resolution accounting for sub-grid clumping. Then, for densities $\geq$0.13 cm^{-3}, stars are formed stochastically over local dynamical time-scales ($t_{\rm dyn} = 1/\sqrt{G\rho}$) with $\sim$ 2 per cent efficiency, following Kennicutt (1989). Sub-grid recipes for feedback from massive stars launch two-phase winds that drive material out of galaxies through a combination of type-II supernovae, radiation pressure, and stellar winds. These winds are parametrized using a mass loading factor and wind speed, and scaling relations for these parameters based on galaxy properties are adopted from the FIRE simulations (Muratov et al. 2015) instead of being tuned to reproduce observations. Since Mufasa does not explicitly model AGN, quenching is accomplished by keeping all the gas in massive haloes heated (except gas that is self-shielded) to reproduce the effects of 'maintenance mode' feedback from long lived and AGB stars (Gabor & Davé 2015). Parameters in Mufasa have been chosen to reproduce the galaxy SMF at $z = 0$.

(iv) **Simba** (Davé et al. 2019): The Simba cosmological galaxy formation simulations are built on the Mufasa simulations including black hole growth and feedback, using the GIZMO cosmological gravity+hydrodynamics code with its meshless finite mass (MFM) solver (Hopkins 2014, 2017). Similar to Mufasa, Simba uses a stochastic H_2 based star formation model, with the SFR given by the H_2 density divided by the local dynamical time-scale. Simba also uses two-phase winds with updated mass loading factor scalings from FIRE (Anglés-Alcázar et al. 2017a), which is similar to those adopted by IllustrisTNG but with slightly lower wind velocities. Simba implements a torque limited BH accretion model along with a kinetic subgrid model for BH feedback similar to Anglés-Alcázar et al. (2017b), but with a variable outflow velocity. Wind particles are decoupled for a short amount of time ($10^{-4}\tau_{\rm H}$, where $\tau_{\rm H}$ is the Hubble time) from hydrodynamics and radiative cooling. The BH feedback is overall similar to the two-mode model in IllustrisTNG, with some differences detailed in Davé et al. (2019). The majority of galaxy quenching occurs due to the AGN jet mode feedback, with a bimodal distribution of quenching time-scales found in Rodríguez Montero et al. (2019). Parameters in the Simba model have been chosen to reproduce the $M_{\rm BH}$–σ relation and the galaxy SMF at $z = 0$.

(v) **EAGLE** (Crain et al. 2015; Schaller et al. 2015; Schaye et al. 2015; McAlpine et al. 2016): The Evolution and Assembly of GaLaxies and their Environments (EAGLE)[4] is a set of cosmological hydrodynamic simulations of galaxy formation using a modified version of the Tree-PM smoothed particle hydrodynamics (SPH) code GADGET-3 (Springel 2005). EAGLE does not resolve molecular clouds for accurate modelling of the warm gas within galaxies and implements sub-grid recipes for stellar evolution, cooling, and heating of gas due to stars and other emission, metal enrichment of ISM gas and energy injection due supernovae, and the formation, accretion and feedback of AGN. Star formation occurs via gas particles that are stochastically converted into star particles at a pressure-dependent rate that reproduces the observed Kennicutt–Schmidt law (Schaye & Dalla Vecchia 2008). A metallicity-dependent density threshold (Crain et al. 2015) is adopted to ensure that star formation happens in cold, dense gas. The local ISM is heated stochastically due to feedback from massive stars and supernovae with a fixed temperature increment (Dalla Vecchia & Schaye 2012). At high SFR, this feedback can lead to large-scale galactic outflows (Crain et al. 2015). Similar to feedback from star formation, AGN feedback is implemented using a single-mode thermal feedback model. The fraction of radiated energy that couples to the ISM is calibrated to reproduce the stellar mass-black hole mass relation at $z = 0$, and mimics the 'radio'- and 'quasar'-like modes depending on the BH accretion rate (Crain et al. 2015). Quenching is thought to happen on long time-scales ($\sim$3–4 Gyr) for low-mass central galaxies due to stellar feedback, and high-mass centrals on shorter time-scales due to AGN feedback and environmental quenching (Trayford et al. 2016; Wright et al. 2019). Parameters in the EAGLE suite are chosen to reproduce the galaxy SMF at $z = 0.1$ and the disc galaxy size–mass relation.

(vi) **Santa-Cruz SAM** (Somerville et al. 2008; Porter et al. 2014; Somerville et al. 2015; Brennan et al. 2017): The Santa-Cruz Semi-Analytic Model contains a number of well-motivated semi-analytic prescriptions for the hierarchical growth of structure, gas heating and cooling, star formation and stellar evolution, supernova feedback and its effect on the ISM and ICM, AGN feedback, starbursts and morphological transformations due to mergers and disc instabilities that are used in conjunction with the Bolshoi–Planck (Klypin, Trujillo-Gomez & Primack 2011; Rodríguez-Puebla et al. 2016; Klypin et al. 2016) dark matter simulation merger trees to construct populations of galaxies that are tuned to match observations at $z = 0$. The model implements two modes of star formation: a 'normal' disc mode following the Schmidt–Kennicutt relation, along with exploding supernovae which drive outflows with recycling that occurs in isolated discs, and a 'starburst' mode that occurs as a result of a merger or internal disc instability. The SAM implements a multiphase gas model for the ISM. Cold gas can be ejected from galaxies by winds driven by SN feedback. Heated gas is either trapped within the DM halo potential well, or ejected from the halo into the diffuse IGM. Brennan et al. (2017) and Somerville & Davé (2015) find that virial shock heating due to massive haloes alone is not enough to quench massive galaxies, with a significant role played by feedback from AGN activity, driven by galaxy mergers or *in situ* processes like disc instabilities. Model parameters such as the strengths of stellar and AGN feedback are calibrated using the observed SMF at $z = 0$, with further details in Porter et al. (2014).

(vii) **UniverseMachine** (Behroozi et al. 2013, 2019): The UniverseMachine is an empirical model that determines the SFRs of galaxies as a function of their host haloes' potential well depths, assembly histories, and redshifts. The model uses halo properties and assembly histories from the Bolshoi–Planck dark matter simu-

[4] http://icc.dur.ac.uk/Eagle/

lation (Klypin et al. 2011, 2016; Rodríguez-Puebla et al. 2017) in conjunction with a variety of observational constraints including the cosmic SFRD, observed SMFs, specific SFR functions, quenched fractions, UV luminosity functions, UV-stellar mass relations, IRX-UV relations, autocorrelation and cross-correlation functions, and the dependence of quenching on environment across $0 < z < 10$ to constrain its free parameters (see table 1 in Behroozi et al. 2019). SFRs are parametrized in terms of redshift and halo properties, with the list of parameters in table 2 of Behroozi et al. (2019), which include the scatter in the SFRs of star-forming galaxies, a model for the SFR–$v_{M,\,\mathrm{peak}}$ relation,[5] quenched fraction properties and random errors in measuring stellar masses and SFRs. The parameters are tuned using Markov Chain Monte Carlo optimization to match the observational constraints. In the current analysis we use SFHs from the public Data Release 1 of UniverseMachine.

(viii) **FIRE-2** (Hopkins et al. 2018): The Feedback In Realistic Environments (FIRE)[6] simulations considers a fully explicit treatment of the multiphase ISM and stellar feedback. The simulations in this work are specifically part of the 'FIRE-2' version of the code; all details of the methods are described in Hopkins et al. (2018), Section 2. The simulations use the code GIZMO (Hopkins 2015),[7] with hydrodynamics solved using the mesh-free Lagrangian Godunov 'MFM' method. Gas dynamics and radiative cooling from a meta-galactic background and local sources are incorporated using tabulated cooling rates from CLOUDY (Ferland et al. 2017). Stars form by stochastically turning gas particles into stellar particles in dense, self-shielding molecular, self-gravitating regions above a density threshold. The stellar feedback prescription includes radiation pressure from massive stars, local photoionization and multi-wavelength photoelectric heating, core-collapse and type Ia supernovae with appropriate momentum and thermal energy injection, and stellar winds. The FIRE physics, source code, and all numerical parameters are identical to those in Hopkins et al. (2018). The higher resolution of the FIRE simulations resolves the ISM to a larger extent than the large-volume simulations. Hopkins et al. 2014 find that supernova feedback alone is not enough, radiative feedback (photo-heating and radiation pressure) is needed to destroy GMCs and enable efficient coupling of later supernovae to gas. Multiple feedback mechanisms are also responsible for regulating the ISM: supernovae regulate stellar masses/winds; stellar mass-loss fuels late star formation; radiative feedback suppresses accretion on to dwarfs and instantaneous star formation in discs. Feedback from supermassive black holes is not included in the simulations (Hopkins et al. 2018). While there are approximations for the momentum and energy deposition from SNe when the cooling radius is not resolved, the simulations are not explicitly tuned.

(ix) **g14** (Governato et al. 2012; Munshi et al. 2013; Brooks & Zolotov 2014; Brooks & Christensen 2016; Christensen et al. 2016, 2018; Brooks et al. 2017): The g14 suite of cosmological zoom simulations are run using the *N*-body+SPH code Gasoline (Wadsley, Stadel & Quinn 2004) within a *WMAP*3 cosmology. The galaxies are chosen to have a range of merger histories and spin values. The g14 simulations follow the non-equilibrium formation and destruction of molecular hydrogen, and allow stars to form in the presence of H_2, with resolution high enough to resolve the disks of galaxies and the GMCs in which stars form Christensen et al. (2012). Stars are born with a Kroupa, Tout & Gilmore (1993) IMF, mass and metals are returned in stellar winds as star particles evolve and SN Ia and II return thermal energy to the surrounding gas (see Stinson et al. 2006 for details). For SN II, 10^{51} erg of energy are injected per SN. Metal diffusion occurs in the ISM (Shen, Wadsley & Stinson 2010), and a cosmic UV background is included following Haardt & Madau (1996). The g14 suite was calibrated to match the SMHM relation of Moster, Naab & White (2013).

(x) **Marvel/Justice League** (Munshi et al. in preparation; Bellovary et al. 2019): The Marvel/Justice League simulations are run using ChaNGa (Menon et al. 2015), the successor to Gasoline. The MARVEL-ous dwarfs (henceforth Marvel) are a sample of field dwarfs (4–11 Mpc from a Milky Way-mass galaxy) at 65 pc force resolution, while the DC Justice League (henceforth JL) are zooms of MW-mass disc galaxies and their surrounding environments at 170 pc resolution. Many of the physics modules in ChaNGa remain the same as in Gasoline, such as the star formation and stellar feedback schemes, with the exception that 1.5×10^{51} erg of thermal energy is injected per SN II. This increase is motivated by the fact that ChaNGa contains an improved implementation of Kelvin–Helmholtz instabilities compared to Gasoline (Wadsley, Keller & Quinn 2017), which leads to more efficient accretion on to the disc. An updated UV background is adopted based on Haardt & Madau (2012). In addition, supermassive black hole growth and feedback is implemented using the models described in Tremmel et al. (2017). Parameters in the simulations were calibrated to reproduce the SMHM, SMBH, and SFRs of galaxies at $z = 0$.

2.2 Extracting SFHs

We compute SFHs for each galaxy in the hydrodynamical simulations under consideration (Illustris, IllustrisTNG, Mufasa, Simba, EAGLE, FIRE-2, g14, and Marvel/Justice League) by performing a mass-weighted binning of the star particles with $\Delta t = 100$ Myr. The choice of time bin is further explored in Section 2.3.1. For models where we only have access to the masses of the star particles at the time of observation, we account for mass-loss using the FSPS (Conroy, Gunn & White 2009; Conroy & Gunn 2010) stellar population synthesis code, adopting the initial mass function (IMF) of the stellar particles in the simulation. In this procedure, we consider all stellar particles belonging to a galaxy at $z \sim 0$ instead of tracing the gas-phase SFR as a function of time. The reason for this is twofold: (i) since the hydrodynamical simulations trace the times when star particles were formed, this gives us finer time-resolution than the snapshots saved for the different simulations, (ii) since the SFHs we observationally reconstruct are the sum over all the progenitors, this archaeological approach therefore allows us to compare directly with observations. Both UniverseMachine and the Santa Cruz SAM track the SFR for each galaxy, so we simply interpolate these to match the same time grid with 100 Myr steps as the hydrodynamical simulations. In both cases, the resolution is fine enough that the interpolation does not need to up-sample the SFR. Since the UniverseMachine SFHs are stored in terms of scale factor instead of absolute time, an additional periodogram is computed using the uneven spacing to check that the PSDs are not significantly affected by the interpolation. Additional fine-resolution SFHs are also computed for the galaxies from the zoom simulations, with a time-step $\Delta t = 1$ Myr.

Since the SFHs span a large dynamic range, we work in log SFR space in order to be able to better quantify the relative strengths of SFR fluctuations. Analysing the SFHs in linear SFR space effectively amounts to a different weighting scheme. This choice is

[5]Where $v_{M,\,\mathrm{peak}}$ is the maximum circular velocity of the halo at peak halo mass.
[6]http://fire.northwestern.edu
[7]http://www.tapir.caltech.edu/~phopkins/Site/GIZMO.html

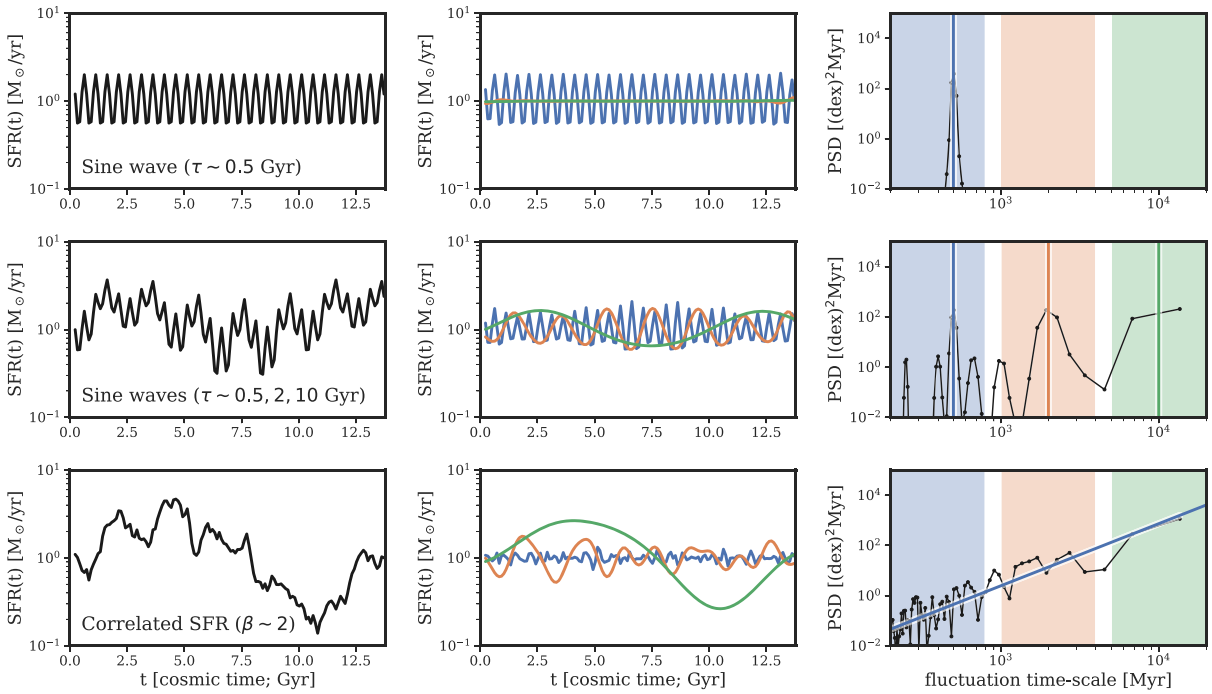

Figure 3. Illustrating the PSD computation using three example SFHs. Top: A simple sine wave with a time-scale of 500 Myr; middle row: a combination of three sine waves, with time-scales: 500 Myr, 2 Gyr, and 10 Gyr; and bottom: a stochastic SFH with a spectral slope of $\beta = 2$. Left: The individual galaxy SFHs, in log SFR space. Middle column: SFH fluctuations on short, intermediate, and long time-scales isolated using a band-pass filter in Fourier space – the green curves show the power arising due to the long time-scales (>4 Gyr), orange curves show the power contribution from intermediate time-scales (1–3 Gyr) and blue from relatively shorter time-scales (<0.9 Gyr). Right: The PSD (black lines) corresponding to each SFH from the left-hand panels, while the three coloured ranges correspond to the band-passes used to isolate the Fourier modes in the middle panel. The PSD in each band pass is proportional to the net strength of the fluctuations contained in the coloured curves from the middle column averaged over all phases. For the sine wave, the PSD is well localized at a single frequency. With multiple sine waves, it is harder to separate the contributions from individual components. For a stochastic process with spectral slope $\beta \sim 2$, the power is distributed across a range of time-scales.

motivated by physical considerations, since the SFRs of star-forming galaxies are often found to be distributed normally in log SFR space, with a tail towards low SFRs from passive galaxies that do not have ongoing star formation (Feldmann 2017; Caplar & Tacchella 2019; Hahn et al. 2019b).

2.3 The power spectral density

The variability or 'burstiness' of galaxy SFRs is a topic of much interest, and has been studied in a variety of ways – using burstiness indicators based on the time-scales of different SFR tracers (Guo et al. 2016; Broussard et al. 2019; Emami et al. 2019), fitting an exponential to the Pearson correlation coefficient of SFRs as a function of time-separation to quantify an 'SFR evolution time-scale' (Torrey et al. 2018), quantifying the scatter in SFRs smoothing on different time-scales (Hopkins et al. 2014; Matthee & Schaye 2019), using power spectral densities (PSDs) to quantify the variability in Fourier space (Caplar & Tacchella 2019; Wang & Lilly 2020b, a), or performing a PCA decomposition of SFHs to get estimate the fraction of variance accounted for by different time-scales (Matthee & Schaye 2019). In other studies involving time series data, the structure function (Hughes, Aller & Aller 1992; MacLeod et al. 2010; Kozłowski 2016; Caplar, Lilly & Trakhtenbrot 2017) has also been used as a metric to quantify variability on different time-scales in quasar and AGN studies.

In the current analysis, we choose to quantify the variability of galaxy SFHs using the PSD formalism, since

(i) the PSD formalism is well studied and easily interpretable, and Fourier space provides an excellent domain to quantify and compare the variability of SFHs across different time-scales;

(ii) the decomposition of variability into different frequencies, and therefore different time-scales, allows us to understand the relative contribution to the overall burstiness from each time-scale. This takes us one step closer towards relating this variability to the underlying physical processes responsible; and

(iii) evolving analysis techniques coupled with upcoming observational data sets will make it possible to obtain observational constraints in PSD space.

For a continuous time series $\psi(t)$, the PSD is defined in terms of the Fourier transform $f(k) = \int \mathrm{d}t\, \mathrm{e}^{-ikt} \psi(t)$ as $\mathrm{PSD}(k) = |f(k)|^2$. In practice, we compute the PSD for each SFH using Welch's method (Welch 1967), implemented in the `scipy.signal.welch` module.

The PSD corresponding to the SFH for an individual galaxy reports a phase-averaged estimate of the strength of SFR fluctuations at a given frequency.[8]

For a sinusoidal signal with a frequency ν, the corresponding PSD is given by a delta function at the frequency ν, shown in the top panel of Fig. 3. Generalized to more complicated time series, the PSD therefore provides a way to disentangle and interpret the strength of the fluctuations on different time-scales, as previously done in studies of AGN variability and theoretically with SFHs (MacLeod

[8]Or, inverting it, at a given time-scale.

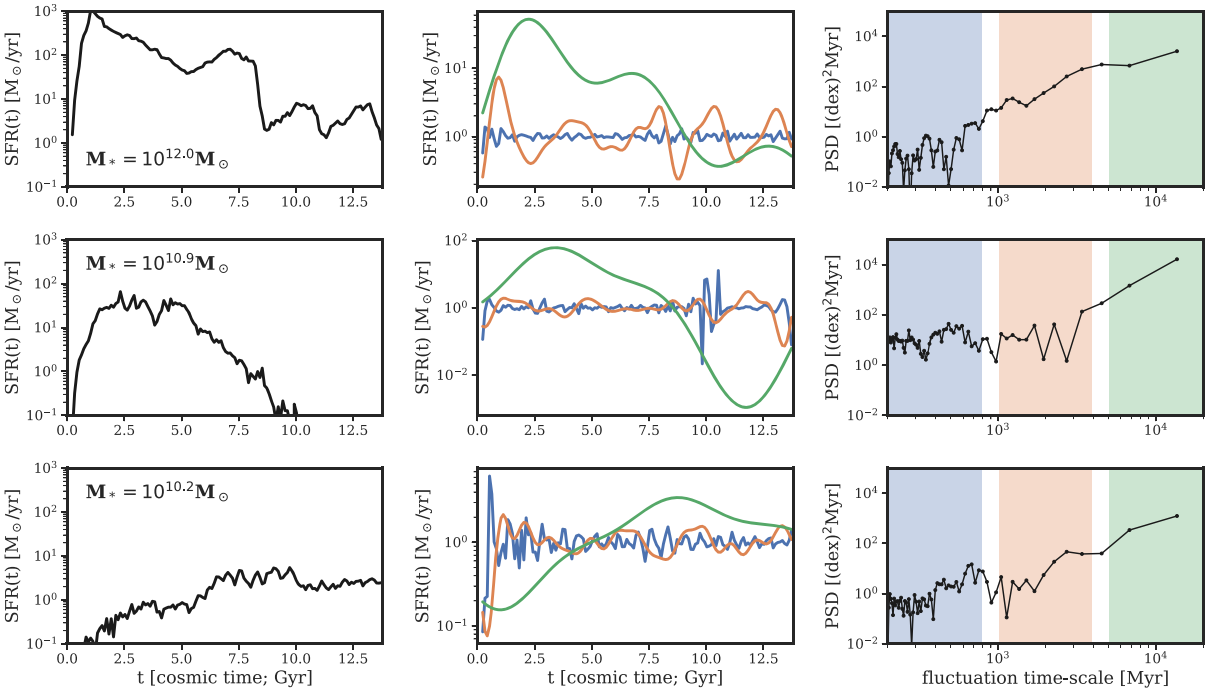

Figure 4. Similar to Fig. 3, showing the (PSD) computation using three galaxies from the IllustrisTNG simulation. Top row: A green-valley galaxy; middle row: a quiescent galaxy with no star formation in the last ∼3 Gyr; and bottom row: an actively star-forming galaxy building up its stellar mass. Left column: The individual galaxy SFHs, obtained by binning mass-weighted star particles in 100 Myr bins. Middle column: Log SFR fluctuations on short, intermediate, and long time-scales isolated using a band-pass filter in Fourier space – the long time-scales contain the most power and capture the overall shape of the SFH, while the shorter time-scales capture fluctuations around it. Right column: The black line shows the full PSD, and the integral of the coloured curves in the middle columns sets the strength of the PSD in the corresponding coloured time-scale ranges. As seen in the middle panel, overall trends in the SFH can be described by the contribution from the longest time-scales, similar to the stochastic process in Fig. 3. However, depending on the shape of the SFH, the distribution of power on shorter time-scales can change significantly.

et al. 2010, 2012; Caplar et al. 2017; Sartori et al. 2018; Caplar & Tacchella 2019). A sharp peak in the PSD would indicate strong SFR fluctuations at a given time-scale, possibly driven by a physical process. However, physical processes acting over a range of time-scales spread out the peaks and make it more difficult to isolate the effects of individual processes. An example of this is shown in the middle column of Fig. 3, where the sum of three sinusoidal curves produces three peaks in the PSD, along with additional artefacts due to the finite length of the time series. Processes like hierarchical structure formation and correlated stochastic star formation additionally link short time-scales to longer ones, creating an overall spectral slope to the PSD, shown in the bottom panel of Fig. 3. Physical processes can additionally drive features at certain characteristic time-scales; for example, the regulator model (Lilly et al. 2013, see also Bouché et al. 2010; Davé, Finlator & Oppenheimer 2012; Forbes et al. 2014b) predicts SFHs correlated below an equilibrium time-scale of a galaxy's gas reservoir, with the slope at time-scales below the break steeper by 2 than the slope above it (Tacchella et al. 2020; Wang & Lilly 2020a). Such features can be seen as breaks in the PSD (Caplar & Tacchella 2019). The PSDs of galaxy SFHs therefore contain a wealth of information about the different physical processes responsible for its shape.

Examples of this procedure are shown in Fig. 4, which shows SFHs for galaxies from the IllustrisTNG simulation (left column) as well as their corresponding PSDs (right column). The contribution to the PSDs at three different time-scales due to the strength of SFH fluctuations are highlighted in different colours in the middle panels. Unlike the case for the sine wave, the power in these PSDs is spread over a large dynamic range, indicative of the stochastic nature of star formation and the wide range of time-scales over which physical processes in galaxies induce variability in the SFRs. With a thorough understanding of a galaxy's evolution and merger history, it might be possible to interpret its individual PSD. However, in the current work we focus on studying the broader trends in a sample of galaxy SFHs and their corresponding PSDs as a way to compare different models of galaxy evolution on the same footing. In doing so, we examine the variability of galaxy SFHs on intermediate (∼200 Myr) to long (∼10 Gyr) time-scales, and study the evolution in the PSDs as a function of stellar mass and star forming state (star forming versus quiescent). We choose stellar mass since it is a good tracer for the overall state of a galaxy, correlating well with a wide range of other physical properties including halo mass, SFR, metallicity and BH mass, and can be calculated self-consistently for all the models directly from the SFHs after accounting for mass-loss.

2.3.1 *Choosing a minimum time interval and SFR = 0*

In choosing the Δt for our time bins, we need to consider the effects of the discreteness of individual star particles, since the SFR will be zero in bins that do not contain any star particles. This effect is particularly important for low-mass galaxies, where the number of star particles is $\mathcal{O}(10^2 - 10^3)$ depending on the model resolution. If not accounted for, these bins lead to shot-noise in log SFR space, biasing the computed PSDs. We avoid this by increasing the size of the time bins until the fraction of our data with SFR $= 0$ is significantly reduced. We also verified that the PSDs at time-scales longer than our adopted bin size Δt are insensitive to the choice of binning. In practice, we find that with time bins of 100 Myr,

the percentage of bins where SFR = 0 is ∼ 3–6 per cent across the various models. The only notable exceptions are Mufasa and Simba, which have poorer resolution. The fraction of the total SFRs that are $\leq 10^{-3}\mathrm{M}_{\odot}\ \mathrm{yr}^{-1}$ for each model are given in Table 1. Finally, we set values of SFR = 0 to SFR = $\mathrm{SFR}_{\mathrm{min}} = 10^{-3}\mathrm{M}_{\odot}\ \mathrm{yr}^{-1}$ for a given model to avoid values of $-\infty$ in the PSD computation. We tested the procedure to ensure that this does not significantly affect the PSDs of quiescent galaxies by broadening the time-bins (increasing Δt) to reduce the number of bins with SFR = 0 and comparing the PSDs for longer time-scales. An example of the PSD for a fully quenched galaxy can be seen in the middle row of Fig. 4, which shows the SFH for a single quenched galaxy from IllustrisTNG.

2.3.2 *Shot-noise due to discrete star particles*

In the hydrodynamical simulations we consider, gas is turned into a star particle probabilistically, depending on whether certain temperature and/or density conditions are met. This introduces a $\mathcal{O}(1)$ fluctuation in a given time bin (width Δt) based on whether the $N + 1^{\mathrm{th}}$ star particle is created. In log SFR space, the sudden conversion of a gas particle into a star particle creates large fluctuations when the SFR is low, i.e. there are only a few star particles in a given time bin. To avoid this, we only consider the portion of the PSD on time-scales ($\Delta t > \Delta t_{\mathrm{min}}$) that are large enough that there are enough star particles in a bin to minimize the effects of discrete star particles.

Since we are working with log SFR, the biggest fluctuations due to discrete star particles will be in bins that contain $\mathcal{O}(1)$ star particle. Given a galaxy with mass M_* and resolution such that a star particle is of mass m_{sp}, this effect becomes more likely when the number of time bins ($\tau_{\mathrm{H}}/\Delta t$) is comparable to the number of star particles. Therefore, we would like to avoid the limit $M_*/m_{\mathrm{sp}} \lesssim \tau_{\mathrm{H}}/\Delta t$. For a simulation with resolution m_{sp}, we therefore require: $\Delta t \gg \tau_{\mathrm{H}} m_{\mathrm{sp}}/M_*$. For a galaxy with $M_* \sim 10^{10}\mathrm{M}_{\odot}$, with resolution $m_{\mathrm{sp}} \sim 10^{6}\mathrm{M}_{\odot}$, this means that the time-bin width at $z \sim 0$ has to be $\gg$1.3 Myr.

However, this is significantly complicated by the fact that the SFHs of galaxies tend to rise and fall, which means that star particles are not uniformly distributed across time. Moreover, an $\mathcal{O}(1)$ fluctuation causes different contributions depending on what the SFR is in a given bin. To account for all of these effects, we forward-model the contribution of discrete star particles in Appendix A, by creating realistic SFHs corresponding to various stellar masses and then discretizing them to match the resolution of the models we consider. We then compute the power spectra of the true and discretized SFHs, to determine the lowest time-scales to which we can accurately probe the PSD at a given resolution and stellar mass. The PSDs below these thresholds have been shown as dashed black lines in Section 3.1. In practice, this means that to probe fluctuations on time-scales below 1 Gyr, we need galaxies that have a stellar mass of at least $10^{8.5}$, $10^{8.6}$, $10^{9.9}$, $10^{9.5}$, and $10^{8.7}\mathrm{M}_{\odot}$ for Illustris, IllustrisTNG, Mufasa, Simba, and Eagle, respectively. As we go to shorter time-scales the threshold goes up, e.g. to probe fluctuations below 300 Myr, the minimum stellar mass of galaxies needed is $10^{10.1}$, $10^{10.1}$, $10^{11.0}$, $10^{10.7}$, and $10^{10.2}\mathrm{M}_{\odot}$, respectively.

Having established the procedures for extracting SFHs from the various models and studying them in PSD space, we now look at the PSDs of galaxies across the different models.

3 STAR-FORMATION DIVERSITY AND VARIABILITY IN DIFFERENT MODELS

The variabilities of galaxy SFHs on different time-scales are linked to the underlying processes that regulate star formation across galaxies. The strength of this variability, i.e. the amount of power in the PSD at a given time-scale is therefore a useful constraint regarding the cumulative effect of all the processes that contribute to the PSD at that time-scale. Since the shapes of the SFHs are intimately linked by scaling relations to the other physical properties of galaxies like stellar mass, environment and morphology (Kauffmann et al. 2003; Whitaker et al. 2014; Iyer et al. 2019; Tacchella et al. 2019), understanding the link between SFHs and the power on different time-scales acts as a step towards linking these properties to the underlying physical processes responsible.

For all the models, Section 3.1 reports the median SFHs and PSDs in bins of stellar mass, and examines their characteristics. Sections 3.2 compares the diversity of SFHs predicted by the different models we consider, while Section 3.3 examines the diversity in the PSDs on particular time-scales of interest. Section 3.4 looks at the difference in the PSDs based on whether galaxies are actively star-forming or quiescent. Finally, the relation between galaxy SFHs and the DMAHs of their parent haloes is studied in Section 3.5.

3.1 Variability in the different models at $z = 0$

3.1.1 *Large-volume simulations*

In Figs 5–7, we show the SFHs and corresponding PSDs for galaxies binned in intervals of stellar mass for the Illustris, IllustrisTNG, Mufasa, Simba, and EAGLE hydrodynamical simulations, the Santa-Cruz semi-analytic model, and the UniverseMachine empirical model. Binning in stellar mass allows us to study the coherent features in the PSDs of similar demographics of galaxies across the various models. In a given mass bin, we plot the median SFH and median PSD; the median PSD is obtained from the PSDs of individual SFHs (i.e. not from the median SFH). We see that there is a large amount of diversity in both the SFHs and the PSDs of galaxies from the various models, although some broad trends can be observed. Overall, the SFHs of galaxies tend to rise and fall (Pacifici et al. 2012, 2016), with this behaviour accentuated as we go to higher stellar masses where the fraction of quenched galaxies is higher (Peng et al. 2010; Whitaker et al. 2014; Schreiber et al. 2015). The times at which the median SFHs in a given mass bin peak and the rate at which they fall differ widely across the different models. For example, the median SFHs for MW-like galaxies ($\mathrm{M}_* \sim 10^{10.5}\mathrm{M}_{\odot}$) peak at epochs ranging from $z \sim 1.75$ ($t = 3.8$ Gyr) for IllustrisTNG to $z \sim 0.75$ ($t = 7.1$ Gyr) for UniverseMachine, with the other models falling somewhere in between. $10^{9}\mathrm{M}_{\odot}$ galaxies in IllustrisTNG and UniverseMachine do not appear to fall on average, contrasted with the decline observed for the EAGLE and SC-SAM models. Due to the coarser resolution of Mufasa and Simba, we are unable to probe this mass range.

For all the models, the PSDs generally rise towards longer time-scales, i.e. the dominant contribution to the overall shape of the SFH comes from fluctuations on the longest time-scales. More massive galaxies show a slight increase in the overall normalization. This increase in power on the longest time-scales traces the increasing contribution on long time-scales from quenched galaxies at higher stellar masses, and is discussed further in Section 3.4.

The PSDs can locally be described using a power-law, with the slopes varying across the models and also within models as a function of stellar mass and time-scale. For the median PSDs, the spectral slopes range between $\beta \sim 0$ to $\beta \sim 4$, where the former implies that the strength of fluctuations on adjacent time-scales are uncorrelated, while the latter implies that the strength of fluctuations on adjacent time-scales are highly correlated. Similar to the PSD power, the slope generally rises towards higher masses and longer time-scales. In conjunction with the SFHs, we see that this is tied to the quenching

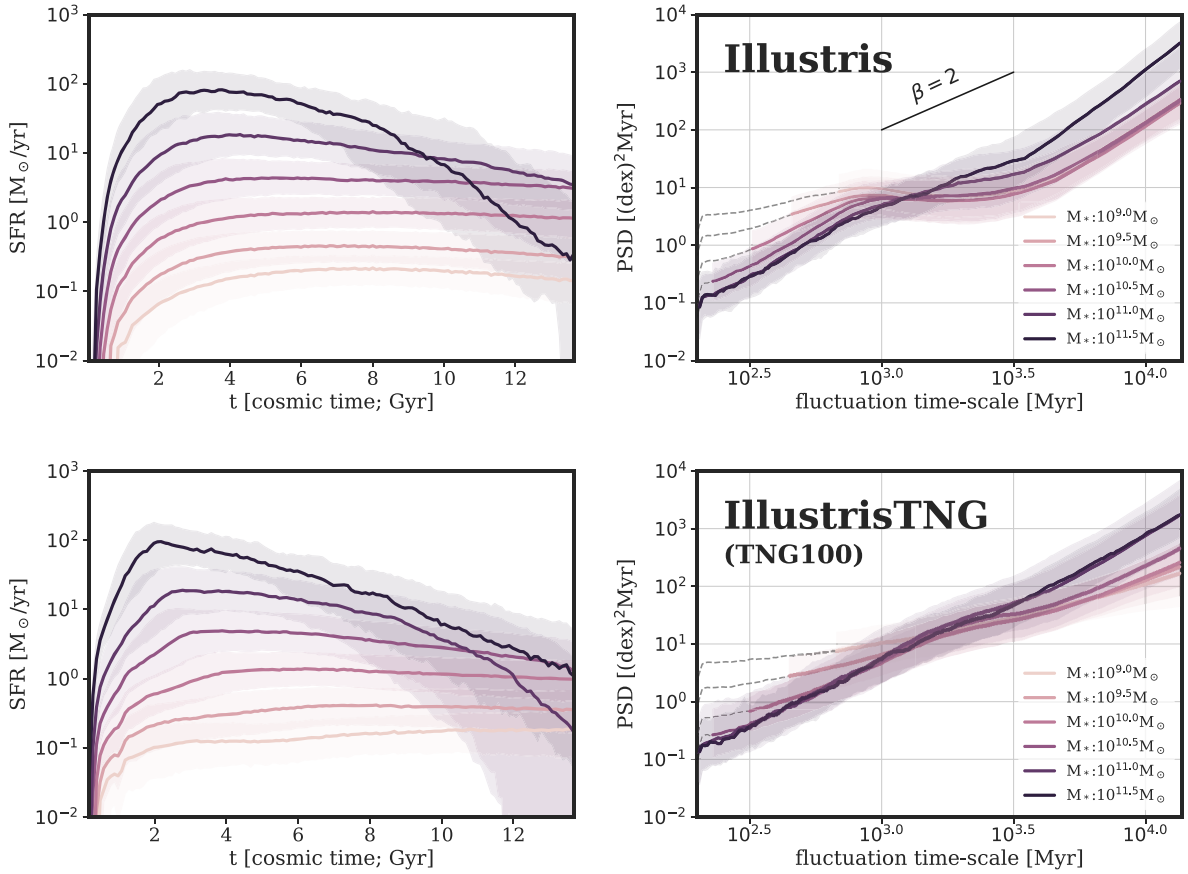

Figure 5. The median SFHs (SFHs; left) and corresponding power spectral densities (PSDs; right) of galaxies from the Illustris and IllustrisTNG cosmological hydrodynamical simulations, shown here in 0.5 dex bins of stellar mass, centred on the values given in the legend. PSDs are computed from individual SFHs prior to taking the median. The shaded regions show the 16th-84th percentile of the distribution in a given mass bin at each point in time (left) and fluctuation time-scale (right). Dashed lines indicate regions where shot-noise due to discrete star particles may contaminate the PSDs according to our validation tests (see Appendix A). The PSDs of low- and intermediate-mass galaxies in Illustris and IllustrisTNG show a break at 1–2 Gyr (more prominent in Illustris than IllustrisTNG), which disappears in higher mass galaxies, i.e. the PSD of the most massive galaxies is nearly scale-free.

of galaxies, which selectively adds power on longer time-scales, leading to an increase in the long-time-scale slope. This can also be seen comparing the bottom to the middle panel of Fig. 4. We discuss this in more detail in Section 3.4.

Apart from these overall similarities, the PSDs and corresponding SFHs display a lot of variety across the various models, with Mufasa and Simba showing greater variability on short time-scales compared to Illustris, IllustrisTNG, EAGLE, Santa Cruz SAM, and UniverseMachine. For the most massive galaxies, this corresponds to a nearly 1 dex increase in the power on ∼200 Myr time-scales.

A possible concern is that this effect is in part due to resolution effects, since Mufasa and Simba star particles are ∼10× those of Illustris, IllustrisTNG, and EAGLE. While our forward-modelling of shot-noise accounts for this, we also consider the PSDs of three different IllustrisTNG runs with varying resolution in Section 4.3 that shows that while there is a slight increase in the power on short time-scales due to poorer resolution, this is an actual phenomenon due to the galaxies evolving differently and quenching faster, as evidenced by the difference in their median SFHs. In addition, the increase is not enough to completely account for the higher power found in Mufasa and Simba (∼0.5 dex due to resolution versus the ∼1 dex difference between the shortest time-scales for the most massive Mufasa/Simba and IllustrisTNG galaxies).

There are several notable breaks in the PSDs for particular models. In general, we see that the breaks generally decrease in strength towards higher stellar masses, tending to resemble an overall scale-free PSD with slope $\beta \sim 2$. The time-scales and number of breaks can vary significantly across the different models, and are briefly summarized below.

(i) Illustris has two breaks – an intermediate-time-scale break around ∼0.6−1 Gyr and a longer time-scale ∼2.6–4.2 Gyr time-scales. These breaks are prominent at low and intermediate stellar masses. For the most massive galaxies, the breaks nearly disappear and the PSD is close to scale free.

(ii) The breaks in IllustrisTNG are similar to the breaks in Illustris, but overall less pronounced. Furthermore, the break at ∼0.6–1 Gyr in Illustris moves to longer time-scales (∼1.1–2.6 Gyr) in IllustrisTNG. Again, the PSD becomes nearly scale-free at $M_* > 10^{11}\mathrm{M}_\odot$.

(iii) Both Mufasa and Simba have no clear breaks, and instead show a gradual increase in PSD slope from $\beta \sim 0$ to $\beta \sim 2$ towards longer time-scales. The highest mass bin in Mufasa shows a slight peak at ∼300 Myr time-scales. Above ∼3 Gyr, the slopes in Mufasa stabilize at a constant value, and slopes in Simba approach $\beta \sim 2$.

(iv) The PSDs in EAGLE show a smooth increase in slope similar to Mufasa. This increase in slope continues till ∼3 Gyr time-scales, beyond which the PSD slopes stay constant.

(v) The Santa-Cruz SAM has a clear break at low and intermediate masses: the break time-scale increases from ∼400–600 Myr to ∼1–

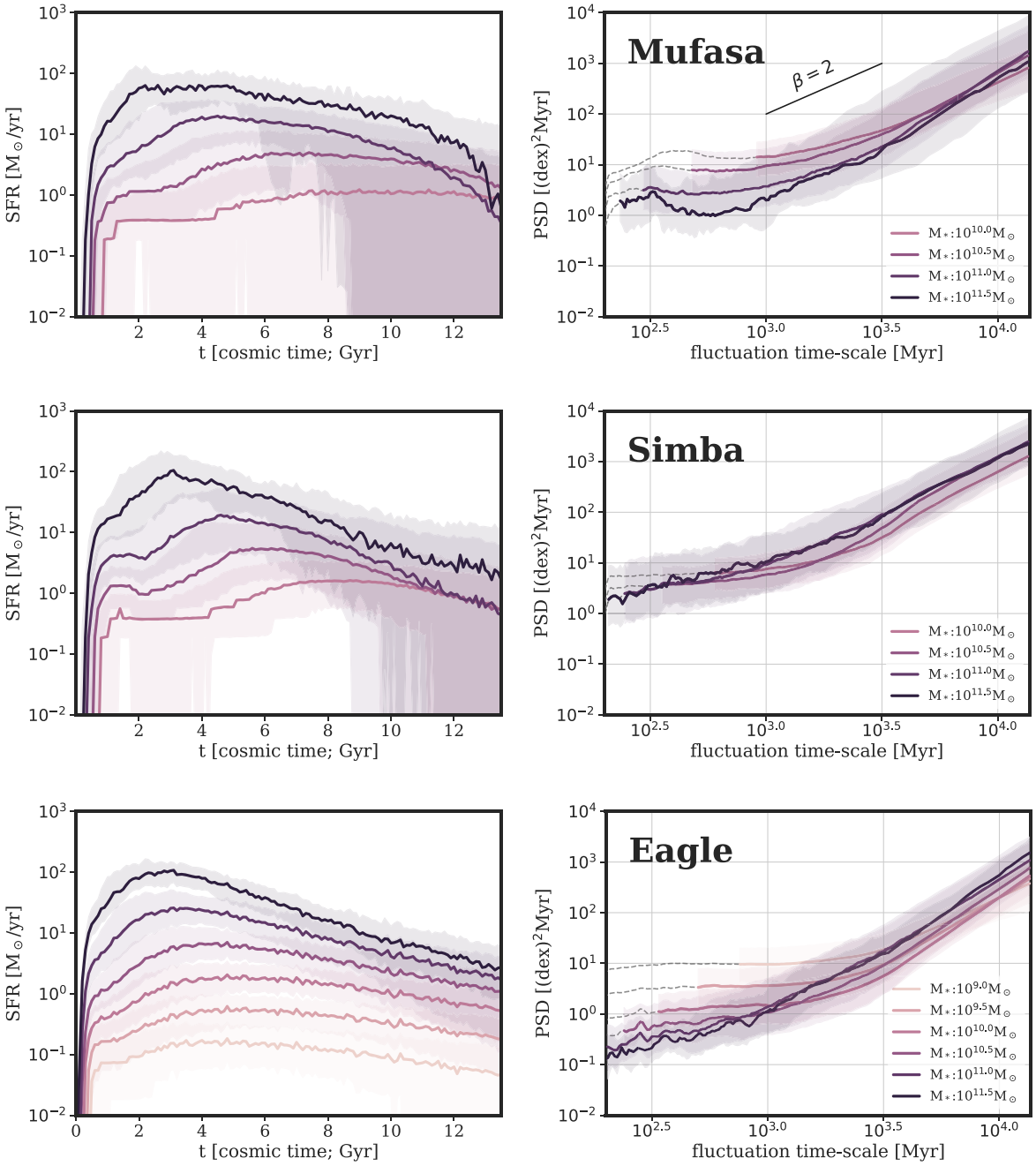

Figure 6. Same as Fig. 5, but for the Mufasa, Simba and EAGLE cosmological hydrodynamical simulations. Due to the lower resolution of the Mufasa and Simba simulations, we only show galaxies with $M_* > 10^{10}\mathrm{M}_\odot$. The PSDs of these simulations show a smoothly increasing PSD slope towards longer time-scales; that is, they show less significant breaks than PSDs in Illustris and IllustrisTNG.

1.6 Gyr from $M_* \sim 10^9\mathrm{M}_\odot$ to $M_* \sim 10^{10.5}\mathrm{M}_\odot$. At $M_* \sim 10^{11}\mathrm{M}_\odot$, the PSD is nearly scale free. For the most massive galaxies, the PSDs resemble those of Simba and EAGLE, showing a smooth increase in slope towards long time-scales.

(vi) UniverseMachine shows the least variation in slope compared to the other models, with $\beta \in (1, 2.5)$. It also contains a break at ∼1.5–3 Gyr, where the slope decreases with time-scale, followed by a shallower break over ∼3–10 Gyr where it rises again towards longer time-scales (similar to IllustrisTNG). The break decreases in strength slightly with increasing stellar mass, and is probably tied to the inferred quenching behaviour learned from tying halo accretion to observed galaxy properties.

3.1.2 Zoom simulations

In addition to the large-volume models, the FIRE-2, g14, and Marvel/Justice League suites of zoom simulations, with star particles of $10^2-10^4\mathrm{M}_\odot$, allow us to (i) test the effect of much finer spatiotemporal resolution that enables the simulations to resolve GMC-scale structures and treat feedback more explicitly compared to the large-volume simulations and (ii) probe specific parts of the PSD parameter space (e.g. shorter time-scales) that are not accessible at present with large-volume cosmological models.

In Fig. 8, we show the PSDs of 14 galaxies in FIRE-2, 8 galaxies in g14, and 5 galaxies in Marvel/JL that have $M_* > 10^9\mathrm{M}_\odot$. All the

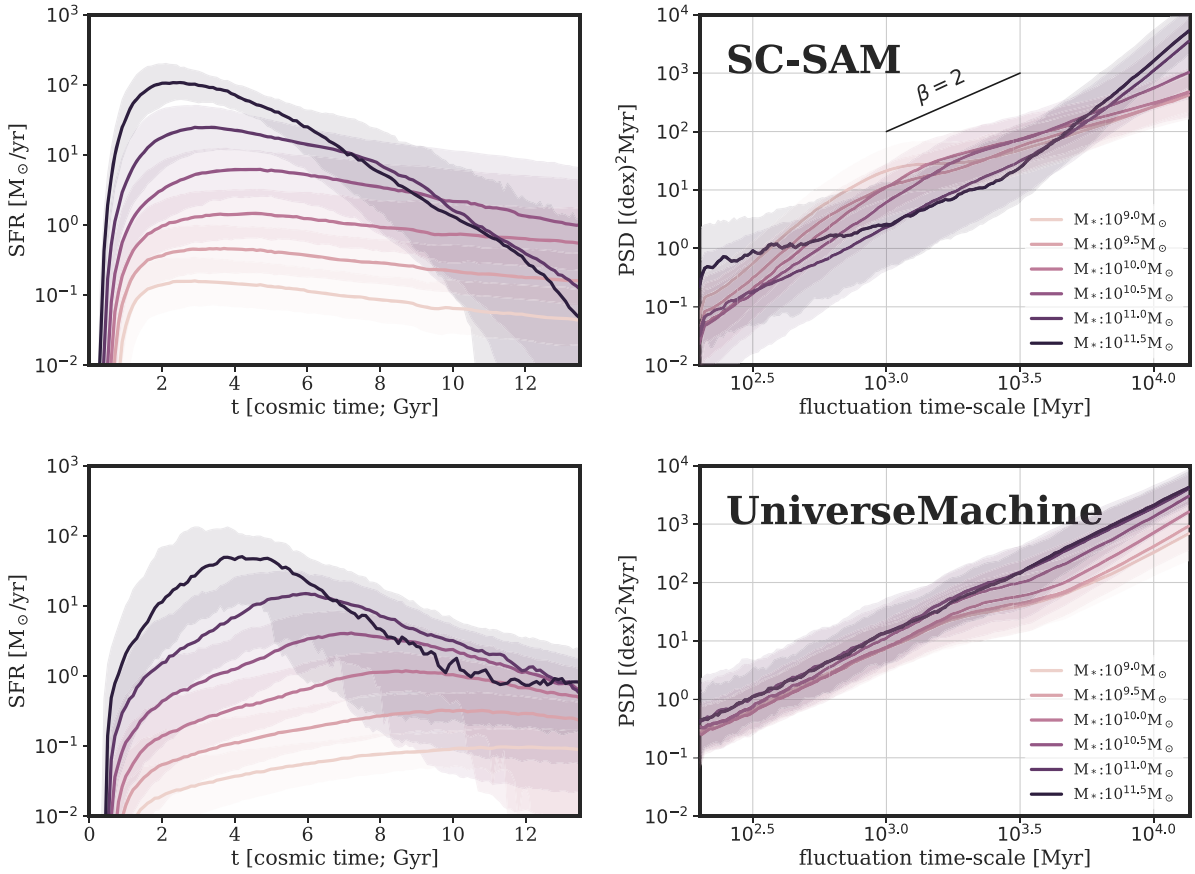

Figure 7. Same as Fig. 5, but for the Santa Cruz semi-analytic model and the UniverseMachine empirical model. Tying galaxy SFRs to the DMAHs of their parent haloes without explicit prescriptions for dynamical processes in UniverseMachine manifests as a lack of features in the PSDs that is similar to IllustrisTNG at long time-scales and high stellar masses.

zoom simulations agree qualitatively with each other: the PSD is roughly constant between a time-scale of ∼300 Myr to 2−3 Gyr and then increases towards longer time-scales. Furthermore, the power around 1 Gyr increases towards lower masses in all three simulations, consistent with the idea that lower mass galaxies have burstier star formation than higher mass galaxies. Quantitatively, the zoom simulations show a few differences: galaxies in g14 and Marvel/Justice League show less power on shorter time-scales compared to FIRE-2 at a given stellar mass, indicating that they are less bursty in general. However, they show a stronger trend of increasing burstiness (i.e. power on shorter time-scales) with decreasing stellar mass.

This behaviour of increasing power on short time-scales towards lower mass galaxies can also been seen in the large-volume models like Illustris, IllustrisTNG, EAGLE, and Mufasa. However, the presence of shot-noise at short-time-scale ($\lesssim$300 Myr) portions of the PSDs makes this conclusion more difficult to draw. FIRE-2 shows a higher contribution to the power from shorter time-scales compared to most large-volume simulations, with uniformly high power at all time-scales $\lesssim$ 3 Gyr that is comparable to Mufasa and Simba.

In Fig. 9, we show the PSDs of six individual galaxies from the three zoom suites – h277 from g14 (Zolotov et al. 2012; Loebman et al. 2014; O'Shaughnessy et al. 2017), Sandra from Justice League, Rogue from Marvel (Munshi et al. in preparation; Bellovary et al. 2019), and m11q, m12f, and m12m from FIRE-2 (Hopkins et al. 2018). m12m is a an early-forming halo hosting an MW-mass galaxy, and is closest in stellar mass to Sandra, and has a similar overall shape for the SFH. m12f is a MW-like galaxy. h277 is an MW analogue with no major mergers since $z = 3$. Rogue and m11q are both SMC-mass dwarfs. More information about these galaxies and their physical properties can be found in the cited papers.

The increased resolution of the zoom simulations allow us to probe the PSDs down to much shorter time-scales (∼10 Myr) than currently possible with the large-volume models. The bottom panel of Fig. 9 provides our first view of the PSD of simulated galaxies down to these time-scales. We find the following:

(i) The broken power-law behaviour found in the PSDs on longer time-scales continues down to the time-scales of ∼10−30 Myr.

(ii) On short time-scales, the PSDs show a slope of $\beta \sim 1-2$, with FIRE-2 tending towards a shallower slope with more overall power, consistent with increased burstiness.

(iii) On time-scales ∼100−300 Myr, some PSDs show distinct peaks (h277 and Rogue). The absence of major mergers could play a part in setting the strength of this peak for h277 since h258, a similar g14 galaxy with a more active merger history does not display such a prominent peak and instead shows an elevated PSD overall.

(iv) On time-scales of ∼0.2−1 Gyr, the PSDs flatten out ($\beta \sim 0$), before converging to a power law with slope $\beta \sim 2-3$ on long time-scales.

(v) The slopes of the FIRE-2 galaxies are generally shallower and have less power compared to galaxies in g14 and Marvel/Justice League.

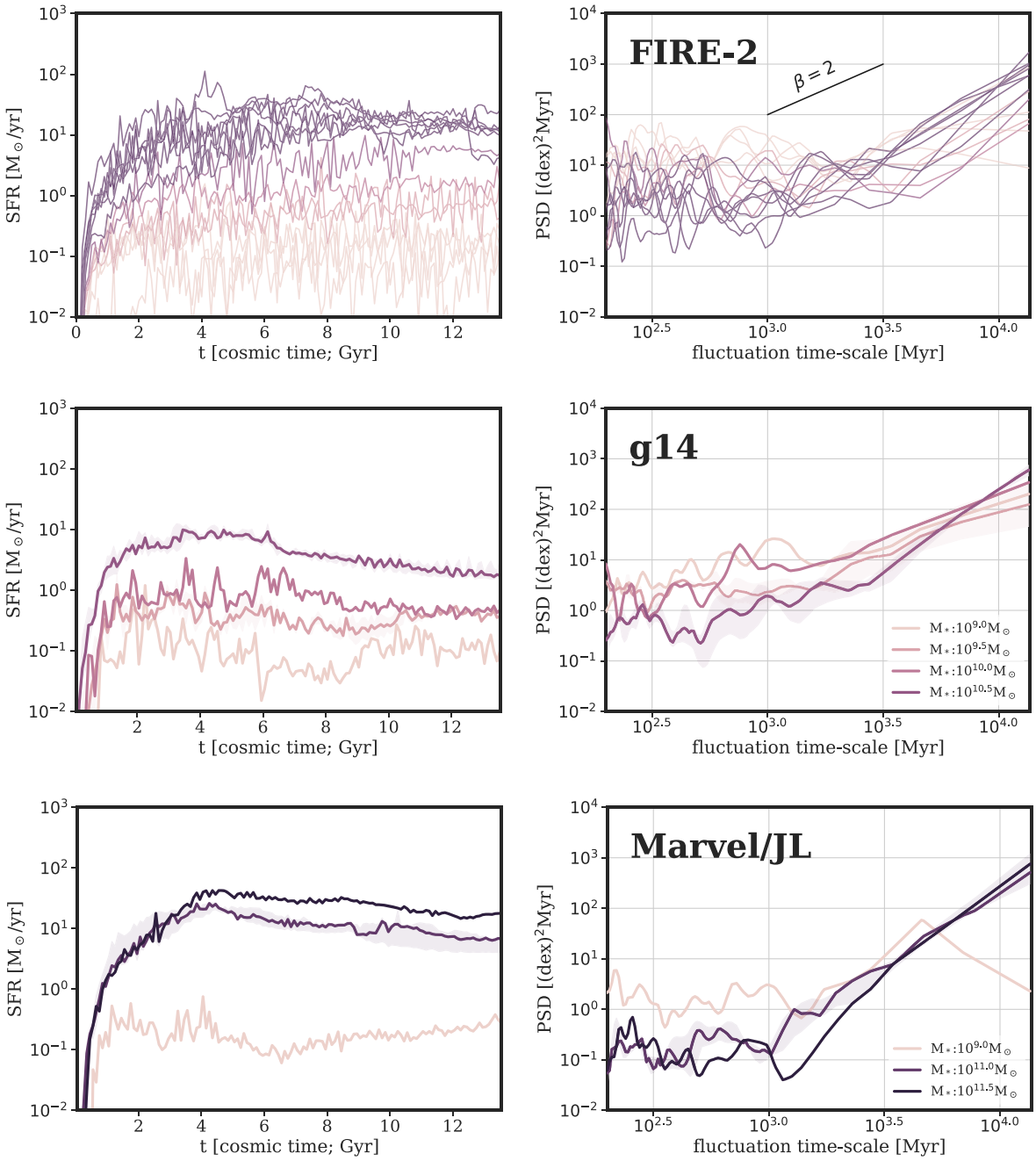

Figure 8. Same as Fig. 5, but for smaller samples of galaxies from the FIRE-2 and g14 and Marvel/Justice League zoom hydrodynamical simulations. The FIRE-2 galaxies exhibit higher values of PSD at short time-scales compared to the other models. The g14 and Marvel/Justice League simulation shows lesser power on shorter time-scales than FIRE-2 at a given mass. In addition, there is a stronger trend of increasing variability on shorter time-scales as we go to lower masses.

(vi) Overall, lower mass galaxies like m11q and Rogue can sometimes display considerably higher power than their higher mass counterparts on time-scales $\lesssim$6 Gyr, in keeping with the trend of increasing burstiness with decreasing stellar mass.

The rich PSDs of these zoom simulations provide an excellent data set to test and validate theories that connect physical processes to features in the PSDs. Specifically, these short time-scales (<100 Myr) probe the gas cycle within galaxies, including the formation and disruption of star-forming clouds (Faucher-Giguère 2018; Jeffreson & Kruijssen 2018; Kruijssen et al. 2019). Therefore, we might be able to use the PSD on these time-scales to constrain the lifecycle of star-forming clouds (Tacchella et al. 2020). Furthermore, the PSD is accessible from observations, since SFRs estimated from H α and the UV can allow us to constrain the slope of the PSD in this regime (Caplar & Tacchella 2019).

3.2 The diversity in SFH shapes

In this section, we study how the different models deviate from the overall sample behaviour (and from each other) by quantifying the overall SFH diversity as a function of time and stellar mass. We

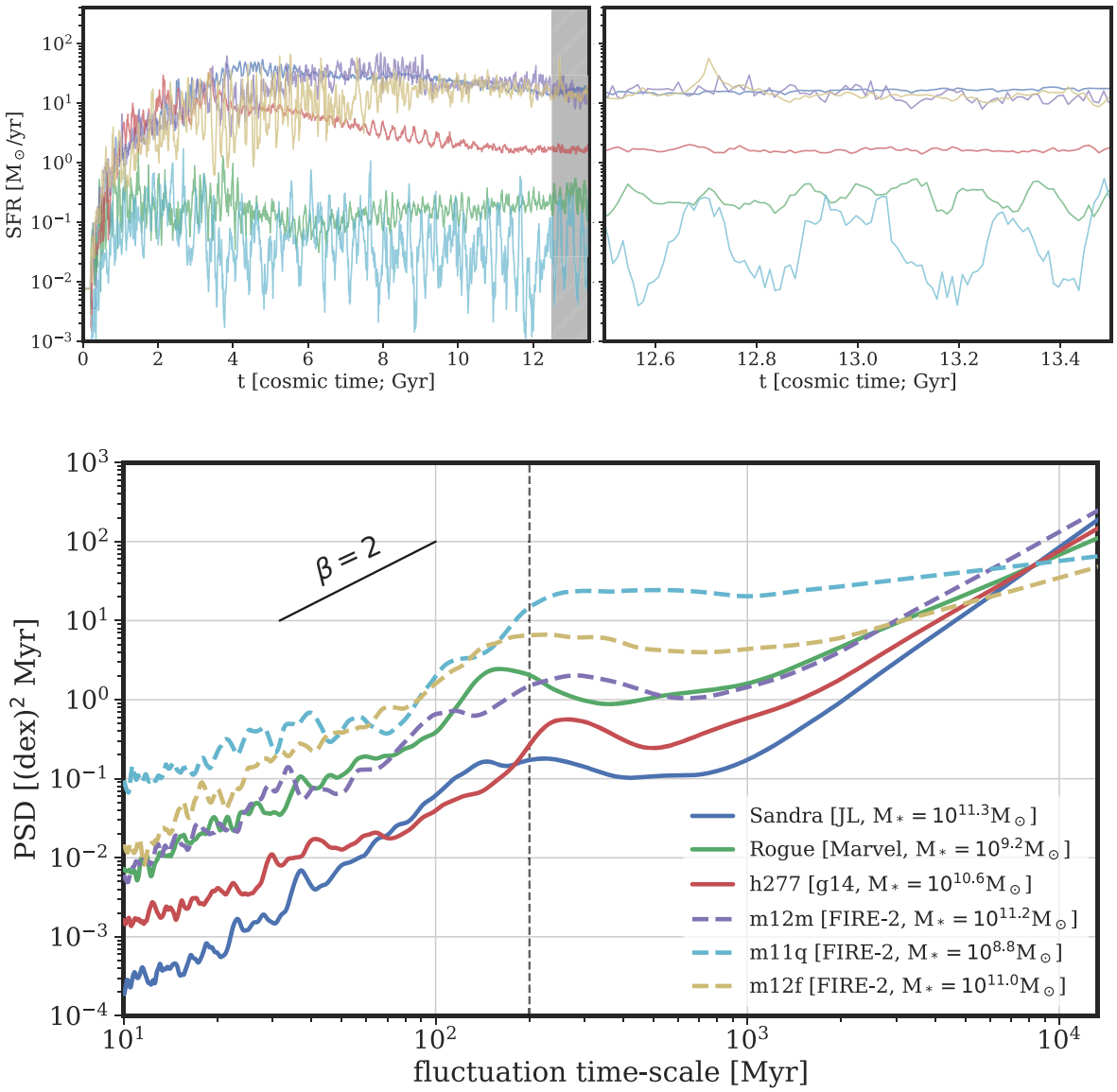

Figure 9. The much finer resolution of galaxies from the zoom simulations allows us to probe the PSDs of individual galaxy SFHs to much finer time-scales than the large-volume models. We compute the PSDs for individual galaxies from the g14 (h277), Marvel (Rogue), JL (Sandra), and FIRE-2 (m12m – closest in stellar mass to Sandra, m11q – an SMC-mass dwarf, m12f – an MW-like halo) suites of zoom simulations. The top panels show the full galaxy SFHs (left) and the SFHs over a period of 1 Gyr (right), corresponding to the shaded region in the left-hand panel. The bottom panel shows the corresponding PSDs. The vertical dashed line in the PSD plot shows the shortest time-scales we probe with the large-volume simulations in Figs 5–7, an order of magnitude above what is possible with the zoom simulations. The overall slope of the PSDs continues down to shorter time-scales, with the FIRE-2 galaxies showing more power on short time-scales compared to the g14 and Marvel/JL galaxies. The PSDs of Rogue and h277 show a notable excess in the PSD at ∼100−300 Myr time-scales, while Sandra, m12m and m12f appear to show broader, less-prominent peaks spread over a longer range of time-scales (∼60−200 Myr). m12f and m11q display a break in the PSD at ∼100 Myr time-scales, with a flattening of the PSD beyond that. Several galaxies also show distinct temporal dependence on variability, with m12f showing increased burstiness at earlier epochs, and Rogue showing oscillatory features at $t = 7-10$ Gyr.

compute the median SFH in a given mass bin for individual models and compare it to the median SFH in a given mass bin across all the models. To account for the differing number of galaxies in a given mass bin across the different models, we randomly sample 1000 SFHs with replacement from the available SFHs at each step of the calculation. We repeat this sampling and calculation 100 times to adequately capture small (∼0.02−0.1 dex) fluctuations due to random seeds.

The result is shown in Fig. 10, which shows the difference between the median SFHs in different bins of stellar mass. It should be noted that the median SFH across all models is not the 'correct' SFH, but merely a guide to the eye. Therefore, instead of comparing the deviation from the median for any given model, it is more instructive to (i) look at the differences between the models themselves, and (ii) use the median to get an idea of the overall variance among models at a given mass and epoch (shown as shaded grey regions). Although there is a considerable diversity across the different models, the largest differences occur when the SFR is low – at early epochs when galaxies are beginning to assemble their mass and when they are quenching. A locus of agreement across the various models exists in each mass bin, moving to higher redshifts with increasing mass. This is correlated with the epoch when the median SFHs peak in

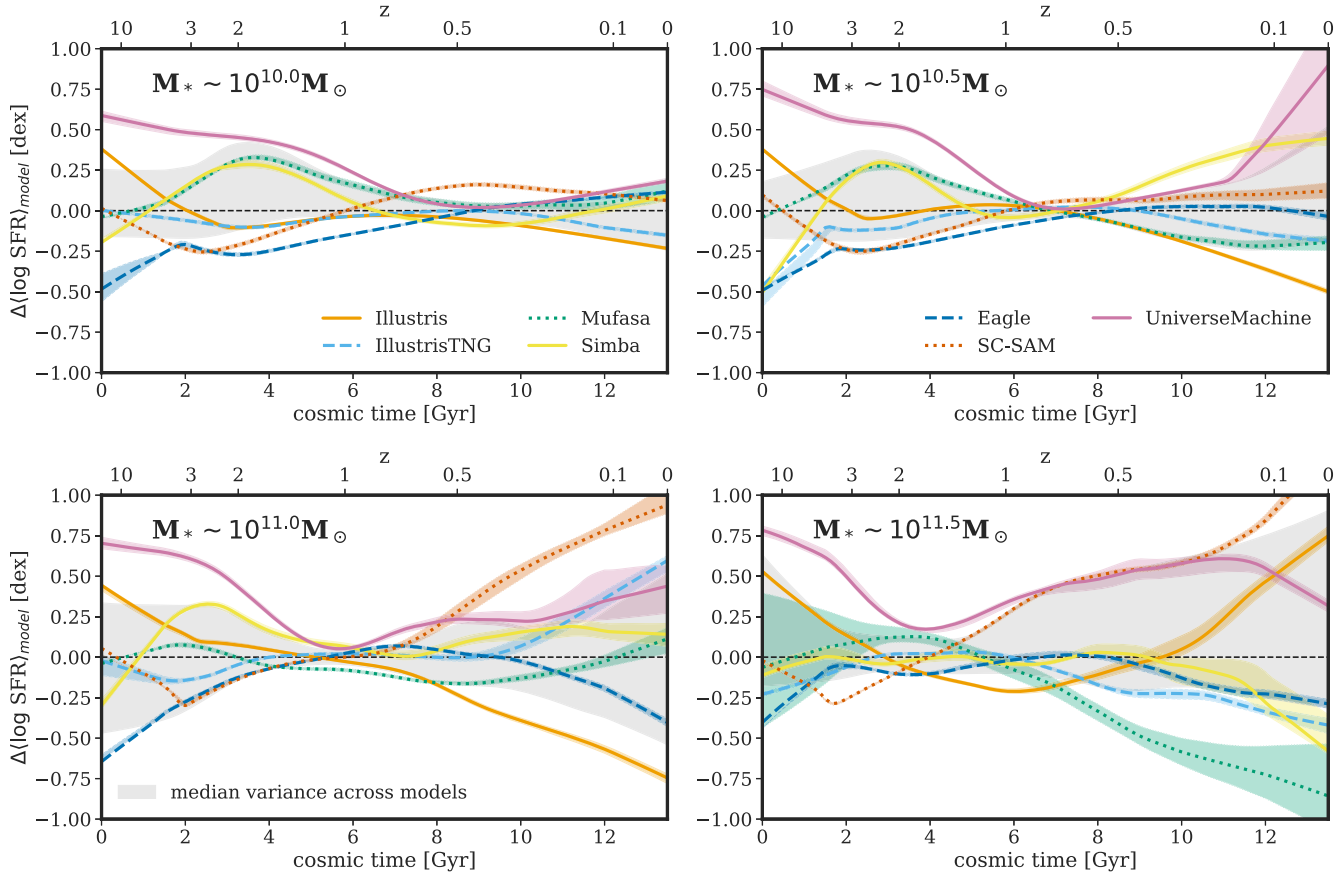

Figure 10. The diversity in the median SFHs for the different models. The dashed black line at 0 dex corresponds to the median SFH of all galaxies in that mass bin across all the models, accounting for the differing number of galaxies from each model. Coloured solid lines show difference in log SFR space between this and the median SFH for all galaxies from individual models. The shaded region shows the median variance (84th−16th percentile)/2 in the SFHs across all the models. At high redshifts, modelling differences give rise to high amounts of variability in galaxy SFHs. The differences between the different models is small for $z \lesssim 1$ in the 10^{10}M$\odot$ bin, but rises in the higher mass bins as galaxies begin to quench and mass growth through merging gets more important.

their SFR, as seen in Section 3.1.2. This means that despite these differences, the overall picture of galaxy mass assembly described by the models is similar.

At late times (low redshifts), there is an increase in the overall variance between the different models with increasing mass, ranging from ∼0.3 dex at $M_* \sim 10^{10.0}\mathrm{M}_\odot$ to $\gtrsim 1$ dex for massive galaxies ($M_* > 10^{10.5}\mathrm{M}_\odot$). The median SFHs across all models agree well at $z < 1$ in the lowest mass bin. These trends are not easy to interpret since, as we discuss in Section 2.2, these SFHs are tracing the SFR of the main progenitor as well as of all the accreted systems. This means that this late time divergence is probably a combination of how the various models implement quenching as well as the SFH of the accreted systems. Although a full treatment studying the cause of these differences is outside the scope of this analysis, quantifying the differences between the PSDs for these SFHs begins to illustrate how differing strengths of SFR fluctuations across a range of time-scales could shape the overall SFHs over the next few sections.

Additional plots showing the distributions of SFH parameters such as stellar mass, sSFR, SFH peak, and width for the various models can be found in Appendix B.

3.3 Comparing PSDs across different models

Section 3.1 describes some of the overall trends in the PSDs – the distribution of power across a broad range of time-scales, with an increase in power towards longer time-scales/shorter frequencies. However, each model shows unique trends in how the PSDs evolve with stellar mass, as well as the actual strength of the PSD at different time-scales.

Since there are a range of modeling assumptions and numerical recipes used across the various models we consider, a comparison in PSD space serves to highlight the differences in the resulting variability of their SFHs on different time-scales. Fig. 11 shows where the median PSDs of galaxies from the various models (as shown in Figs 5–7) lie in PSD slope versus PSD power space at three representative time-scales (300 Myr, 1 Gyr, and 10 Gyr), and an interactive version of this plot spanning time-scales ranging from ∼200 Myr to 13 Gyr can be found online.[9] An equivalent plot showing individual galaxies from the zoom simulations is shown in Fig. 12. The PSD power is the strength of SFR fluctuations or 'burstiness' at a given time-scale. The local slope of the PSD at a given time-scale is computed using the PSD within a log time-scale of ±0.1 dex, and is a measure of how tightly coupled the PSD is to adjacent time-scales. Changing this interval while computing the slope does not affect the overall trends across the models. A slope of 2 can be found in models of stochastic star formation described by random walks (Caplar & Tacchella 2019; Kelson et al.

[9] https://kartheikiyer.github.io/psd_explorer.html

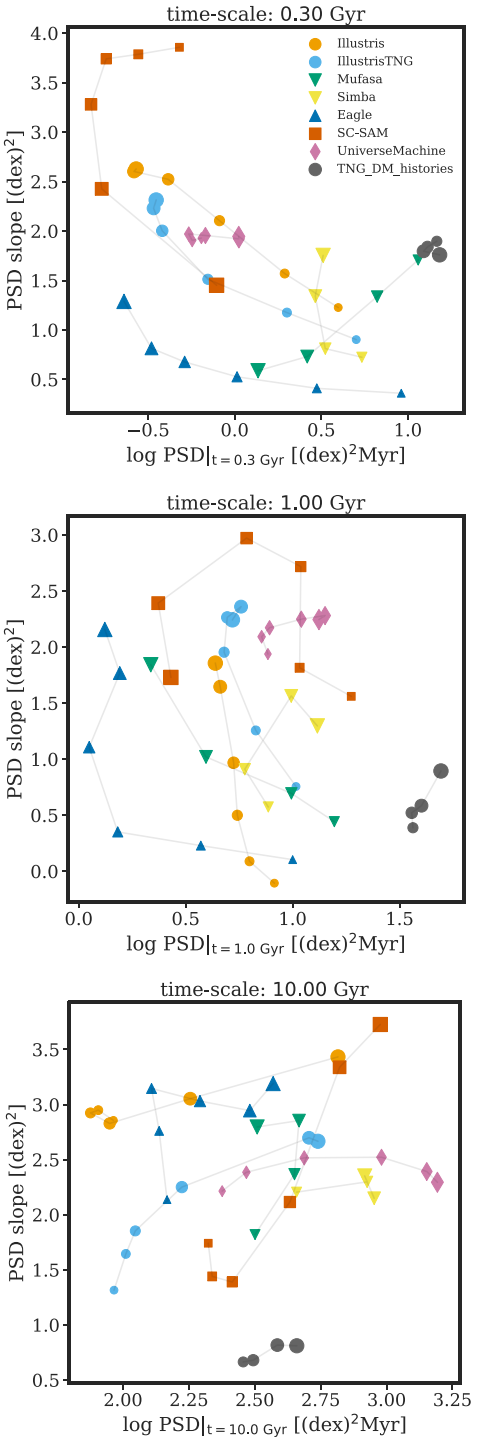

Figure 11. Quantifying the behaviour of the PSDs in slope-power space at different time-scales. This amounts to taking cross-sectional slices of the PSDs in Figs 5–7 at 300 Myr (top) and 1 Gyr (middle) and 10 Gyr (bottom). The circle size increases with stellar mass, using the same 0.5 dex stellar mass bins as previous figures. The x-axis shows the overall power in the PSDs at different time-scales and masses, while the slope indicates how tightly the time-scales are coupled. Moving towards higher power and lower slope (bottom-right) increases how 'bursty' the SFR is. While the PSDs inhabit a similar locus in slope-power space at shorter time-scales, they show varied behaviour at time-scales of ∼1 Gyr. An interactive version of this plot can be found online at https://kartheikiyer.github.io/psd_explorer.html.

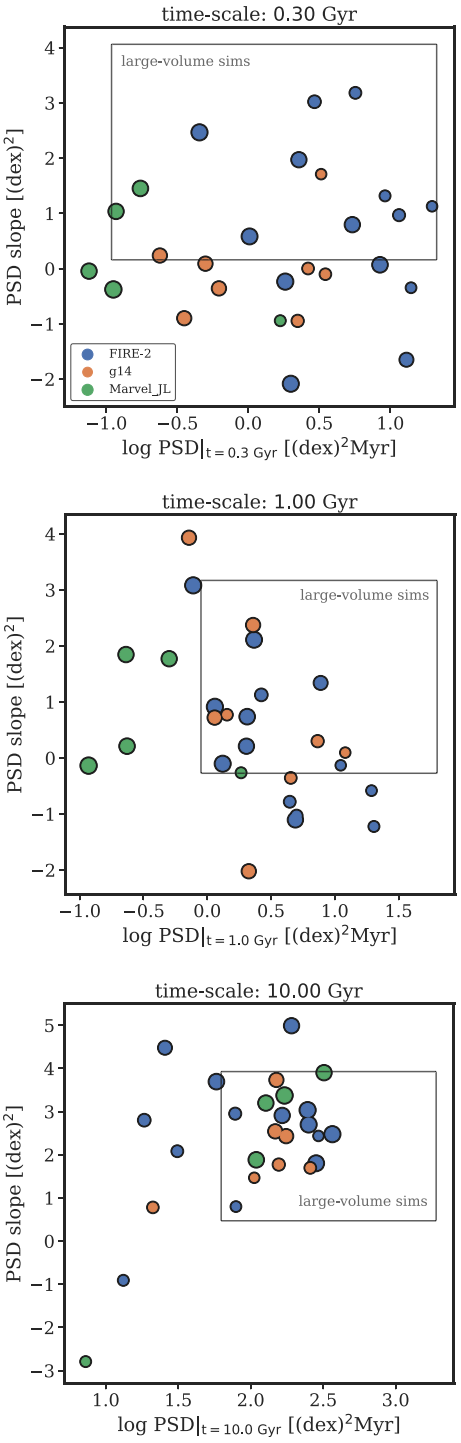

Figure 12. Similar to Fig. 11, but for individual galaxies from the zoom simulations. The bounding boxes correspond to the edges of the corresponding panels in Fig. 11 for the median PSD slope and power from the large volume models. There is a notable trend towards increasing power with decreasing stellar mass on ∼300 Myr time-scales. While a similar trend is also seen in the large-volume hydrodynamical simulations, the lack of PSD contamination on the shortest time-scales due to the significantly higher resolution of the zoom simulations makes this a more robust result, albeit with a much smaller sample.

2020). Tacchella et al. (2020) find this to emerge naturally within the framework of the gas regulator model (Lilly et al. 2013) and in modelling stochasticity due to GMC formation and destruction. Most high-mass and low-sSFR galaxies across the different models show a slope ∼2, while UniverseMachine shows this at all stellar masses. Individual points for each model show the median slope and power of the PSDs in the same 0.5 dex bins of stellar mass that are used in Figs 5–7, highlighting evolution in PSD space as galaxies grow more massive.

A key point to note is that the various models are extremely diverse in (i) the region of PSD space they occupy at a given time-scale, and (ii) their evolution with stellar mass. At ∼300 Myr time-scales, there seems to be an overall attractor towards increasing slope and decreasing power as the stellar mass increases, although this does not hold for all the models. The short-time-scale power generally increases as a function of decreasing stellar mass, indicating that lower mass galaxies are generally more bursty across a variety of models. This trend is not as prominent for the SAM and empirical model. Meanwhile, at ∼1 Gyr time-scales the models seem to follow a range of different behaviours, although most models seem to converge on a PSD slope of $\beta \sim 2$ at high stellar masses. On the longest time-scales, both slope and power tend to increase with increasing stellar mass, in part due to the increased contribution from quenched galaxies to the long time-scale PSD power. Depending on how the individual models implement quenching, however, the rate and extent of this effect can vary greatly (see Section 3.4).

It should be noted that although these trends are shown using the median values for the PSD slope and power in a given mass bin, there is a large amount of variance in the range of slope and power values possible for individual galaxy PSDs due to features that may be present in individual galaxy SFHs based on stochastic events like halo accretion fuelled star formation and major mergers. The variance in slopes is from $\sigma(\text{PSD slope}) \sim 0.7-1.0\ (\text{dex})^2$ and in power is $\sigma(\log \text{PSD}) \sim 0.2-0.7(\text{dex})^2$ Myr, corresponding to the shaded regions in the individual PSD plots and generally increasing with increasing stellar mass. While the large variance indicates that individual galaxies in a given mass range exhibit a large diversity in behaviour, trends across stellar mass are generally robust since they trace the behaviour of the entire population.

Given that the models span such a wide range in PSD slope and power at any given mass and time-scale, observational constraints in this space (Caplar & Tacchella 2019; Wang & Lilly 2020b) would provide strong constraints on modelling galaxy physics.

3.4 The PSDs of star-forming versus quiescent galaxies

Quenching becomes an increasingly important phenomenon as we consider galaxies with higher stellar masses. This phenomenon can be driven by a range of different physical processes acting on different time-scales. Since the quenching of galaxies is an observably measurable phenomenon, it is therefore possible to get observational constraints on quenching time-scales and connect them to the relevant physical processes. Here, we explore the differences in the PSDs of actively star forming and quiescent galaxies at $z = 0$ to determine what, if any, differences they show at different stellar masses.

To perform this analysis, we first need to select galaxies that are quiescent at the time of observation. There exist multiple ways of performing this selection, depending on the definition of quenching (e.g. through a cut in UVJ space, in specific SFR, or a threshold distance from the SFR–M_* correlation, among others, see e.g. Donnari et al. 2019; Hahn et al. 2019b). In the current analysis, we separate galaxies into star forming versus quiescent using a commonly used threshold in sSFR [$\text{sSFR} < 0.2/\tau_H \sim 10^{-10.83}\text{yr}^{-1}$ for quiescent galaxies at $z \sim 0$, see Pacifici et al. (2016) and Carnall et al. (2020)]. This approach is motivated by two reasons: (i) since we already have access to the SFHs, this allows us to avoid the systematic assumptions of forward-modelling rest-frame UVJ colours and the degeneracies of separating quiescent galaxies in that space, and (ii) we avoid the systematics of accounting for different SFR–M_* correlations across the different models (Hahn et al. 2019b) and use a uniform threshold for comparison across the models.

Having identified quiescent galaxies across the various models, we then compare the PSDs of quiescent galaxies to those of star-forming galaxies at different stellar masses. Since quenching distinctively alters the shape of a galaxy's SFH, we expect the PSDs of quiescent galaxies to show more power on long time-scales. Fig. 13 shows the difference in the median log PSDs of quiescent and star forming galaxies in the same 0.5 dex stellar mass bins used in the rest of this work. We exclude the highest mass bin ($M_* \sim 10^{11.5}\text{M}_\odot$), since there are not enough star-forming galaxies in all the models to perform this analysis.

We see that at low stellar masses, the quiescent galaxy PSDs generally show greater power on long time-scales, with the exact time-scale varying across models, ranging from ∼900 Myr to $\gtrsim$3 Gyr. As we go to higher stellar masses, we find that there is an excess of power across a range of shorter time-scales in the IllustrisTNG, Simba, EAGLE, and SC-SAM models. This could be explained by processes driving quenching also driving variability in SFRs on other time-scales. For example, multiple short episodes of feedback due to (i) AGN-driven outflows leading to the eventual quenching of galaxies, as seen in the implementation of jet mode AGN feedback (Rodríguez Montero et al. 2019) or (ii) X-ray feedback rapidly evacuating the star-forming gas in the central regions (Appleby et al. 2020) could lead to increased short-time-scale variability in Simba. In contrast, since Mufasa implements quenching primarily through a 'maintenance mode' feedback, it does not show a strong evolution with stellar mass. Another explanation for this increase in power on short time-scale for quiescent galaxies could be that the quiescent galaxies assemble their mass earlier, when SFHs in general were more bursty (Muratov et al. 2015; Hayward & Hopkins 2017). The phenomenon of quiescent galaxies assembling their mass earlier can be seen the correlation between t_{50} and sSFR for quenched galaxies among the various models shown in Appendix B. However, the nature of this correlation is uniform across all the models and cannot fully account for the variations in the difference between star-forming and quenched galaxy PSDs observed between the models.

In more detail, the Illustris and IllustrisTNG models both show sharp breaks above which the power in quiescent galaxies rises, with the break occurring on longer time-scales in IllustrisTNG. The increase in power on short time-scales with increasing mass is also more prominent in TNG compared to Illustris. The updated winds and AGN feedback in IllustrisTNG also show a noticeable increase in power on short time-scales above masses $10^{10.5}\text{M}_\odot$, where AGN feedback becomes most effective. EAGLE shows a much broader range of time-scales in comparison, similar to Simba albeit with high power at a given mass. The SAM shows a significant increase in power on time-scales below ∼2 Gyr, with this trend increasing with stellar mass. This seems to be primarily associated with stochastic starbursts on short time-scales triggered by mergers, with more massive galaxies experiencing these events to a larger extent. UniverseMachine shows a moderate increase in power with quenching over all time-scales.

In summary, PSDs across the different models show a range of behaviours when galaxies quench, with strong mass dependence in

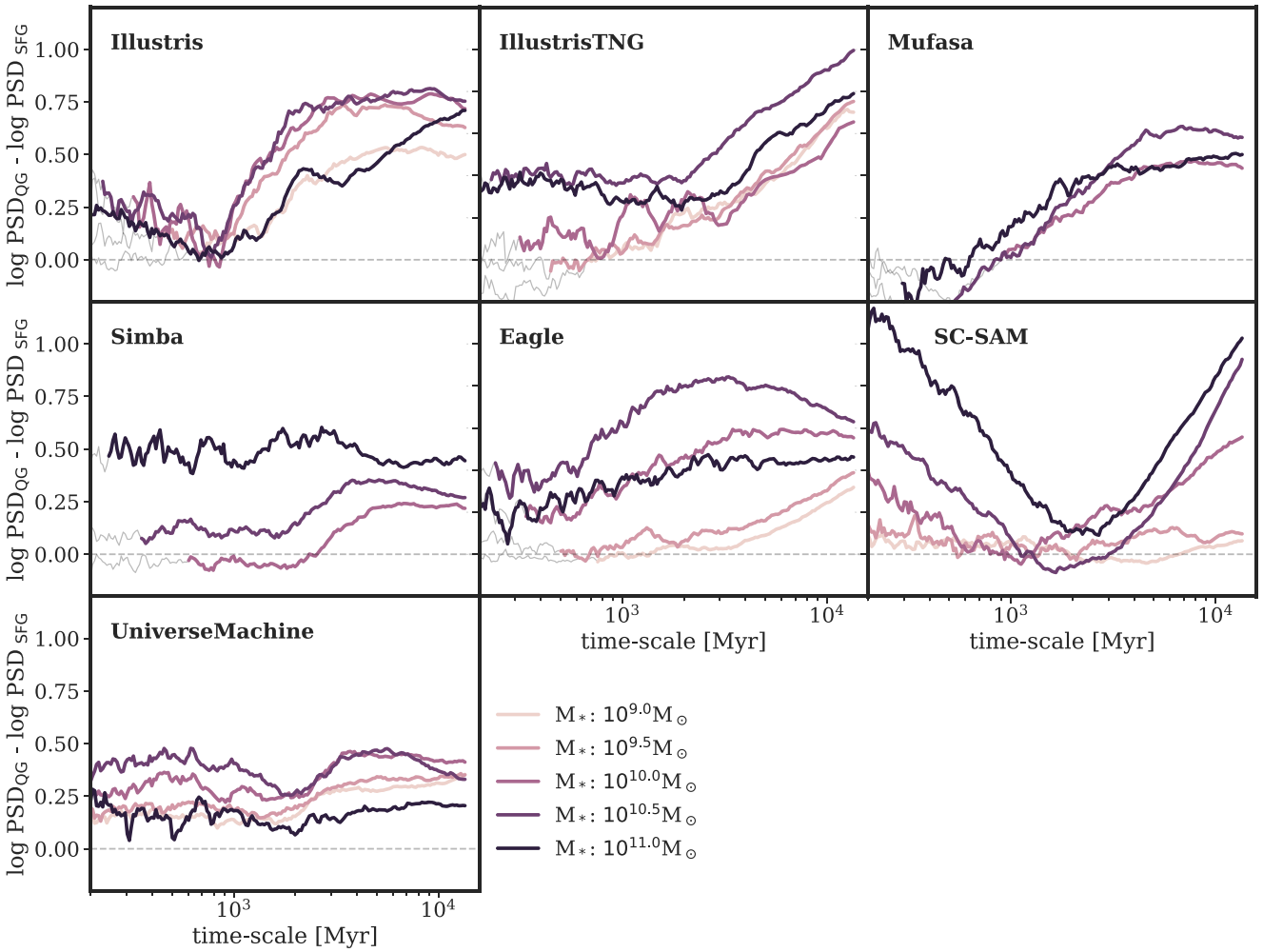

Figure 13. The difference between the median log PSDs of quiescent and star-forming galaxies in 0.5 dex bins of stellar mass. The bins are the identical to those in Figs 5–7, starting from $10^9 M_\odot$ for all the large-volume models we consider except Mufasa and Simba, which start at $10^{10} M_\odot$ due to lower resolution. Coloured lines represent different mass bins, while grey curves denote regions where we expect resolution-dependent shot-noise to contaminate the PSDs. The PSDs of quiescent galaxies are notably greater than those of star-forming galaxies on long time-scales, with some models showing mass-dependent trends on shorter time-scales.

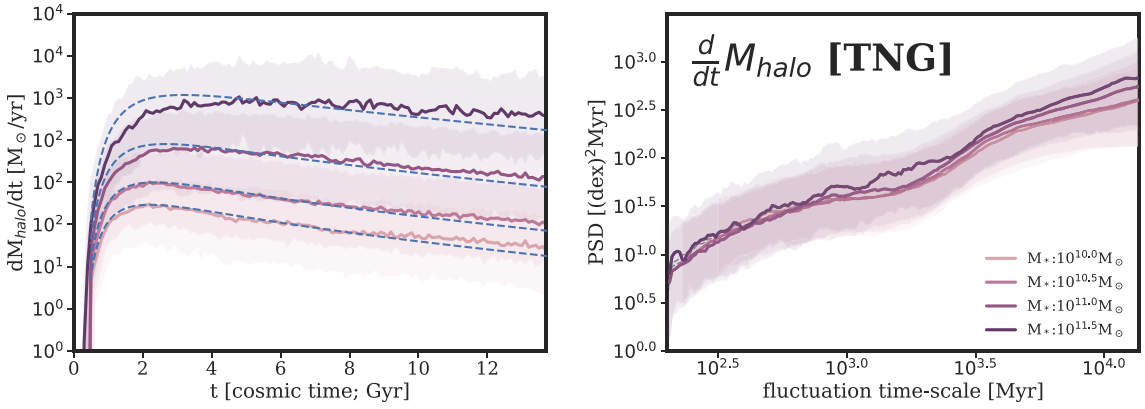

Figure 14. Equivalent to Fig. 5, halo mass accretion histories and corresponding PSDs for the parent haloes of galaxies in the IllustrisTNG simulation, in bins of stellar mass. In comparison to the SFH PSDs, the halo accretion history PSDs show a remarkable self-similarity for galaxies in different bins of stellar mass. The dashed blue lines in the left-hand panel provide a comparison to the median DM accretion histories computed using the EPS formalism as outlined in Correa et al. (2015), calculated using the median DM halo mass for each stellar mass bin.

some models (IllustrisTNG, Simba, EAGLE, SC-SAM) and a range of time-scale-specific breaks in the PSD (∼900 Myr in Illustris, ∼2−3 Gyr in IllustrisTNG, ∼3−4 Gyr in Simba, and ∼2 Gyr in the SC-SAM). Observational constraints in PSD space for star-forming and quiescent galaxy populations will provide sensitive probes of discriminating between the range of quenching mechanisms implemented across these models.

3.5 How dark matter accretion shapes PSDs

Upon examining the PSDs of galaxy SFHs across different models, we find that most of the power resides in the long time-scales on which SFHs rise and fall. At early cosmic times, several models find the SFHs of galaxies to be correlated with the DMAHs of their parent haloes (Wechsler & Tinker 2018). Diemer et al. (2017) model galaxy SFHs as lognormal curves, and find that the peak and width of SFHs in Illustris correlate strongly with the properties of their DMAHs with an offset between the formation times of haloes and galaxies that increases with stellar mass, along with a tight relation between the BH mass and peak time. Similarly, Qu et al. (2017) show that the SFHs of galaxies in EAGLE increasingly decorrelate from the halo accretion histories at increasing masses, by plotting the formation time versus accretion time for haloes and galaxies across stellar mass bins. They find this to be due to AGN feedback, which suppresses *in situ* star formation and causes the stars in massive galaxies to form early and the galaxies to grow subsequently by mergers (i.e. the majority of star formation finished early), while haloes continue accreting mass until late times (i.e. massive haloes form late) (Neistein, van den Bosch & Dekel 2006).

From an analytical standpoint, Kelson (2014) models star formation as a stochastic time series, with the 'long-time-scale memory' encapsulated by a Hurst parameter of ∼0.98 ± 0.06. In Kelson, Benson & Abramson (2016), this model is extended to derive stellar mass functions at early times, explicitly relating the variance of the SFRs for an ensemble of galaxies to the DM haloes and their ambient matter densities at the epoch when star formation begins. Kelson et al. (2020) analytically estimate the slope of the DMAH PSD to be ∼1.

With this in mind, it would therefore be instructive to (i) compute the PSDs of DMAHs and study their behaviour, (ii) study the extent to which variability in galaxy SFHs is tied to the variability in the DMAHs of their parent haloes, and (iii) examine if SFHs and DMAHs are coherent, to understand if dark matter accretion drives star formation.

3.5.1 The variability of DMAHs

We compute the PSDs for a sample of DMAHs from IllustrisTNG, defined as $\Delta M_{\rm halo}$ from one time-step to another with the same $\Delta t =$ 100 Myr bin width. The halo accretion histories are computed using the Friend-of-Friend (FOF) and SUBFIND algorithms (Davis et al. 1985; Springel et al. 2001; Dolag et al. 2009), by selecting galaxies with $M_* > 10^9 {\rm M}_\odot$ at $z \sim 0$ and tracing them back in time to find all the dark matter particles associated with the halo of the main progenitor at each snapshot from $z \sim 20$ to $z = 0$, described in detail in Pillepich et al. (2018b). While this does not correspond directly to the full SFH that we have been considering so far, it is possible to relate it to the *in situ* SFH of the central progenitor, and then connect the *in situ* SFH to the full SFH. Since the halo accretion histories are only accessible at the discrete time-steps of the IllustrisTNG snapshots, they have been interpolated to match the uniform time-grid used throughout the rest of this work. Comparing the computed PSD after this interpolation to periodograms computed using the original uneven snapshot time-steps do not show any significant differences. We also repeated the analysis with different halo mass definitions based on the DM mass within certain fractions of $R_{\rm crit,200}$ or within fixed distances of 10, 50, and 100 kpc from the centre of the halo potential, and found that the resulting trends do not change significantly.

Fig. 14 shows the DMAHs of galaxies in IllustrisTNG across four bins in stellar mass. For each stellar mass, the median DM halo masses in the 0.5 dex bin are $M_{\rm halo} \sim 10^{11.61}$, $10^{11.89}$, $10^{12.37}$, and $10^{12.89} {\rm M}_\odot$, corresponding to stellar masses of $M_* \sim 10^{10}$, $10^{10.5}$, 10^{11}, and $10^{11.5} {\rm M}_\odot$, respectively. The dashed blue lines show the average DMAHs based on the extended Press–Schechter (EPS) formalism (Press & Schechter 1974; Bond et al. 1991; Lacey & Cole 1993), which provides an approximate description for the hierarchical growth of DM haloes from an initial Gaussian density field as a stochastic process. Specifically, the accretion histories were computed using an analytic model derived from the EPS formalism described in Correa et al. (2015). The analytic curves are a good match to the IllustrisTNG DMAHs, and show a rise and a slight subsequent decline described by the relation $M_{\rm halo}(z) = M_0(1+z)^{af(M_0)} {\rm e}^{-f(M_0)z}$, where M_0 is the mass of the halo at $z \sim 0$, a depends on cosmology and $f(M_0)$ is related to the linear (spatial) matter power spectrum. We find that the PSDs show a remarkable self-similarity, with a slight increase at the longest time-scales corresponding to the overall normalization of the halo mass. The PSDs also show a 'plateau'-like behaviour at ∼1−3 Gyr time-scales, i.e. a sharp break towards increasing PSD slope from $\beta \sim 0.3$ to $\beta \sim 1.6$, followed by a break towards slopes of $\beta \sim 0.6-1$ on long time-scales. However, this trend is weak in the highest mass bin. Although outside the scope of the current work, the physical origin of this feature could be independently verified by comparing against PSDs from DM-only simulations. Such an analysis will necessitate a slightly different sample selection approach, since here we simply computed the PSDs for the DMAHs of the parent haloes of galaxies in fixed stellar mass bins.

The slopes also increase to $\beta \sim 1.6$ as we approach the shortest time-scales probed. Overall the median PSD slopes are ∼1, consistent with the analytical derivation of Kelson et al. (2020). On long time-scales, haloes are thought to grow by smooth accretion, while on shorter time-scales they grow by merging (Dekel et al. 2013). Understanding the origin of this plateau, and whether it can be derived within the EPS formalism[10] is therefore an interesting challenge for models of halo growth.

3.5.2 Comparing the PSDs of DMAHs to SFHs

Having computed the PSDs of DMAHs, we would now like to compare them to the PSDs of SFHs computed earlier. To this end, Fig. 15 shows the excess power in the median PSDs of galaxy SFHs from IllustrisTNG compared to those of DMAHs across bins of stellar mass 0.5 dex wide.

Since the DMAHs generally have a higher overall normalization and correspondingly larger fluctuations due to considering the accretion and mergers of the entire haloes instead of just their baryonic component, we normalize the PSD for each central galaxy – parent halo pair by the ratio of their stellar mass to halo mass, in effect bringing the DMAHS to the same scale as the SFHs. Doing so allows

[10]That is, relating the *spatial* matter density power spectrum to the *temporal* mass accretion history power spectrum, see Kelson et al. (2020).

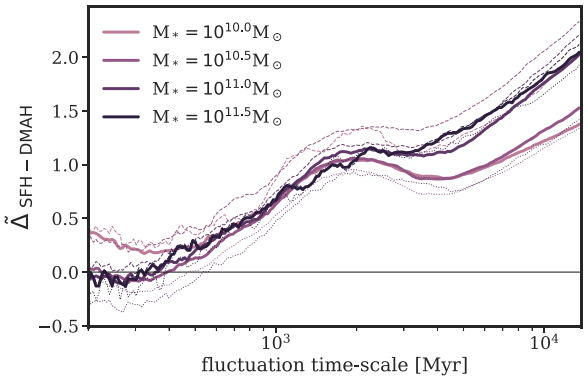

Figure 15. The difference between the median DMAH and SFH PSDs for IllustrisTNG ($\tilde{\Delta}_{\rm SFH-DMAH} = \log {\rm PSD}_{\rm SFH} - \log {\rm PSD}_{\rm DMAH.scaled}$). Since the DM accretion rates are generally higher and have more variance than their corresponding SFHs, the PSDs for each halo are scaled by a factor of $M_*/M_{\rm halo}$ prior to computing the median DMAH PSDs in a given mass bin. Thick solid lines show the median difference in PSDs corresponding to 0.5 dex mass bins centred at the values shown in the legend. Dashed lines show the difference in PSDs for quiescent galaxies, while dotted lines show the PSD difference for star-forming galaxies.

us to compare their PSDs on a similar footing. Note that this is not a perfect comparison, since it assumes that the $M_{\rm halo}-M_*$ ratio is roughly constant throughout cosmic time. However, this assumption only needs to hold for ensembles of haloes, and is motivated by studies that find a only a mild evolution of baryon fraction with redshift (Crain et al. 2007) in conjunction with extensions to central galaxies (Kulier et al. 2019).

Fig. 15 finds that the excess power in SFHs in comparison to DMAHs lies mostly on longer time-scales, which can also be inferred from the steeper slopes of their PSDs – IllustrisTNG SFHs have median slopes of $\beta \sim 2 \pm 0.4$, compared to DMAHs, whose PSDs have median slopes of $\beta \sim 1 \pm 0.4$. On the shortest (∼200 Myr) time-scales, the DMAHs have comparable power to the IllustrisTNG SFHs. While this does not imply that DM accretion is driving the variability on these time-scales, it is a helpful coincidence that accounts for why Mitra et al. (2016), Rodríguez-Puebla et al. (2016), Kelson et al. (2020) get the right scatter for the SFR–M_* correlation using models that correlate SFRs with DM accretion rates, without having to invoke arguments of SFR regulation by feedback. In an alternate analysis, Feldmann et al. (2019) find that the scatter of DM accretion rates measured over ∼Gyr time-scales is not sufficient to explain the scatter of the star-forming sequence. While this runs counter to the idea put forth by Rodríguez-Puebla et al. (2016), both results are consistent if we take the time-scale into consideration, as seen in Fig. 15. There is a noticeable plateau in the DMAH PSDs that translates to a coherent feature at ∼1−3 Gyr in Fig. 15, although the prominence of this feature decreases with stellar mass. A portion of this excess power on long time-scales appears to come from quenching, which decorrelates when galaxies form their stars from when haloes assemble their mass. This can be seen from the difference between the median PSD difference between SFHs and DMAHs for star forming (dotted) and quiescent (dashed) galaxies in a mass bin, and in Section 4.1. Even with quenching accounting for up to ∼1 dex of power on time-scales $\gtrsim$3 Gyr, there still remains an excess of about ∼0.8−1 dex of power on time-scales above a Gyr with a tail towards shorter time-scales, that needs to be accounted for by mergers and dynamical processes within galaxies.

3.5.3 *The coherence of* in situ *SFHs and DMAHs*

It is important to keep in mind that the mass assembly histories of galaxies are different from their SFHs, since mergers bringing in already-formed stars would be counted in the former at the time when the merger occurs, but in the latter when the *ex situ* stars first formed. Since the contribution from *ex situ* star formation is known to correlate strongly with stellar mass across different models (Rodriguez-Gomez et al. 2015; Qu et al. 2017; Moster, Naab & White 2018; Behroozi et al. 2019; Tacchella et al. 2019), it would be instructive to understand the time-scale dependence of correlations between the *in situ* star formation and the full SFH, as well as the correlations between the *in situ* star formation of the central progenitor and the DMAH of its parent halo. We quantify this by computing the cross power spectrum, given by $P_{xy} = \int (\int x(t) y(t + t') {\rm d}t') {\rm e}^{-ikt} {\rm d}t$, and using it to find the coherence, $C_{xy} = P_{xy}^2 / |P_x P_y|$ for these two sets of time series, where P_x, P_y are the PSDs of the two time series x and y (in this case SFHs and DM accretion histories, or full and *in situ* SFHs) and P_{xy} is the cross-power spectrum. The coherence is therefore the normalized excess in power compared to each series taken in isolation.

The top panel of Fig. 16 shows the coherence computed for the full SFHs compared to just the *in situ* SFH of the central progenitor for IllustrisTNG galaxies. We see that while the coherence is high on long time-scales, which means that the shape of the two SFHs cannot be too different, the coherence on shorter time-scales falls off on shorter time-scales with increasing mass. Rodriguez-Gomez et al. (2015) and Tacchella et al. (2019) showed that more massive Illustris and IllustrisTNG galaxies assemble an increasing fraction of their mass *ex situ*, due in part to an increased number of major and minor mergers. Mergers bring in lower mass galaxies, which typically have more power on shorter time-scales. This leads to the full SFH decorrelating from that of the central progenitor on shorter time-scales. The bottom panel of Fig. 16 shows the coherence computed between the DM accretion histories and the *in situ* SFH of the central progenitor, which most closely tracks the parent halo. This plot quantifies the effect of baryonic physics on regulating SFR on short time-scales, as the two quantities are linked on the longest time-scales, but fall off rapidly at time-scales below ∼3 Gyr. Similar to the DM accretion history PSDs, there is only a weak trend with increasing stellar mass.

In summary, (i) the variability of DMAHs, quantified using their PSDs, is self-similar across different masses and has a median slope of ≈1; (ii) the DMAHs do not contribute significantly to the overall variability of their SFHs, except at the shortest ($\lesssim$400 Myr) time-scales where their variability is similar to those of SFHs. Quenching can account for a significant fraction of the excess power in SFHs on the longest time-scales; and (iii) The DMAHs are coherent with the *in situ* star formation of galaxies on long time-scales ($\gtrsim$3 Gyr). Therefore, they may set the overall shape of the *in situ* mass assembly histories of their central galaxies.

4 DISCUSSION

The PSD formalism provides a useful way to quantify the variability in galaxy SFHs across different time-scales. Applying this to a variety of different models of galaxy evolution, we find that the PSDs of galaxy SFHs generally show broken power-law shapes, with a tendency to grow more featureless and tend to a single power-law with slope $\beta \sim 2$ towards higher stellar masses. The PSDs also show a wide diversity between the models in terms of slope and power at any given stellar mass and time-scale. In Section 4.1, we relate these observed PSD features to existing

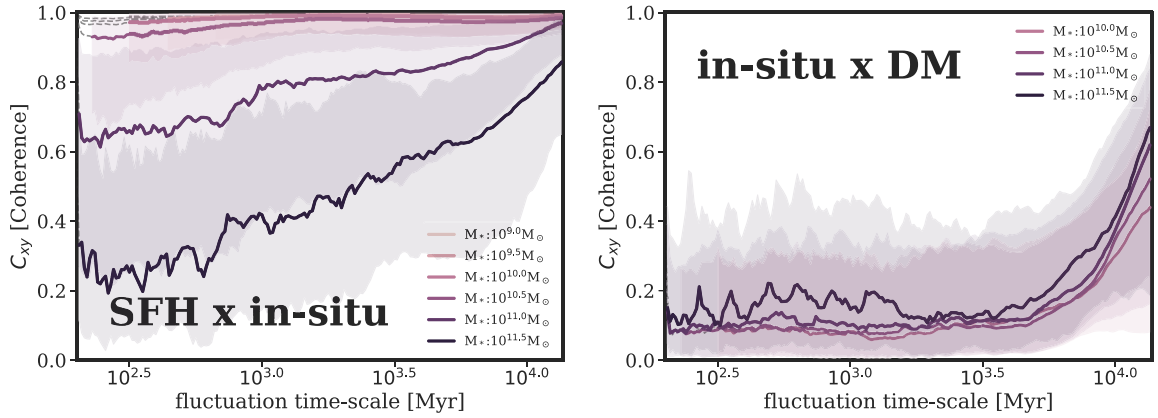

Figure 16. The coherence between the *in situ* component of the SFHs to the full SFHs (top), and that of the *in situ* SFHs with the DMAHs (bottom) of their parent haloes at different time-scales. Coherence is defined as $C_{xy} = P_{xy}^2/|P_x P_y|$. As more massive galaxies grow a greater fraction of their mass *ex situ* due to mergers, they increasingly decohere from their *in situ* SFHs on shorter time-scales. The PSDs of dark matter and *in situ* SFR are largely mass invariant and only weakly related at short time-scales, where baryonic processes dominate. The slightly higher coherence in the highest mass bin on shorter time-scales could be due to short-lived bursts of star formation induced by mergers.

estimates for the time-scales on which different physical processes are expected to act, with a table reported in Appendix C. In Section 4.2, we discuss observational measurements and techniques that can be used to obtain constraints in PSD space. Section 4.3 demonstrates the effects of lower resolution on PSDs using additional runs of the IllustrisTNG simulation. Finally, Section 4.4 considers possible directions for extending the analysis presented in thi s work.

4.1 The characteristic time-scales of physical processes in simulations

There exist a range of estimates in the literature for time-scales associated with different physical processes, some of which are shown in Fig. 1 and listed in Appendix C. In this section, we briefly summarize the current state of our understanding regarding which physical processes can contribute to SFR fluctuations at various time-scales. By doing this, we can begin to connect the different features seen in the median PSDs of SFHs in Section 3.1.2 to the underlying physical processes responsible. It also serves as a useful starting point for future analyses looking at these features in greater depth within specific models. Starting with processes that act on the shortest time-scales, we gradually work our way to the longer time-scales that are the focus of the bulk of this paper.

4.1.1 GMC formation and destruction

Star formation on small spatiotemporal scales occurs in GMCs, whose lifetimes are sensitive to a variety of factors including cloud collisions and mergers, feedback from supernovae, cosmic rays, and photoionization, turbulence in the ISM, and the growth of magnetic fields (Dobbs, Pringle & Burkert 2012; Dobbs, Pringle & Duarte-Cabral 2015; Kim & Ostriker 2017; Pakmor et al. 2017; Semenov et al. 2017; Benincasa et al. 2020). Current upper bounds on theoretical predictions for GMC lifetimes range between ∼7 and 20 Myr (Tasker 2011; Benincasa et al. 2020), with estimates for the time-scales of individual processes that influence GMC lifetimes reported in Appendix C. Analytical models can also provide an understanding of when star formation in this regime can be bursty (Faucher-Giguère 2018).

Considering the rate of GMC formation and destruction to be a stochastic process, we would therefore expect a power-law PSD with slope $\beta \sim 2$ at these time-scales (Kelson 2014; Tacchella et al. 2020). Although the large-volume models do not probe these time-scales, the three suites of zoom simulations allow us to test this hypothesis. In fact, we do find the PSD in this time-scale to be well-described by power-laws, and the g14 and Marvel/Justice League galaxies show slopes of $\beta \sim 1.6^{+0.4}_{-0.1}$ uncorrelated with stellar mass, while the FIRE-2 galaxies show slopes of $\beta \sim 1.8^{+0.5}_{-0.4}$, with a mild trend of increasing slope with stellar mass over time-scales of ∼10−20 Myr.

4.1.2 Dynamical processes within galaxies

A range of physical processes act to influence the state of the ISM on galaxy dynamical time-scales (∼10^8 yr). These processes include turbulence in the ISM, molecular gas encountering spiral arms and bars, galactic winds, and the rapid cycling of ISM gas between star-forming and non-star-forming regions, in addition to the exponential growth of magnetic fields, and stochastic inflows of CGM gas.[11] Analytical models account for these processes through a range of time-scales, including time-scales for gas accretion and cooling, as well as star formation, turbulent crossing and effective viscous time-scales that describe how long it takes for accreted gas to reach the centre of the galaxy (Dekel, Sari & Ceverino 2009; Krumholz & Burkert 2010; Forbes et al. 2014a). For modelling these processes, resolution plays an extremely important role since resolving the ISM allows simulations to capture the effects of turbulence driven by feedback, as well as model the feedback self-consistently while relaxing the need for sub-grid recipes. Most of our knowledge in this regime comes from small-volume simulations (e.g. a slice of a galactic disc, Kim & Ostriker 2017, or an idealized disc Semenov et al. 2017) or zoom simulations focusing on individual galaxies (Ceverino et al. 2014; Hopkins et al. 2014; Christensen et al. 2016). Bursty star formation has been noted on time-scales of ∼45 Myr in the TIGRESS framework (Kim & Ostriker 2017), and on ≤100 Myr time-scales in FIRE-2 (Sparre et al. 2017; Hung et al. 2019).

[11] The last two extend to longer time-scales as well.

Since there are many competing factors at play, we expect the PSDs in this regime (and beyond) to be complicated, and this is what we generally see in all the zoom simulation suites. Overall, while the PSDs can still be approximated with a power-law, several PSDs show minor peaks[12] or breaks[13] with average slopes in the ∼30−100 Myr range of $\beta \sim 2.0^{+0.8}_{-0.7}$ for g14 and Marvel/Justice League and $\beta \sim 1.3^{+0.4}_{-0.5}$ for FIRE-2. All three suites of simulations show increased scatter in the power-law slopes, along with a trend of increasing slope with stellar mass in this time-scale range, perhaps correlated with decreasing dynamical time-scales as galaxies grow more massive.

4.1.3 Mergers

Mergers between galaxies bring in a combination of stars that have already formed and gas that can fuel a burst of subsequent star formation, with time-scales ranging from ∼100 to 500 Myr (Hernquist 1989; Barnes & Hernquist 1991, 1996; Mihos & Hernquist 1996; Robertson et al. 2006b; Hani et al. 2020). The effect on SFHs comes from mergers as a primary mechanism for driving starbursts in galaxies (in addition to disc instabilities) and as a controversial trigger for quenching, depending on a variety of factors including the mass ratio, relative alignment, how gas-rich the merger is, and even if the merger triggers a central AGN (Hopkins et al. 2006; Governato et al. 2009). Zoom simulations also predict that mergers or counter-rotating streams can lower the angular momentum of the gas disc within galaxies, leading to a compaction of the gas phase, which results in an enhancement of the SFR (Zolotov et al. 2015). These phases can last for one to a few hundred Myr and move galaxies to the upper envelope of the SFS (Tacchella et al. 2016). Rodríguez Montero et al. (2019) find that major mergers cause enhanced SFR at all masses below a threshold of $\sim 10^{11} M_\odot$ in Simba. Tacchella et al. (2019) find trends consistent with centrally enhanced star formation due to *ex situ* star formation for intermediate mass ($10^{10-11} M_\odot$) galaxies, with mergers responsible for over two-thirds of the *ex situ* component towards the high-mass portion of that range. A notable consequence of this is the increasing loss of coherence between the *in situ* and full SFHs of galaxies in Fig. 16 with increasing stellar mass.

In addition to the time-scale of SFR enhancement following a merger, we also need to consider the fact that mergers themselves are stochastic events, and therefore carry an additional implicit time-scale. Estimates of merger time-scales are generally $\mathcal{O}(1)$ Gyr (Boylan-Kolchin et al. 2008; Lotz et al. 2011; Snyder et al. 2017), and can vary significantly depending on assumed definitions and factors like pair separation and angular momentum of the system. Due to these factors, it can be difficult to isolate the effects of mergers on galaxy PSDs.

4.1.4 Baryon cycling

The global efficiency of how galaxies are able to convert their gas into stars is almost an order of magnitude different from local efficiencies in star-forming regions. Semenov et al. (2017) tie this to the cycling of ISM gas between regions that are star forming and those that are not. In addition to this, gas that leaves the galaxy due to ejective feedback and returns also contributes to prolonging the period over which a galaxy continues to form stars (Christensen et al. 2016; Hopkins et al. 2018; also see review by Tumlinson, Peeples & Werk 2017 and references therein). The lifetimes and dynamics of cold clouds in the halo are also subject to a variety of time-scales (Forbes & Lin 2019).

Estimated time-scales for the cycling of baryons span a wide range, from ∼100 Myr to about 3 Gyr (Oppenheimer et al. 2010; Christensen et al. 2016; Mitra et al. 2016; Anglés-Alcázar et al. 2017a; Grand et al. 2019). Some studies find the time-scales to scale with halo or stellar mass (Oppenheimer et al. 2010; Mitra et al. 2016), while other studies find it to be largely independent of mass (Christensen et al. 2016). While we find evidence for peaks and breaks in the PSDs of individual galaxies on these time-scales, especially in the zoom simulations (e.g. in Fig. 9), the broad range of time-scales and the dependence on galaxy properties other than stellar mass results in these peaks being washed out in the median behaviour for an ensemble of galaxies. However, it is possible that breaks in the PSD could be correlated with baryon cycling processes, and bears further investigation in future work. In particular, the evolution of the break time-scales with stellar mass in different models could help us understand why some studies show a significant mass-dependent trend while others do not. However, since mergers and other factors also play a role at these time-scales, their effects also need to be accounted for in such an analysis.

The ∼1 dex excess in the power of SFHs compared to DMAHs after accounting for quenching could correspond to contributions from baryonic processes like mergers and baryon cycling occurring on halo dynamical time-scales as the galaxy grows, leading to imprints in the PSD on time-scales $\propto 2\pi\tau_{\rm dyn} \sim 2\pi(0.1\tau_{\rm H}) \sim$ 2.1−8.6 Gyr over the past ∼10 Gyr.[14] Since the dynamical time grows with decreasing redshift, the resulting contribution to the PSD would end up being smoothed out over a broad range of time-scales. The plateau in simulations like Illustris and IllustrisTNG and individual galaxies in the zoom simulations at ∼1−3 Gyr are also indicative of a decorrelation time-scale that naturally arises in damped random walk models of star formation (Caplar & Tacchella 2019; Tacchella et al. 2020).

4.1.5 Quenching

Quenching in central galaxies can happen due to a lot of different factors – the shock heating of virial halo gas preventing cold-mode accretion (Dekel & Birnboim 2006), energy from AGN jets that heat gas and prevent it from forming stars (Somerville et al. 2008) and outflows that could remove cold gas from the galaxy (Di Matteo et al. 2005). Observational scaling relations like the $M_{\rm BH}-\sigma$ correlation tie behaviour on large (galaxy-wide) scales to sub-kpc scales on which SMBHs grow, leading to a unique scenario where sub-grid recipes for implementing BH growth and feedback affect when and how galaxies quench. In addition to this, recipes for how simulations implement cooling and star formation, and the strength of winds that blow gas out of galaxies all contribute to the overall trends seen in galaxy quiescence. Finally, the haloes of galaxies set the inflow rate of gas into the central galaxy, as seen through the correlation on long time-scales between the DMAHs and *in situ* SFHs. This dependence could tie the fuelling of the central AGN to that parent

[12] ∼35−60 Myr for Sandra in Justice League, Rogue in Marvel and in m12m, m11e, m11d, m11i, m11v, and m12i in FIRE-2.

[13] ∼60−90 Myr for h986 from g14 and for m12b, m11f, m11i, m11g, m11c in FIRE-2.

[14] Although it is outside the scope of the current work, it would be an interesting exercise to model the excess in the SFH PSDs as an aggregate effect of baryonic processes across a range of redshifts using a broken power-law model with $\tau_{\rm break} \sim 2\pi\tau_{\rm dyn}(z)$, based on the formalism described in Caplar & Tacchella (2019) and Tacchella et al. (2020).

halo, ultimately determining when the onset of quenching occurs (Chen et al. 2020).

Fig. 6 in Wright et al. (2019) shows a broad, unimodal distribution of quenching time-scales in EAGLE galaxies extending out to τ_H with a median of $\sim$2.5−3.3 Gyr for low-mass centrals and at shorter time-scales (median of $\sim$1.7−2.1 Gyr) for high-mass centrals depending on the definition of quenching time-scale. Longer quenching time-scales at low masses are associated with stellar feedback prolonging star formation activity, while shorter time-scales at high masses are associated with AGN activity. Simba, on the other hand, shows a bimodal distribution of quenching time-scales (Rodríguez Montero et al. 2019), with a slow mode acting approximately over a dynamical time ($t_Q \sim 0.1\tau_H$) that is more numerous overall for central galaxies, and a fast mode ($t_Q \sim 0.01\tau_H$) that dominates at stellar masses of $M_* \sim 10^{10}-10^{10.5}M_\odot$. The fast quenching mode is associated with AGN jet quenching causing a rapid cessation of accretion, since it becomes active at this mass range, and merger rates are not preferentially elevated at these masses. Additionally, X-ray feedback can rapidly evacuate the central regions of galaxies (Appleby et al. 2020) and contribute to short-time-scale variability. Sales et al. (2015) find a quenching time-scale of $\sim$2−5 Gyr for galaxies in Illustris. Nelson et al. (2018a) find the colour-transition time-scale, a tracer of the quenching time-scale, to be $\sim$0.7−3.8 Gyr for IllustrisTNG galaxies. Additionally, Joshi et al. (2020) find that morphological transformations in IllustrisTNG clusters occur on time-scales of $\sim$0.5−4 Gyr after accretion, with a control group showing a broader distribution. They also find that morphological transformation lags $\sim$1.5 Gyr behind quenching for gas-poor discs, while it precedes quenching by $\sim$0.5 Gyr for gas rich cluster galaxies, and by $\sim$2.5 Gyr for gas-rich control galaxies.

In studying the excess PSD power on different time-scales and stellar masses due to quenching, we find that the excess variability in IllustrisTNG on short time-scales rises strongly at $M_* \geq 10^{10.5}M_\odot$, correlated with the onset of strong kinetic-mode AGN feedback at $M_{BH} \sim 10^{8.5}M_\odot$ (Weinberger et al. 2018). While we are not in a position to speculate about time-scales of $0.01\tau_H$, we do find a tail of excess variability extending to the lowest time-scales in Simba that could be related to the jet-mode AGN feedback. In EAGLE, Wright et al. (2019) find that galaxies at low masses quench primarily due to stellar feedback on long time-scales, consistent with the excess power we see on time-scales $\geq$2 Gyr. As galaxies grow more massive ($M_* \geq 10^{10.3}M_\odot$) mergers and black hole activity increase sharply, leading to overall shorter quenching times, and additional variability on all time-scales, as seen in Fig. 13. The excess power in the SAMs at high masses seems to be primarily due to increased stochastic starbursts triggered by mergers and AGN activity (Somerville et al. 2008). The increasingly featureless (scale-free) nature of the PSDs towards high stellar masses, where the fraction of quenched galaxies is the largest, could be due to the contribution to the PSD from quenching dominating all other contributions.

Since a combination of multiple processes is responsible for quenching at different stellar masses, it is difficult to constrain their relative strengths with observational measurements of quenching time-scales. However, since these different processes also induce varying amounts of short-time-scale variability, constraints in PSD space might be able to distinguish between processes and allow for better constraints on their relative strengths.

4.2 Observational constraints in PSD space

For the different galaxy evolution models we consider in Section 3, we see a large diversity in the amount of power in SFR fluctuations on a given time-scale, the coupling between adjacent time-scales, and the existence and location of breaks in the PSD. This makes the PSD a sensitive probe of both the strengths of physical processes and their numerical implementation in these models. Observational constraints in this space are therefore extremely important, and will allow us to better constrain the relative strengths of different processes for a population of galaxies at a given stellar mass and epoch. These observational constraints can come in three forms: (i) constraints in PSD space obtained by measuring the SFR variability of ensembles of galaxies, which can be compared to the models we study, (ii) constraints on the time-scales for observed phenomena like quenching or rejuvenation, which can be tied to breaks or peaks in the PSD, and (iii) constraints on time-scales of physical processes, which can be used to isolate the effects of different processes contributing to the PSD on a given time-scale. In this section, we will briefly discuss each of these.

4.2.1 Ensemble constraints on SFR variability

The spectral energy distributions (SEDs) of galaxies are composed of spectrally distinct contributions from stellar populations formed at different ages relative to the time of observation. Interpreting these contributions gives us access to SFRs averaged over different time-scales. Nebular emission from the regions near short-lived O- and B-type stars provides constraints on SFR over the most recent $\sim$4−10 Myr (Madau & Dickinson 2014). The rest-UV portion of the SED contains contributions from young stars that probe the SFR out to $\sim$30−100 Myr, with a similar time-scale probed by the rest-FIR portion of the SED, which contains the re-emitted light from the young stellar light absorbed by dust. In addition to this, features like the strength of Hδ absorption and the 4000 Å break are sensitive to SFR within the last $\sim$1 Gyr and to the light-weighted age within $\sim$2 Gyr, respectively (Kauffmann et al. 2006; Wang & Lilly 2020b).

To get constraints in PSD space, it is useful to consider the SFR distributions for populations of galaxies and compare these distributions on different time-scales to quantify a relative change in burstiness.[15] While this straightforward to forward-model for the large-volume models, the small number of zoom galaxies make this a more involved procedure while considering those models. In these cases, a workaround is possible by realizing samples from the PSDs of zoom galaxies, similar to the procedure followed in Tacchella et al. (2020). In terms of the PSD formalism, this is equivalent to an observational constraint on the slope of the PSD between two time-scales. This has been done for select time-scales and populations of galaxies in Guo et al. (2016), Broussard et al. (2019), and Emami et al. (2019). More recently, Caplar & Tacchella (2019), and Wang & Lilly (2020a, b) have performed analyses motivated by the PSD formalism to constrain the slope of the PSD and other features in its shape. Most relevant to the current work, Caplar & Tacchella (2019) fit broken power-law models to galaxy fluctuations around the star-forming sequence at $z \sim 0$ with $M_* = 10^{10}-10^{10.5}M_\odot$. With degeneracies due to current observational uncertainties, they find that they cannot constrain both a slope and break time-scale, but find a break time-scale of $\sim$200 Myr assuming a slope of $\beta = 2$. Wang & Lilly (2020a) extend this analysis in a spatially resolved direction and find PSD slopes of $\beta \sim 1-2$ in the time-scale range of $\sim$5 to

[15]This makes an inherent assumption of ergodicity, that the PSDs obtained from a population of galaxies can be connected to the PSDs of individual galaxy SFHs over time. This assumption is explored in detail in Wang & Lilly (2020a).

∼800 Myr, assuming no break in the PSD (which implies that SFHs are correlated over the age of the universe). They also find that the slopes generally decrease with stellar mass for $M_* > 10^9 M_\odot$, and are correlated with estimated gas depletion time-scales in galaxies. Going forwards, these novel measurements can be used to constrain free parameters in the different models, and existing models can be used to make predictions for future observations with upcoming facilities like *JWST* and WFIRST.

4.2.2 *Constraints on the time-scales for observed phenomena*

Combining the spectral features from distant galaxies across a range of wavelengths in a full SED fitting code allows us to estimate the SFHs of individual galaxies with uncertainties (Heavens, Jimenez & Lahav 2000; Tojeiro et al. 2007; Pacifici et al. 2012; Smith & Hayward 2015; Pacifici et al. 2016; Iyer & Gawiser 2017; Leja et al. 2017; Carnall et al. 2018; Iyer et al. 2019; Leja et al. 2019a). While these observationally derived SFHs are not sensitive to variability on short time-scales, they can be useful for measuring the time-scales for morphological transformations, mergers, quenching and rejuvenation, and even recent starbursts. These time-scales can then be linked to features in the PSDs of galaxy SFHs, such as peaks or breaks.

Pacifici et al. (2016) analyse a sample of quiescent galaxies from CANDELS at $0.2 < z < 2.1$ and find quenching time-scales to be ∼2−4 Gyr, with a strong mass dependence. Carnall et al. (2018) study a sample of quiescent galaxies from UltraVISTA at $0.25 < z < 3.75$ and find that the majority of galaxies quench on time-scales of $\sim 0.4\tau_H$, with a rising set of galaxies towards the lower redshift portion of their observations with quenching time-scales $\sim 0.6\tau_H$. Iyer et al. (2019) analysed a sample of CANDELS galaxies at $0.5 < z < 3.0$ and found that ∼ 15–20 per cent of galaxies showed evidence for multiple strong episodes of star formation, with the median time-scale separating multiple peaks to be $\sim 0.4\tau_H$, which matches the predictions using cosmological simulations by Tacchella et al. (2016). The study also found that the SFHs of galaxies were correlated with their morphological classification, with an elevation in SFR on time-scales over the last ∼0.5 Gyr in galaxies classified as mergers and interactions, and with a longer period of SFR decline for spheroids compared to discs.

A number of studies (Lotz et al. 2011; Snyder et al. 2017; Duncan et al. 2019) also use statistical estimates of the physical properties of galaxies to constrain merger rates and observability time-scales. Pandya et al. (2017) use a similar statistical approach to quantify the time-scales on which galaxies experience quenching and rejuvenation by studying the relative number of galaxies that are star forming, quiescent, and transitioning between the two states at a given epoch.

Current observational techniques require a certain set of modeling assumptions, such as a choice of IMF, stellar population synthesis (SPS) model, and dust attenuation law. Combined with state-of-the-art observations, this leads to uncertainties of ∼0.2 dex in estimating stellar masses, and ∼0.3 dex in estimating SFRs from SED fitting, with fractional uncertainties in SFR growing large as we go to lower values of SFR and older stellar populations. Caution should be exercised in analysing the variability across different time-scales using these derived physical properties, with care taken in propagating measurement uncertainties and instrumental effects in observations to uncertainties on their estimated physical properties. One example of this procedure is in accounting for the difference between the observed and intrinsic scatter in the SFR–M_* correlation due to measurement uncertainties (Kurczynski et al. 2016; Boogaard et al. 2018), which would potentially affect the PSD slope described earlier in this section.

That being said, techniques to model and extract SFH information from galaxy SEDs are growing increasingly sophisticated (Iyer et al. 2019; Leja et al. 2019b), and are (i) better at estimating the older star formation in galaxies, (ii) using fully Bayesian techniques accounting for possible covariances between parameters, and (iii) implementing well motivated priors being used to break degeneracies between parameters like dust, metallicity, and SFH. With this in mind, it is hoped that in addition to time-scales, SFHs from upcoming surveys will also be able to provide direct constraints on PSD slope and power on the longest time-scales. Functionally, this provides a way to infer the same information as the first class of constraints on these time-scales, although in this case the time-scales are estimated from the histories of individual objects as opposed to recent burstiness of ensembles of galaxies. This would, in principle, allow us to independently verify estimated time-scales, and test the assumption of ergodicity inherent to constraints on the PSD obtained using ensembles of galaxies.

4.2.3 *Constraints on the time-scales of physical processes*

In addition to the two approaches described above, observations can also directly measure time-scales for gas depletion (Kennicutt 1998; Wong & Blitz 2002; Bigiel et al. 2008), stellar winds (Sharp & Bland-Hawthorn 2010; Ho et al. 2016), disc formation (Kobayashi, Springel & White 2007), bulge growth (Lang et al. 2014; Tacchella et al. 2015), black hole growth (Hopkins et al. 2005) and more, albeit for limited samples of galaxies. On short time-scales, a large body of work also exists studying GMC lifetimes (∼10−30 Myr) (Kruijssen et al. 2019; Zanella et al. 2019; Chevance et al. 2020), measuring the extent to which this depends on environment, and the extent to which it is decoupled from galactic dynamics. Krumholz, Kruijssen & Crocker (2017) also find episodic starbursts lasting ∼5−10 Myr with intervals of ∼20−40 Myr in a ring around the Milky-Way's central molecular zone. Equivalent behaviour in the zoom galaxies would therefore manifest as a local peak in the PSD on those time-scales. In the local Universe, resolved observations of stellar populations allow us to constrain the SFHs of nearby galaxies using colour–magnitude diagrams (Weisz et al. 2011a). For galaxies where stellar populations can be resolved, additional time-scale information can be obtained from chemical abundances, since the production of heavy elements by different types of supernovae trace a range of intermediate time-scales (Kobayashi et al. 2007; Kobayashi & Nomoto 2009). However, the masses of these galaxies are often too low to compare against the large-volume models considered in the current work. Another interesting study along these lines uses the fact that supernovae are produced at a certain rate after an episode of star formation to compute the delay time distributions of SN Ia using SN Ia yields in conjunction to observationally measured galaxy SFHs (Strolger et al. 2020). These constraints on the time-scales of physical processes allow for better modelling of the individual components that contribute to the full PSD of a galaxy's SFH, and sometimes provide an independent check of behaviour predicted using the PSDs.

Using the PSD formalism as our basis, it is therefore possible to constrain the PSD power on certain time-scales or the PSD slope on certain time-scale ranges using observations, with currently available data already starting to provide initial estimates of PSD slopes on ∼4−800 Myr time-scales. Taken together, the three types of constraints outlined above, i.e. (i) estimates of SFR variability using ensembles of galaxies, (ii) observationally measured time-

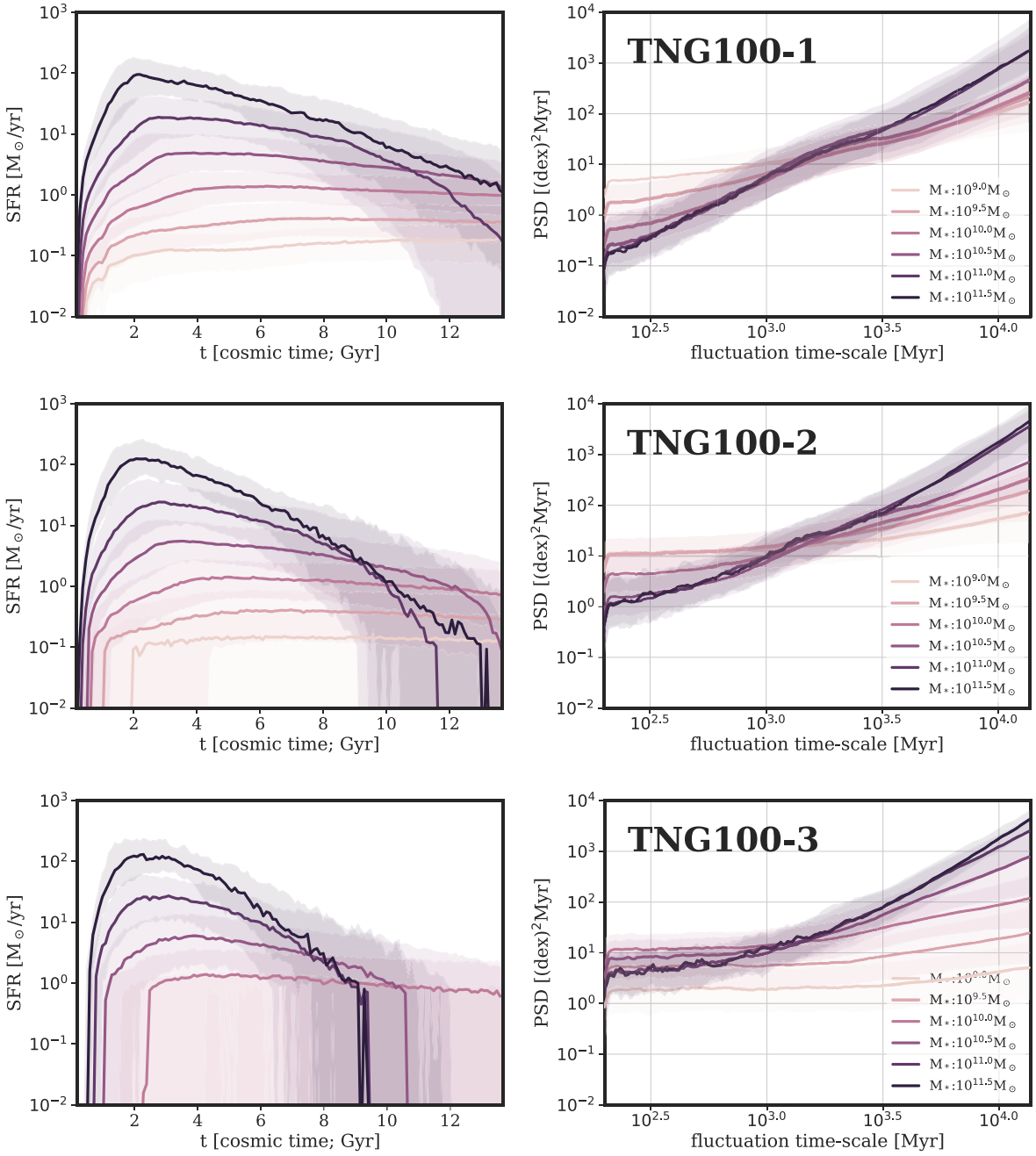

Figure 17. Exploring the effects of decreasing resolution (increasing star particle masses) on the SFHs and corresponding PSDs of galaxies using the IllustrisTNG simulation ($M_* = 9.44 \times 10^5 \mathrm{M}_\odot\ h^{-1}$, $M_* = 7.55 \times 10^6 \mathrm{M}_\odot\ h^{-1}$, and $M_* = 6.04 \times 10^7 \mathrm{M}_\odot\ h^{-1}$, respectively, for the three). Decreasing the resolution leads to a boost of power on short time-scales due to increased contribution of shot-noise from discrete star particles. This manifests as a 'white noise' floor in the PSDs that prevents us from probing the PSD to shorter time-scales.

scales for phenomena like quenching, starbursts, and rejuvenation, and (iii) time-scales for physical processes like gas depletion and GMC formation and destruction will allow us to compare features in the PSD such as slopes and peaks across different galaxy populations.

4.3 Effects of resolution

In order to investigate the effects of resolution of the numerical simulation, we consider three realizations of the TNG100 simulation (TNG100-1, 2, and 3), which are identical except for resolution. These are described in further detail in Pillepich et al. (2018b), and contain star particles with initial masses of $9.44 \times 10^5 \mathrm{M}_\odot\ h^{-1}$, $7.55 \times 10^6 \mathrm{M}_\odot\ h^{-1}$, and $6.04 \times 10^7 \mathrm{M}_\odot\ h^{-1}$, respectively. Mufasa and Simba therefore fall somewhere between TNG100-2 and TNG100-3 in terms of resolution, while EAGLE is comparable to TNG100-1. We show the SFHs and corresponding PSDs for these runs in Fig. 17.

In SFH space, we see that the different resolutions have a large impact on SFHs across all masses, especially in the portions with low SFRs. For the three simulations, with our adopted 100 Myr time bins, the lowest SFRs we can probe are $\approx 10^{-2.02}$, $10^{-1.12}$, and

$10^{0.68}$ $M_{\odot}yr^{-1}$ neglecting mass-loss. We see this in effect as the median SFHs for low-mass galaxies grow increasingly dominated by shot-noise and in the case of TNG100-3, completely drop off the plot. This resolution effect also affects high-mass quiescent galaxies, which leads to the apparent more rapid quenching of the median SFHs in the highest mass bins. This is simply because the SFRs can only drop to their minimum value from the quantum of SFR given the resolution, leading to a steeper apparent drop in the SFHs.

In PSD space, we see that the effect of lower resolution is to increase the amount of white-noise in the PSDs, which manifests as a flattening to spectral slopes of 0 towards shorter time-scales. In addition to affecting the PSDs to higher masses, the white noise also increases in magnitude proportional to the mass of the star particles, leading to contamination at longer time-scales in a given stellar mass bin. This effect is quantified in the analysis of Appendix A.

While resolution can be a limiting factor in any analysis of small-scale features in hydrodynamical models, convergence tests on individual simulations (Genel et al. 2019; Keller et al. 2019), and forward modelling the effects of discrete star particles as in Appendix A allow us to understand and account for these limitations. In this case, resolution effects mostly prevent us from studying the behaviour of the PSDs on small time-scales, which can be circumvented using the zoom simulations, which have much higher resolution. It should also be noted that the location of the breaks in the PSD listed in Section 3 are robust to resolution, although their strengths can be affected by the amount of white noise. Therefore, breaks and peaks in the PSD of simulations should be carefully compared to observations (see also Section 4.2).

4.4 Going forward: physics versus numerics

The considerable differences between the PSD slopes and power across the different models seen in Fig. 11 are caused in part due to the different modelling assumptions for physical processes, for example, AGN seeding, growth and feedback, star formation and stellar feedback and processes governing galactic winds. These differences are also in part due to the resolution of the simulations, as seen in Section 4.3 and numerical techniques used to implement gravity and magnetohydrodynamics (MHD), ranging from no explicit treatment of MHD in empirical and semi-analytic models, to differences between smoothed particle hydrodynamics, adaptive mesh refinement schemes and other hybrid techniques in hydrodynamical simulations (e.g. Kereš et al. 2012; Sijacki et al. 2012; Vogelsberger et al. 2012) using codes like AREPO (Springel 2010) in Illustris and IllustrisTNG, GIZMO (Hopkins 2014) in FIRE-2, Mufasa and Simba, a forked version of GADGET-3 (Springel et al. 2005) in EAGLE, Gasoline (Wadsley et al. 2004) for the g14 suite, and ChaNGa (Menon et al. 2015) for the Marvel/Justice League suite of zoom simulations.

While the current work serves to illustrate the cumulative differences between models due to choices of numerical techniques and physical models, it is outside the scope of the current work to break down the individual contributions. Building on the current work, there are three directions in which we can begin to better connect individual physical processes to their relevant time-scales in a model-independent way:

(i) Tacchella et al. (2020) propose an analytical model in PSD space using the gas regulator model of galaxy evolution (Lilly et al. 2013), extending the model to account for the creation and destruction of GMCs on short time-scales. Using this model, they derive the PSD as a broken power law with multiple breaks that characterize the equilibrium time-scale of gas inflow and the average lifetime of GMCs. Applied to PSDs from the different models we consider, this can explain the effective time-scales for these processes across the various models.

(ii) In a slightly different direction, many of the models we consider have run additional simulations varying the input physics. For example, there is a set of 25 Mpc^3 boxes run for Illustris-TNG varying a single parameter per run, including stellar and black hole feedback mechanisms, galactic wind scalings, and aspects of star formation (Nelson et al. 2018b; Pillepich et al. 2018a). The Simba model contains additional simulations varying the AGN feedback model (Davé et al. 2019). Crain et al. (2015) describe model variations within the EAGLE suite varying stellar and AGN feedback. Choi et al. (2017) contains a suite of zoom simulations that are run with and without AGN feedback. The Santa Cruz SAM and other semi-analytic models are also capable of being run multiple times varying model parameters.
Using all of this data, it should be possible to characterize the effects of varying physical modelling assumptions with individual models, and use this across several models to understand the general trends and time-scales for physical processes like stellar and AGN feedback and baryon cycling. However, as Pillepich et al. (2018a) note, 'the optimal choices for wind as well as black hole feedback strongly depend on the *whole ensemble* of galaxy formation mechanisms incorporated into the model.' What holds for a given model need not generalize across all models, and extreme caution should be exercised while extrapolating trends from individual models, using the full available range of observational constraints described in Section 4.2 as benchmarks.

(iii) Further studies will also be needed to investigate the link between the well-studied effects of spatial turbulence on star formation (Larson 1981; Krumholz & McKee 2005; Nakamura & Li 2005; Padoan & Nordlund 2011) and the natural emergence of power-law spatial correlation functions (Guszejnov, Hopkins & Grudić 2018) to its temporal manifestations studied in this work. Studies like di Leoni, Cobelli & Mininni (2015), which look at the joint spatiotemporal power spectra for numerical simulations of turbulent flows to identify the signatures of physical mechanisms, provide a useful starting point in this regard.

5 CONCLUSIONS

A range of physical processes acting on different time-scales regulate star formation within galaxies. Processes that act concomitantly over an overlapping range of time-scales have complicated effects, and render it impractical to estimate the time-scale of one process independently of the other. The resulting process of galaxy growth is therefore diverse, and understanding the impact of the underlying processes across all time-scales simultaneously can help explain this diversity.

Using the PSD formalism, we quantify the variability of galaxy SFHs on different time-scales for a wide range of galaxy evolution models and find:

(i) **Overall trends:** The PSDs of galaxy SFHs are well described by broken power-law characteristic of stochastic processes, in line with theoretical descriptions by Kelson (2014), Caplar & Tacchella (2019), and Kelson et al. (2020) with most of the power lying on long ($\gtrsim$1 Gyr) time-scales. Across the full range of time-scales investigated in this work ($\sim$200 Myr to 10 Gyr), the PSDs of galaxies with $M_* \sim 10^{10} M_{\odot}$ show a median slope of $\beta \sim 1.6 \pm 0.84$, increasing smoothly with mass to $\beta \sim 2.1 \pm 0.68$ at $M_* \sim 10^{11.5} M_{\odot}$.

(ii) Although most models show comparable mass functions and similar overall behaviour in their SFHs, the specific PSD slope and power at any time-scale can vary considerably across the different models. The PSD power can vary by up to an order of magnitude at a given time-scale and stellar mass. Similarly, the local PSD slope can vary by $\sim$1.5 at a given time-scale and stellar mass.[16] Steeper slopes result in a larger fraction of the overall SFH power being concentrated on longer time-scales. Interestingly, some models show a flattening of the slope at intermediate ($\sim$1$-$3 Gyr) time-scales, indicating that the SFHs decorrelate (i.e. lose memory) on these time-scales.

(iii) **PSD shape between models:** IllustrisTNG shows more variability on intermediate time-scales compared to Illustris, as does Simba when compared to Mufasa. Updated feedback models (particularly for AGN feedback) in both of these simulations likely account for this. The UniverseMachine PSDs look quite self-similar, since the SFHs are closely tied to the DM-accretion histories of their parent haloes. The FIRE-2 simulations, with their significantly higher resolution and more explicit feedback, show greater contributions at shorter time-scales compared to the semi-analytic and empirical models. The g14 and Marvel/Justice League simulations, which have comparable resolution to FIRE-2, show less variability across a range of time-scales and a sharper trend for increasing burstiness with decreasing stellar mass.

(iv) **Breaks in the PSD:** Illustris, IllustrisTNG, the SC-SAM, and the zoom simulations show distinct breaks in their PSDs at several time-scales across the different stellar mass bins. These breaks become less prominent with increasing stellar mass, with the PSDs approaching a scale-free power law with slope $\beta \sim 2$. Mufasa, Simba, EAGLE, and UniverseMachine show a smooth increase in slope towards longer time-scales, with the slope being constant at time-scales $\gtrsim$3 Gyr. These breaks could stem from physical processes acting within galaxies, such as GMC lifecycle, dynamical processes, and gas regulation (Tacchella et al. 2020).

(v) **DMAHs:** The DMAHs of galaxies show self-similar behaviour across different stellar mass bins with a median power-law slope of $\beta \sim 1$, consistent with the analytic derivation by Kelson et al. (2020). DMAHs do not contribute significantly to the overall variability of SFHs, except on the shortest time-scales ($\lesssim$400 Myr). The excess power in SFH PSDs compared to those of the DMAHs increases to long time-scales, and is likely due to a combination of mergers, baryon cycling and AGN feedback.

(vi) Studying the coherence between the PSDs of the full versus *in situ* SFHs shows that mergers are responsible for decorrelating the two at short time-scales. Since mergers are effectively stochastic events, there is no preferred time-scale for this decorrelation, with the coherence falling off smoothly towards shorter time-scales. Since higher mass galaxies experience more mergers, the decoherence is also a function of the stellar mass.

(vii) The *in situ* SFHs are coherent with the DM accretion histories of their parent haloes on long time-scales ($\gtrsim$3 Gyr), independent of stellar mass. This coherence is likely due to the growth of a galaxy's parent halo determining the fuelling and therefore the subsequent star formation in its central galaxy. The decline in coherence quantifies the increasing importance of baryonic physics in regulating SFR on shorter time-scales.

(viii) **Variability on short time-scales:** A number of models display a trend of increasing power on short time-scales ($\sim$200$-$300 Myr) with decreasing stellar mass, i.e. lower mass galaxies are burstier. This is notable for some of the large-volume hydrodynamical simulations (Illustris, IllustrisTNG, Mufasa, and EAGLE) and the zoom simulations (g14 and Marvel/Justice League and FIRE-2), while short-time-scale power in the Santa-Cruz SAM, UniverseMachine and DM accretion histories is largely invariant as a function of stellar mass. Since the latter three models are most closely linked to halo merger trees, their lack of burstiness suggests that this shorter time-scale behaviour is due to hydrodynamical feedback mechanisms that are not adequately captured by these models.

(ix) **Zoom simulations:** The zoom simulations are a good test-bed to study the time-dependent variability of SFHs on shorter time-scales, with their higher resolution allowing us to probe their PSDs to the much shorter time-scales on which GMCs are created and destroyed. Studying galaxies from the FIRE-2 and g14 and Marvel/Justice League zoom suites, the broken power-law behaviour of the PSDs is found to continue to nearly an order of magnitude below the time-scales studied in the rest this work. The power in the zoom PSDs on long time-scales is generally lower than their large-volume counterparts. Galaxies in FIRE-2 generally have more power on short time-scales compared to galaxies in g14 and Marvel/Justice League, although the trend of increasing short-time-scale 'burstiness' to lower masses is stronger in the latter.

(x) **The effects of quenching on PSDs:** Separating galaxies into star-forming and quiescent populations in a given mass bin allows us to quantify the excess strength in the PSD due to the physical processes responsible for quenching. This excess power at a given time-scale can be nearly an order of magnitude, with the dependence on stellar mass, the existence of a quenching time-scale, and the behaviour of the PSDs below this quenching time-scale varying widely across the different models.

The PSD formalism allows us to quantify the strength of SFR fluctuations on different time-scales. Studying the SFHs of galaxies from different models of galaxy evolution shows large differences in PSD space, due to differences in resolution and the implementation of sub-grid recipes. In conjunction with these models, observational measurements of SFR variability on different time-scales will provide a useful new constraints on the relative strengths of the different physical processes that regulate star formation in galaxies.

ACKNOWLEDGEMENTS

We would like to thank the anonymous referee for their insightful comments. We would like to thank Phil Hopkins, Ena Choi, Viraj Pandya, Yuan Li, Harry Ferguson, Gwen Eadie, and Bryan Gaensler, and the entire the KSPA 2018 cohort for productive discussions and comments, and Peter Behroozi for making the UniverseMachine SFHs publicly available. KI gratefully acknowledges support from Rutgers University and from the Dunlap Institute for Astronomy and Astrophysics through the Dunlap Postdoctoral Fellowship. The Dunlap Institute is funded through an endowment established by the David Dunlap family and the University of Toronto. ST is supported by the Smithsonian Astrophysical Observatory through the CfA Fellowship. This work was initiated as a project for the Kavli Summer Program in Astrophysics held at the Center for Computational Astrophysics of the Flatiron Institute in 2018. The Flatiron Institute is supported by the Simons Foundation. KI and ST thank them for their generous support. We acknowledge the Virgo Consortium for making their simulation data available. The EAGLE simulations were performed using the DiRAC-2 facility at Durham, managed by the ICC, and the PRACE facility Curie based

[16] An interactive plot allowing the user to explore the PSD slope and power for the various models at different time-scales can be found online at this link: https://kartheikiyer.github.io/psd_explorer.html

in France at TGCC, CEA, Bruyères-le-Châtel. Resources supporting the g14/Marvel/JL simulations were provided by the NASA High-End Computing (HEC) Program through the NASA Advanced Supercomputing (NAS) Division at Ames Research Center. Support for Program number *HST*-AR-14564.001-A was provided by NASA through a grant from the Space Telescope Science Institute, which is operated by the Association of Universities for Research in Astronomy, Incorporated, under NASA contract NAS5-26555.

Software: ASTROPY (Astropy Collaboration 2013; Price-Whelan et al. 2018), ASTROML (VanderPlas et al. 2012), COMMAH (Correa et al. 2015), MATPLOTLIB (Caswell et al. 2019), SCIPY (Virtanen et al. 2020), NUMPY (Walt, Colbert & Varoquaux 2011), and CORNER (Foreman-Mackey 2016).

DATA AVAILABILITY STATEMENT

The data underlying this article will be shared on request to the corresponding author. Raw data for some of the models studied in this work are publicly available at the following repositories: Illustris (https://www.illustris-project.org/data/), IllustrisTNG [https://www.tng-project.org/data/, Nelson et al. (2019)], EAGLE [(http://icc.dur.ac.uk/Eagle/database.php, McAlpine et al. (2016)], Simba (http://simba.roe.ac.uk/), and UniverseMachine (https://www.peterbehroozi.com/data.html).

REFERENCES

Anglés-Alcázar D., Faucher-Giguère C.-A., Kereš D., Hopkins P. F., Quataert E., Murray N., 2017a, MNRAS, 470, 4698
Anglés-Alcázar D., Faucher-Giguère C.-A., Quataert E., Hopkins P. F., Feldmann R., Torrey P., Wetzel A., Kereš D., 2017b, MNRAS, 472, L109
Appleby S., Davé R., Kraljic K., Anglés-Alcázar D., Narayanan D., 2020, MNRAS, 494, 6053
Astropy Collaboration, 2013, A&A, 558, A33
Barnes J. E., Hernquist L., 1996, ApJ, 471, 115
Barnes J. E., Hernquist L. E., 1991, ApJ, 370, L65
Behroozi P., Wechsler R. H., Hearin A. P., Conroy C., 2019, MNRAS, 488, 3143
Behroozi P. S., Wechsler R. H., Conroy C., 2013, ApJ, 770, 57
Bellovary J. M., Cleary C. E., Munshi F., Tremmel M., Christensen C. R., Brooks A., Quinn T. R., 2019, MNRAS, 482, 2913
Bell E. F., 2008, ApJ, 682, 355
Benincasa S. M. et al., 2020, MNRAS, 497, 3993
Bigiel F., Leroy A., Walter F., Brinks E., De Blok W., Madore B., Thornley M. D., 2008, AJ, 136, 2846
Bond J. R., Cole S., Efstathiou G., Kaiser N., 1991, ApJ, 379, 440
Boogaard L. A. et al., 2018, A&A, 619, A27
Bothun G., ed., 1998, Modern Cosmological Observations and Problems. CRC press, p. 619
Bouché N. et al., 2010, ApJ, 718, 1001
Boylan-Kolchin M., Ma C.-P., Quataert E., 2008, MNRAS, 383, 93
Brennan R. et al., 2017, MNRAS, 465, 619
Brooks A., Christensen C., 2015, in Laurikainen E., Peletier R. F., Gadotti D. A., eds, Galactic Bulges. Springer International Publishing, p. 317
Brooks A. M., Zolotov A., 2014, ApJ, 786, 87
Brooks A. M., Papastergis E., Christensen C. R., Governato F., Stilp A., Quinn T. R., Wadsley J., 2017, ApJ, 850, 15
Broussard A. et al., 2019, ApJ, 873, 74
Bundy K. et al., 2008, ApJ, 681, 931
Caplar N., Tacchella S., 2019, MNRAS, 487, 3845
Caplar N., Lilly S. J., Trakhtenbrot B., 2017, ApJ, 834, 111
Carnall A., McLure R., Dunlop J., Davé R., 2018, MNRAS, 480, 4379
Carnall A. C. et al., 2020, MNRAS, 496, 695
Caswell T. et al., 2019, matplotlib/matplotlib v3. 1.0
Ceverino D., Klypin A., Klimek E. S., Trujillo-Gomez S., Churchill C. W., Primack J., Dekel A., 2014, MNRAS, 442, 1545
Chen Z. et al., 2020, ApJ, 897, 102
Chevance M. et al., 2020, MNRAS, 493, 2872
Choi E., Ostriker J. P., Naab T., Somerville R. S., Hirschmann M., Núñez A., Hu C.-Y., Oser L., 2017, ApJ, 844, 31
Christensen C., Quinn T., Governato F., Stilp A., Shen S., Wadsley J., 2012, MNRAS, 425, 3058
Christensen C. R., Davé R., Governato F., Pontzen A., Brooks A., Munshi F., Quinn T., Wadsley J., 2016, ApJ, 824, 57
Christensen C. R., Davé R., Brooks A., Quinn T., Shen S., 2018, ApJ, 867, 142
Ciesla L., Elbaz D., Fensch J., 2017, A&A, 608, A41
Conroy C., Gunn J. E., 2010, ApJ, 712, 833
Conroy C., Gunn J. E., White M., 2009, ApJ, 699, 486
Correa C. A., Wyithe J. S. B., Schaye J., Duffy A. R., 2015, MNRAS, 450, 1514
Cox T. J., Jonsson P., Somerville R. S., Primack J. R., Dekel A., 2008, MNRAS, 384, 386
Crain R. A., Eke V. R., Frenk C. S., Jenkins A., McCarthy I. G., Navarro J. F., Pearce F. R., 2007, MNRAS, 377, 41
Crain R. A. et al., 2015, MNRAS, 450, 1937
Dalla Vecchia C., Schaye J., 2012, MNRAS, 426, 140
Davé R., Finlator K., Oppenheimer B. D., 2012, MNRAS, 421, 98
Davé R., Thompson R., Hopkins P. F., 2016, MNRAS, 462, 3265
Davé R., Anglés-Alcázar D., Narayanan D., Li Q., Rafieferantsoa M. H., Appleby S., 2019, MNRAS, 486, 2827
Davis M., Efstathiou G., Frenk C. S., White S. D. M., 1985, ApJ, 292, 371
Dekel A., Birnboim Y., 2006, MNRAS, 368, 2
Dekel A., Sari R., Ceverino D., 2009, ApJ, 703, 785
Dekel A., Zolotov A., Tweed D., Cacciato M., Ceverino D., Primack J., 2013, MNRAS, 435, 999
di Leoni P. C., Cobelli P. J., Mininni P. D., 2015, Eur. Phys. J. E, 38, 136
Diemer B., Sparre M., Abramson L. E., Torrey P., 2017, ApJ, 839, 26
Di Matteo T., Springel V., Hernquist L., 2005, Nature, 433, 604
Dobbs C., Pringle J., Burkert A., 2012, MNRAS, 425, 2157
Dobbs C., Pringle J., Duarte-Cabral A., 2015, MNRAS, 446, 3608
Dolag K., Borgani S., Murante G., Springel V., 2009, MNRAS, 399, 497
Domínguez A., Siana B., Brooks A. M., Christensen C. R., Bruzual G., Stark D. P., Alavi A., 2015, MNRAS, 451, 839
Donnari M. et al., 2019, MNRAS, 485, 4817
Dressler A., Kelson D. D., Abramson L. E., 2018, ApJ, 869, 152
Duncan K. et al., 2019, ApJ, 876, 110
Emami N., Siana B., Weisz D. R., Johnson B. D., Ma X., El-Badry K., 2019, ApJ, 881, 71
Fang J. J., Faber S., Salim S., Graves G. J., Rich R. M., 2012, ApJ, 761, 23
Faucher-Giguère C.-A., 2018, MNRAS, 473, 3717
Feldmann R., 2017, MNRAS, 470, L59
Feldmann R., Faucher-Giguère C.-A., Kereš D., 2019, ApJ, 871, L21
Ferland G. J. et al., 2017, RMxAA, 53, 385
Forbes J. C., Lin D. N. C., 2019, AJ, 158, 124
Forbes J. C., Krumholz M. R., Burkert A., Dekel A., 2014a, MNRAS, 438, 1552
Forbes J. C., Krumholz M. R., Burkert A., Dekel A., 2014b, MNRAS, 443, 168
Foreman-Mackey D., 2016, J. Open Source Softw., 24, 1864
Gabor J. M., Davé R., 2015, MNRAS, 447, 374
Genel S. et al., 2014, MNRAS, 445, 175
Genel S. et al., 2019, ApJ, 871, 21
Gnedin N. Y., Kravtsov A. V., Chen H.-W., 2008, ApJ, 672, 765
Governato F. et al., 2009, MNRAS, 398, 312
Governato F. et al., 2012, MNRAS, 422, 1231
Grand R. J. J. et al., 2019, MNRAS, 490, 4786
Guo Y. et al., 2016, ApJ, 833, 37
Guszejnov D., Hopkins P. F., Grudić M. Y., 2018, MNRAS, 477, 5139
Haardt F., Madau P., 1996, ApJ, 461, 20
Haardt F., Madau P., 2012, ApJ, 746, 125
Hahn C., Tinker J. L., Wetzel A., 2019a, preprint (arXiv:1910.01644)

Hahn C. et al., 2019b, ApJ, 872, 160
Hanasz M., Kowal G., Otmianowska-Mazur K., Lesch H., 2004, ApJ, 605, L33
Hani M. H., Gosain H., Ellison S. L., Patton D. R., Torrey P., 2020, MNRAS, 493, 3716
Hayward C. C., Hopkins P. F., 2017, MNRAS, 465, 1682
Heavens A. F., Jimenez R., Lahav O., 2000, MNRAS, 317, 965
Hernquist L., 1989, Nature, 340, 687
Ho I.-T. et al., 2016, MNRAS, 457, 1257
Hopkins P. F., 2014, Astrophysics Source Code Library, record ascl:1410.003
Hopkins P. F., 2015, MNRAS, 450, 53
Hopkins P. F., 2017, preprint (arXiv:1712.01294)
Hopkins P. F., Hernquist L., Martini P., Cox T. J., Robertson B., Di Matteo T., Springel V., 2005, ApJ, 625, L71
Hopkins P. F., Hernquist L., Cox T. J., Di Matteo T., Robertson B., Springel V., 2006, ApJS, 163, 1
Hopkins P. F., Kereš D., Oñorbe J., Faucher-Giguère C.-A., Quataert E., Murray N., Bullock J. S., 2014, MNRAS, 445, 581
Hopkins P. F. et al., 2018, MNRAS, 480, 800
Hughes P. A., Aller H. D., Aller M. F., 1992, ApJ, 396, 469
Hung C.-L. et al., 2019, MNRAS, 482, 5125
Iyer K., Gawiser E., 2017, ApJ, 838, 127
Iyer K. G., Gawiser E., Faber S. M., Ferguson H. C., Kartaltepe J., Koekemoer A. M., Pacifici C., Somerville R. S., 2019, ApJ, 879, 116
Jeffreson S. M. R., Kruijssen J. M. D., 2018, MNRAS, 476, 3688
Jiang C. Y., Jing Y. P., Faltenbacher A., Lin W. P., Li C., 2008, ApJ, 675, 1095
Johnson B. D. et al., 2013, ApJ, 772, 8
Joshi G. D., Pillepich A., Nelson D., Marinacci F., Springel V., Rodriguez-Gomez V., Vogelsberger M., Hernquist L., 2020, MNRAS, 496, 2673
Kauffmann G. et al., 2003, MNRAS, 341, 33
Kauffmann G., Heckman T. M., De Lucia G., Brinchmann J., Charlot S., Tremonti C., White S. D. M., Brinkmann J., 2006, MNRAS, 367, 1394
Kaviraj S., Kirkby L. A., Silk J., Sarzi M., 2007, MNRAS, 382, 960
Kaviraj S., Schawinski K., Silk J., Shabala S. S., 2011, MNRAS, 415, 3798
Keller B. W., Wadsley J. W., Wang L., Kruijssen J. M. D., 2019, MNRAS, 482, 2244
Kelson D. D., 2014, preprint (arXiv:1406.5191)
Kelson D. D., Benson A. J., Abramson L. E., 2016, preprint (arXiv:1610.06566)
Kelson D. D. et al., 2020, MNRAS, 494, 2628
Kennicutt R. C., 1989, ApJ, 344, 685
Kennicutt R. C., Jr, 1998, ApJ, 498, 541
Kereš D., Katz N., Fardal M., Davé R., Weinberg D. H., 2009, MNRAS, 395, 160
Kereš D., Vogelsberger M., Sijacki D., Springel V., Hernquist L., 2012, MNRAS, 425, 2027
Khoperskov S. A., Khrapov S. S., 2018, A&A, 609, A104
Kim C.-G., Ostriker E. C., 2017, ApJ, 846, 133
Kimm T. et al., 2009, MNRAS, 394, 1131
Klypin A., Yepes G., Gottlöber S., Prada F., Hess S., 2016, MNRAS, 457, 4340
Klypin A. A., Trujillo-Gomez S., Primack J., 2011, ApJ, 740, 102
Kobayashi C., Nomoto K., 2009, ApJ, 707, 1466
Kobayashi C., Springel V., White S. D., 2007, MNRAS, 376, 1465
Kozłowski S., 2016, ApJ, 826, 118
Kroupa P., Tout C. A., Gilmore G., 1993, MNRAS, 262, 545
Kruijssen J. M. D. et al., 2019, Nature, 569, 519
Krumholz M., Burkert A., 2010, ApJ, 724, 895
Krumholz M. R., McKee C. F., 2005, ApJ, 630, 250
Krumholz M. R., McKee C. F., Tumlinson J., 2009, ApJ, 699, 850
Krumholz M. R., Kruijssen J. M. D., Crocker R. M., 2017, MNRAS, 466, 1213
Kulier A., Padilla N., Schaye J., Crain R. A., Schaller M., Bower R. G., Theuns T., Paillas E., 2019, MNRAS, 482, 3261
Kurczynski P. et al., 2016, ApJ, 820, L1
Lacey C., Cole S., 1993, MNRAS, 262, 627
Lang P. et al., 2014, ApJ, 788, 11
Larson R. B., 1981, MNRAS, 194, 809
Leitherer C. et al., 1999, ApJS, 123, 3
Leja J., Johnson B. D., Conroy C., van Dokkum P. G., Byler N., 2017, ApJ, 837, 170
Leja J., Carnall A. C., Johnson B. D., Conroy C., Speagle J. S., 2019a, ApJ, 876, 3
Leja J. et al., 2019b, ApJ, 877, 140
Lilly S. J., Carollo C. M., Pipino A., Renzini A., Peng Y., 2013, ApJ, 772, 119
Loebman S. R. et al., 2014, ApJ, 794, 151
Lotz J. M., Jonsson P., Cox T., Croton D., Primack J. R., Somerville R. S., Stewart K., 2011, ApJ, 742, 103
MacLeod C. L. et al., 2010, ApJ, 721, 1014
MacLeod C. L. et al., 2012, ApJ, 753, 106
Madau P., Dickinson M., 2014, ARA&A, 52, 415
Marcolini A., Brighenti F., D'Ercole A., 2004, MNRAS, 352, 363
Marinacci F. et al., 2018, MNRAS, 480, 5113
Matthee J., Schaye J., 2019, MNRAS, 484, 915
McAlpine S. et al., 2016, Astron. Comput., 15, 72
McQuinn K. B. et al., 2010, ApJ, 724, 49
Menon H., Wesolowski L., Zheng G., Jetley P., Kale L., Quinn T., Governato F., 2015, Comput. Astrophys. Cosmol., 2, 1
Mihos J. C., Hernquist L., 1994, ApJ, 425, L13
Mihos J. C., Hernquist L., 1996, ApJ, 464, 641
Mitra S., Davé R., Simha V., Finlator K., 2016, MNRAS, 464, 2766
Mo H., van den Bosch F. C., White S., 2010, Galaxy Formation and Evolution, Cambridge Univ. Press, Cambridge
Moster B. P., Naab T., White S. D. M., 2013, MNRAS, 428, 3121
Moster B. P., Naab T., White S. D., 2018, MNRAS, 477, 1822
Munshi F. et al., 2013, ApJ, 766, 56
Muratov A. L., Kereš D., Faucher-Giguère C.-A., Hopkins P. F., Quataert E., Murray N., 2015, MNRAS, 454, 2691
Naiman J. P. et al., 2018, MNRAS, 477, 1206
Nakamura F., Li Z.-Y., 2005, ApJ, 631, 411
Neistein E., van den Bosch F. C., Dekel A., 2006, MNRAS, 372, 933
Nelson D. et al., 2015, Astron. Comput., 13, 12
Nelson D. et al., 2018a, MNRAS, 475, 624
Nelson D. et al., 2018b, MNRAS, 477, 450
Nelson D. et al., 2019, Comput. Astrophys. Cosmol., 6, 2
O'Shaughnessy R., Bellovary J., Brooks A., Shen S., Governato F., Christensen C., 2017, MNRAS, 464, 2831
Oppenheimer B. D., Davé R., Kereš D., Fardal M., Katz N., Kollmeier J. A., Weinberg D. H., 2010, MNRAS, 406, 2325
Pacifici C., Kassin S. A., Weiner B., Charlot S., Gardner J. P., 2012, ApJ, 762, L15
Pacifici C., Oh S., Oh K., Lee J., Yi S. K., 2016, ApJ, 824, 45
Padoan P., Nordlund Å., 2011, ApJ, 730, 40
Pakmor R. et al., 2017, MNRAS, 469, 3185
Pandya V. et al., 2017, MNRAS, 472, 2054
Parrish I. J., Quataert E., Sharma P., 2009, ApJ, 703, 96
Peng Y.-j. et al., 2010, ApJ, 721, 193
Pillepich A. et al., 2018a, MNRAS, 473, 4077
Pillepich A. et al., 2018b, MNRAS, 475, 648
Porter L. A., Somerville R. S., Primack J. R., Johansson P. H., 2014, MNRAS, 444, 942
Press W. H., Schechter P., 1974, ApJ, 187, 425
Price-Whelan A. M. et al., 2018, AJ, 156, 123
Qu Y. et al., 2017, MNRAS, 464, 1659
Robaina A. R., Bell E. F., van der Wel A., Somerville R. S., Skelton R. E., McIntosh D. H., Meisenheimer K., Wolf C., 2010, ApJ, 719, 844
Robertson B., Cox T. J., Hernquist L., Franx M., Hopkins P. F., Martini P., Springel V., 2006a, ApJ, 641, 21
Robertson B., Bullock J. S., Cox T. J., Di Matteo T., Hernquist L., Springel V., Yoshida N., 2006b, ApJ, 645, 986
Rodriguez-Gomez V. et al., 2015, MNRAS, 449, 49
Rodríguez-Puebla A., Primack J. R., Behroozi P., Faber S., 2016, MNRAS, 455, 2592
Rodríguez-Puebla A., Behroozi P., Primack J., Klypin A., Lee C., Hellinger D., 2017, MNRAS, 462, 893

Rodríguez Montero F., Davé R., Wild V., Anglés-Alcázar D., Narayanan D., 2019, MNRAS, 490, 2139
Sales L. V. et al., 2015, MNRAS, 447, L6
Sartori L. F., Schawinski K., Trakhtenbrot B., Caplar N., Treister E., Koss M. J., Megan Urry C., Zhang C., 2018, MNRAS, 476, L34
Scannapieco E., Silk J., Bouwens R., 2005, ApJ, 635, L13
Schaller M., Dalla Vecchia C., Schaye J., Bower R. G., Theuns T., Crain R. A., Furlong M., McCarthy I. G., 2015, MNRAS, 454, 2277
Schaye J., Dalla Vecchia C., 2008, MNRAS, 383, 1210
Schaye J. et al., 2015, MNRAS, 446, 521
Schmidt M., 1959, ApJ, 129, 243
Schreiber C. et al., 2015, A&A, 575, A74
Semenov V. A., Kravtsov A. V., Gnedin N. Y., 2017, ApJ, 845, 133
Sharp R., Bland-Hawthorn J., 2010, ApJ, 711, 818
Shen S., Wadsley J., Stinson G., 2010, MNRAS, 407, 1581
Shivaei I. et al., 2018, ApJ, 855, 42
Sijacki D., Springel V., Di Matteo T., Hernquist L., 2007, MNRAS, 380, 877
Sijacki D., Vogelsberger M., Kereš D., Springel V., Hernquist L., 2012, MNRAS, 424, 2999
Smith B. D. et al., 2017, MNRAS, 466, 2217
Smith D. J., Hayward C. C., 2015, MNRAS, 453, 1597
Snyder G. F., Lotz J. M., Rodriguez-Gomez V., Guimarães R. D. S., Torrey P., Hernquist L., 2017, MNRAS, 468, 207
Somerville R. S., Davé R., 2015, ARA&A, 53, 51
Somerville R. S., Hopkins P. F., Cox T. J., Robertson B. E., Hernquist L., 2008, MNRAS, 391, 481
Somerville R. S., Popping G., Trager S. C., 2015, MNRAS, 453, 4337
Sparre M. et al., 2015, MNRAS, 447, 3548
Sparre M., Hayward C. C., Feldmann R., Faucher-Giguère C.-A., Muratov A. L., Kereš D., Hopkins P. F., 2017, MNRAS, 466, 88
Springel V., 2005, MNRAS, 364, 1105
Springel V., 2010, Proc. Int. Astron. Union, 6, 203
Springel V., Hernquist L., 2003, MNRAS, 339, 289
Springel V., White S. D. M., Tormen G., Kauffmann G., 2001, MNRAS, 328, 726
Springel V., Di Matteo T., Hernquist L., 2005, MNRAS, 361, 776
Springel V. et al., 2018, MNRAS, 475, 676
Stinson G., Seth A., Katz N., Wadsley J., Governato F., Quinn T., 2006, MNRAS, 373, 1074
Strolger L.-G., Rodney S. A., Pacifici C., Narayan G., Graur O., 2020, ApJ, 890, 140
Tacchella S. et al., 2015, Science, 348, 314
Tacchella S., Dekel A., Carollo C. M., Ceverino D., DeGraf C., Lapiner S., Mandelker N., Primack Joel R., 2016, MNRAS, 457, 2790
Tacchella S., Bose S., Conroy C., Eisenstein D. J., Johnson B. D., 2018, ApJ, 868, 92
Tacchella S. et al., 2019, MNRAS, 487, 5416
Tacchella S., Forbes J. C., Caplar N., 2020, MNRAS, 497, 698
Tan J. C., 2000, ApJ, 536, 173
Tasker E. J., 2011, ApJ, 730, 11
Thomas D., Kauffmann G., 1999, in Hubeny I., Heap S., Cornett R., eds, ASP Conf. Ser. Vol. 192, Spectrophotometric Dating of Stars and Galaxies. Astron. Soc. Pac., San Francisco, p. 261
Tojeiro R., Heavens A. F., Jimenez R., Panter B., 2007, MNRAS, 381, 1252
Torrey P. et al., 2018, MNRAS, 477, L16
Trayford J. W., Theuns T., Bower R. G., Crain R. A., Lagos C. d. P., Schaller M., Schaye J., 2016, MNRAS, 460, 3925
Tremmel M., Karcher M., Governato F., Volonteri M., Quinn T., Pontzen A., Anderson L., Bellovary J., 2017, MNRAS, 470, 1121
Tumlinson J., Peeples M. S., Werk J. K., 2017, ARA&A, 55, 389
Übler H., Naab T., Oser L., Aumer M., Sales L. V., White S. D. M., 2014, MNRAS, 443, 2092
VanderPlas J., Connolly A. J., Ivezić Ž., Gray A., 2012, in 2012 Conference on Intelligent Data Understanding. Princeton Univ. Press, p. 47
Virtanen P. et al., 2020, Nat. Methods, 17, 261
Vogelsberger M., Sijacki D., Kereš D., Springel V., Hernquist L., 2012, MNRAS, 425, 3024
Vogelsberger M., Genel S., Sijacki D., Torrey P., Springel V., Hernquist L., 2013, MNRAS, 436, 3031
Vogelsberger M. et al., 2014a, MNRAS, 444, 1518
Vogelsberger M. et al., 2014b, Nature, 509, 177
Vogelsberger M., Marinacci F., Torrey P., Puchwein E., 2020, Nat. Rev. Phys., 2, 42
Wadsley J. W., Stadel J., Quinn T., 2004, New Astron., 9, 137
Wadsley J. W., Keller B. W., Quinn T. R., 2017, MNRAS, 471, 2357
Walt S. V. D., Colbert S. C., Varoquaux G., 2011, Comput. Sci. Eng., 13, 22
Wang E., Lilly S. J., 2020a, ApJ, 895, 25
Wang E., Lilly S. J., 2020b, ApJ, 892, 87
Wechsler R. H., Tinker J. L., 2018, ARA&A, 56, 435
Weinberger R. et al., 2017, MNRAS, 465, 3291
Weinberger R. et al., 2018, MNRAS, 479, 4056
Weisz D. R. et al., 2011a, ApJ, 739, 5
Weisz D. R. et al., 2011b, ApJ, 744, 44
Welch P., 1967, IEEE Trans. Audio Electroacoust., 15, 70
Whitaker K. E. et al., 2014, ApJ, 795, 104
White S. D., Rees M. J., 1978, MNRAS, 183, 341
Wong T., Blitz L., 2002, ApJ, 569, 157
Woo J. et al., 2012, MNRAS, 428, 3306
Wright R. J., Lagos C. d. P., Davies L. J., Power C., Trayford J. W., Wong O. I., 2019, MNRAS, 487, 3740
Yung L. Y. A., Somerville R. S., Finkelstein S. L., Popping G., Davé R., 2019, MNRAS, 483, 2983
Zanella A. et al., 2019, MNRAS, 489, 2792
Zolotov A. et al., 2012, ApJ, 761, 71
Zolotov A. et al., 2015, MNRAS, 450, 2327

APPENDIX A: FINDING THE SHORTEST TIME-SCALES THAT CAN BE PROBED IN HYDRODYNAMICAL SIMULATIONS

Hydrodynamical simulations, both cosmological (Illustris, TNG, Mufasa, Simba) and zoom (FIRE-2, g14 and Marvel/Justice League), have limits on the lowest SFR possible in any given time bin that is set by the mass of the star particles they use in our archaeological approach. All the simulations listed above turn gas into a star particle probabilistically depending on whether certain temperature and density conditions are met. In practice, this introduces portions in the SFH where the SFR = 0, punctuated by small spikes which contain $\mathcal{O}(1)$ star particles. The effect of this on the power spectrum is to introduce white noise on the time-scales where the SFR is probabilistically populated by discrete star particles. Looking at the PSD of individual galaxies, we see the effects of this effectively Poisson-distributed 'shot-noise' as a flattening as we approach short time-scales. This depends on the amount of time the SFH spends in the vicinity of the minimum SFR threshold, set by

$$\langle \mathrm{SFR}_{\mathrm{min}} \rangle = \langle M_{*,\mathrm{sp}} \rangle / t_{\mathrm{PSD}}, \tag{A1}$$

where $M_{*,\mathrm{sp}}$ is the average stellar mass of the star particles in the simulation given in Table 1, and t_{PSD} is the time-scale being probed. From this relation, we see that the effects of shot-noise on the PSD are greater on short time-scales, as well as for simulations that have more massive star particles. However, finding the amount of time SFHs at a given stellar mass spend below $\mathrm{SFR}_{\mathrm{min}}$ is a nontrivial task, depending on the shape of the SFH itself, and the number of the fluctuations around the median shape that could take it below $\mathrm{SFR}_{\mathrm{min}}$.

In the simplest case, given an SFH that is simply a constant $\mathrm{SFR}_{\mathrm{const}} = \psi_{\mathrm{mean}}$+stochastic fluctuations $\mathrm{SFR}_{\mathrm{fluct}} = (N(0, \psi_\sigma))$, the distribution of SFR(t) at any given time is simply given by a Gaussian $N(\psi_{\mathrm{mean}}, \psi_\sigma)$. $\psi_{\mathrm{mean}} = M_*/\tau_{\mathrm{H}}$ is set by the stellar mass of the galaxy, where τ_{H} is the age of the universe at the epoch of

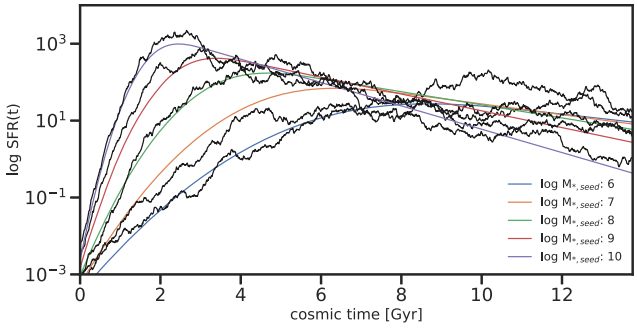

Figure A1. Generating SFHs for validation. For each test, we generate mock SFHs that follow the SFR–M_* correlation from Schreiber et al. (2015) following the procedure in Ciesla et al. (2017) corresponding to different seed masses. We then realize physically motivated SFHs as perturbations around these smooth curves with a spectral slope of 2 and a scatter of ≈0.3 dex.

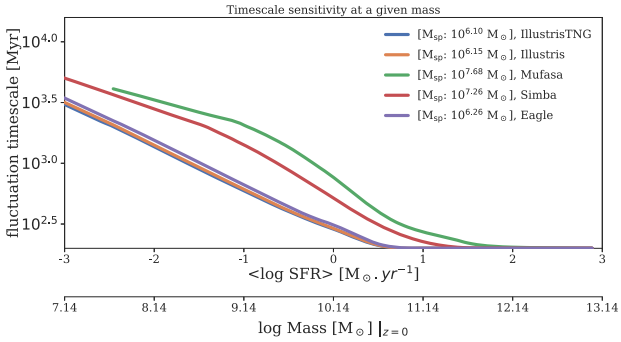

Figure A2. The lowest time-scales we can probe as a function of stellar mass for galaxies from the different hydrodynamical simulations we consider. For each SFH realized using the procedure described in Fig. A1, we introduce shot-noise proportional to the mass of the star particles for the different models. By comparing the pristine PSD to the PSD with shot-noise, we determine the loss of sensitivity in the PSD as a function of lifetime averaged SFR and stellar mass at $z = 0$.

interest. The amount of time any SFH at a given stellar mass spends below a threshold SFR is then given by

$$t(\mathrm{SFR} < \mathrm{SFR_{min}}|M_*, z) = \tau_\mathrm{H} \int_{-\infty}^{\mathrm{SFRmin}} \exp\left(-\frac{(\mathrm{SFR}-\psi_\mathrm{mean})^2}{(\psi_\sigma)^2}\right) \mathrm{dSFR} = \frac{\tau_\mathrm{H}\psi_\sigma\sqrt{\pi}}{2}\left(1+\mathrm{erf}\left[\frac{M_{*,\mathrm{sp}}/t_\mathrm{PSD} - M_*/\tau_\mathrm{H}}{\psi_\sigma}\right]\right).$$

Using this, we can set a threshold on the amount of shot-noise, and limit our analysis to time-scales above that.

Realistic SFHs are more complicated, however. From the evolution of the SFR–M_* correlation and the cosmic SFRD, we know that SFHs tend to rise at high redshifts and plateau or fall at low redshifts. From our simulations, we also see that on long time-scales the SFH perturbations can be described as a nontrivial power law (PSD(f) $\propto f^{-2}$). We therefore consider the case where the median SFH is not stationary, generating median SFH curves for galaxies of different stellar masses using the procedure described in Ciesla, Elbaz & Fensch (2017). To this, we add perturbations of ∼0.3 dex with a spectral power-law slope of 2, to create an ensemble of 10 000 mock SFHs. Examples of such SFHs are shown in Fig. A1. We also repeat our analysis for the cases where the power-law slope is 1–3, finding no significant difference in our results.

Using these mock SFHs, we model the effects of discrete star particles in the same way as the simulations. To do this, we discretize the mock SFH by rounding the SFR in each time bin to its nearest number of star particles, and consider the excess as the gas probability that a star particle will be formed in that time bin. Star particles are then added to each bin using a random draw with that probability.

We then compute the power spectra for these SFHs before and after the discretization procedure and quantify the time-scale at which the divergence from the original PSD exceeds a certain threshold (here 0.3 dex in PSD space). We also tried fitting the PSD corresponding to the discretized SFH with a broken power law to quantify the time-scale at which the transition from $\alpha = 2$ to white noise ($\alpha = 0$) happens, and find that our results do not significantly change. Based on these numerical experiments, Fig. A2 shows the thresholds for each simulation. For all cases, the figures can be read in two ways:

(i) Read horizontally, the figures give the minimum time-scale to which we can study the PSDs for galaxies in a given stellar mass bin at a particular epoch. These have been used to set the thresholds in Fig. 5.

(ii) Read vertically, the figures give the minimum SFR (and therefore the minimum stellar mass) needed to probe a certain time-scale or regime of the PSDs of galaxies.

Below these stellar masses (and time-scales) the effects of discretization of the star particles begins to dominate the SFRs, and thus the PSDs.

APPENDIX B: SFH DIVERSITY ACROSS MODELS

Fig. B1 shows five randomly chosen SFHs from each model across a range of stellar masses. Mufasa and Simba are shown above $10^{10}\mathrm{M}_\odot$ due to resolution limits, corresponding to the rest of the analysis in this work. As seen from their PSDs, the SFHs of these galaxies show a wide range of diversity in the strength of fluctuations on different time-scales. The SFHs of lowest stellar mass galaxies from the hydrodynamical simulations often show shot-noise due to discrete star particles. However, this noise mostly affects the PSDs on short time-scales, which is computed in Appendix A and accounted for while analysing their PSDs.

Fig. B2 shows distributions of the stellar masses, specific SFRs, and SFH shape parameters t_{50} and ($t_{75} - t_{25}$) as well as their covariances for the various large-volume galaxy evolution models we consider. t_{50} is defined as the cosmic time in Gyr at which a galaxy forms half of its total mass in stars, and $t_{75} - t_{25}$ is the amount of time taken by the galaxy to go from having formed 25 per cent of its total mass to 75 per cent of its total mass. The zoom simulations do not contain enough points to robustly sample a distribution and therefore are not shown.

The mass-versus-sSFR plots show a variety of slopes for the SFS, ranging from roughly linear for IllustrisTNG, Illustris, EAGLE, and the SC-SAM to sub-linear for Mufasa, Simba, and UniverseMachine. UniverseMachine in particular shows a remarkably strong quiescent population, in contrast with some models. It should be noted that the sSFR is computed using the number of star particles formed within the last 100 Myr, and might differ from the gas-based SFR. This effect is especially important for Simba and Mufasa, whose lower resolution decreases the probability that a star particle is formed in the last 100 Myr, leading to a much higher fraction of galaxies with sSFR hitting the lower boundary.

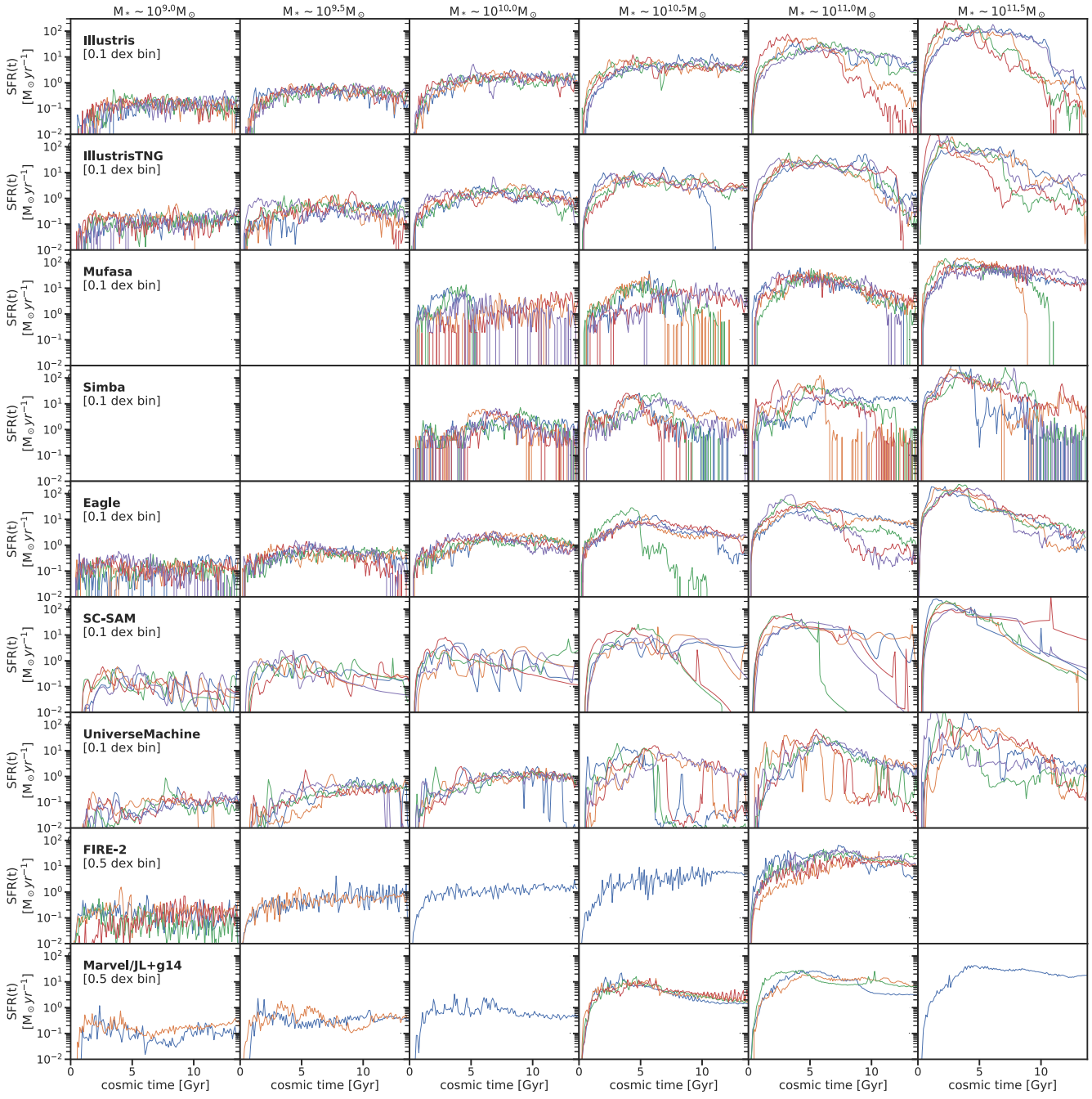

Figure B1. Representative SFHs from each model we consider across a range of stellar masses. For each model, we pick five SFHs randomly from galaxies that have stellar masses within 0.05 dex (0.25 dex for the zoom simulations) of the stellar masses reported at the top of each column. The panels display a large range of diversity in SFHs across mass, and among the different models.

The t_{50} quantifies the time in Gyr at which a galaxy formed half its total mass. A small value for t_{50} therefore indicates that the galaxy formed most of its mass at high redshifts. In conjunction with this, the $(t_{75} - t_{25})$ is the amount of time during which the galaxy formed the middle 50 per cent of its total mass, and serves as a proxy for the width of the period during which the galaxy was star forming. Although stellar masses and sSFR distributions among most models are similar, the distributions of t_{50} and $(t_{75} - t_{25})$, which can now be observationally constrained through SED fitting (Iyer et al. 2019), vary significantly. It is interesting to note that most simulations have a tail of populations with low t_{50}, usually corresponding to massive quiescent galaxies that formed most of their stellar mass in a short burst of star formation, as evidenced by the correlations between t_{50} and mass, sSFR, and $(t_{75} - t_{25})$. Massive late bloomer galaxies as found by Dressler, Kelson & Abramson (2018) at $0.4 < z < 0.7$, which formed most of their mass in the last $\sim$1.5 Gyr, thus do not feature prominently in any of these models.

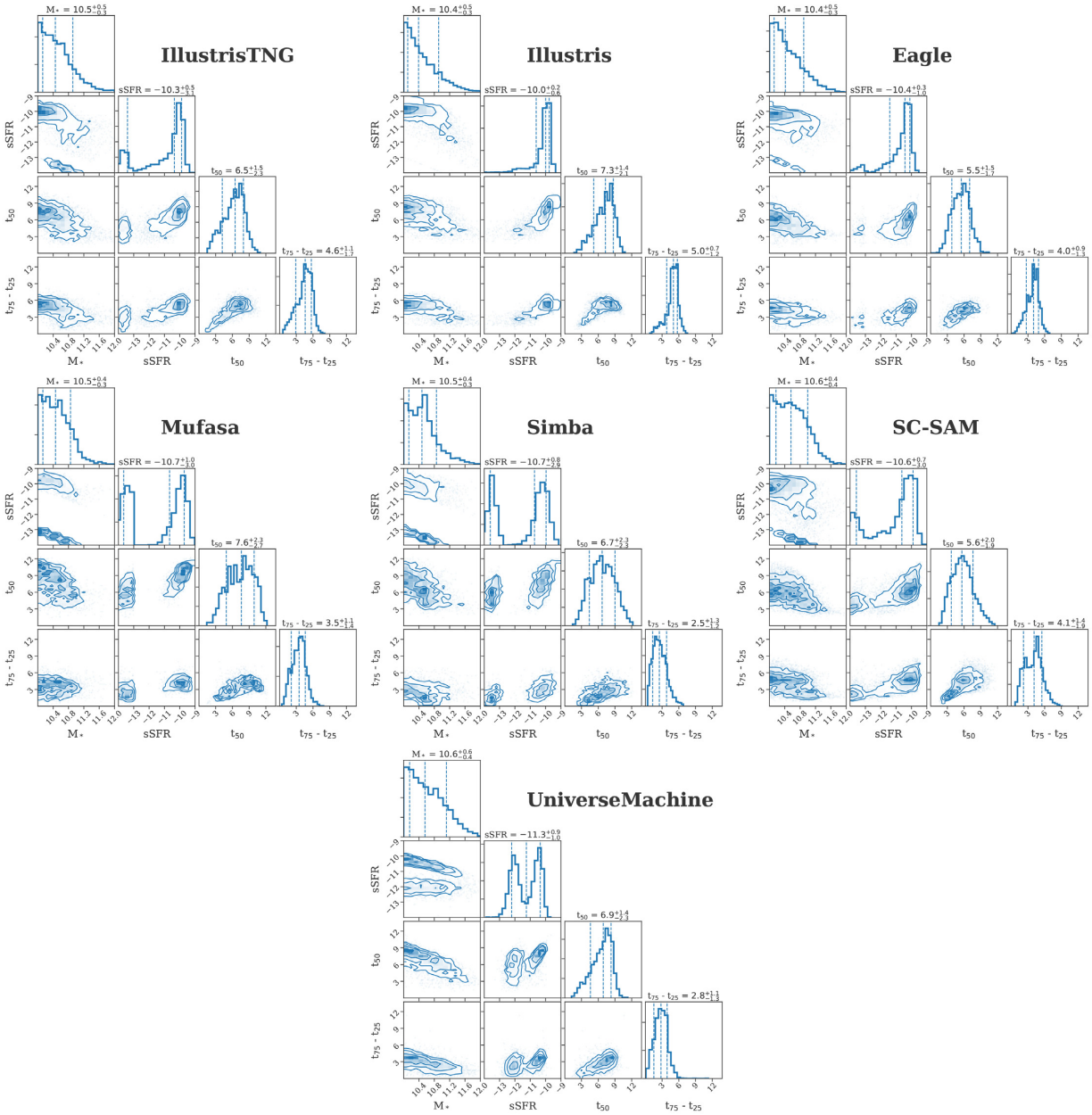

Figure B2. Distributions of SFH parameters at $z \sim 0$ for the different galaxy evolution models under consideration. The four histograms of the corner plot (Foreman-Mackey 2016) show the distribution for log Stellar Mass (M_*, [$M_\odot$]), log specific SFR (sSFR, yr^{-1}), the half-mass time (t_{50}, [Gyr]), and the width of the galaxy's star-forming period ($t_{25} - t_{75}$, [Gyr]). The remaining panels show the covariances between the different quantities. The numbers above each column show the median and 16–84th percentile values for each quantity across the various models.

APPENDIX C: ESTIMATES OF TIME-SCALES IN THE LITERATURE

Table C1 reports the estimated time-scales for physical processes from current literature used in the rest of this paper and for generating the time-scale ranges shown in Fig. 1.

Table C1. A summary of time-scales estimated in different simulations and analytical models, assuming $\tau_{\rm H} \approx 10$ Gyr at $z \sim 0$ where time-scales are reported in terms of the Hubble time.

Physical process	Time-scale range	Reference
SNe, cosmic rays, photoionization from Starburst99	4−20 Myr	Leitherer et al. (1999)
GMC lifetimes	∼5−7 Myr	Benincasa et al. (2020)
Molecular cloud formation time-scale	$\mathcal{O}(10)$ Myr	Dobbs et al. (2012, 2015)
Turbulent crossing time	∼10−30 Myr	Semenov et al. (2017)
Free-fall time at mean density	∼10−50 Myr	Semenov et al. (2017)
Molecular cloud collision time-scales	≤20 Myr	Tan (2000)
Cycling of ISM gas between SF regions and ISM	∼20−100 Myr	Semenov et al. (2017)
GMC lifetimes (MW-like discs)	≤20 Myr	Tasker (2011)
Bursty SF in TIGRESS	∼45 Myr	Kim & Ostriker (2017)
Molecular gas encounters spiral arms (MW like)	∼50−100 Myr	Semenov et al. (2017)
Galactic winds affecting ISM	∼50−200 Myr	Marcolini et al. (2004)
Galaxy wide gas depletion time-scales	∼2−10 Gyr	Semenov et al. (2017)
Local gas depletion time-scales (SF regions)	∼40−500 Myr	Semenov et al. (2017)
Exponential growth of B field	∼50−350 Myr	Pakmor et al. (2017)
Merger induced starburst	∼90−450 Myr	Robertson et al. (2006b)
Starburst time-scale after major merger	∼90−570 Myr	Cox et al. (2008)
Rapid fluctuations of inflow rates in FIRE	$\lesssim$100 Myr	Hung et al. (2019)
Exponential growth of B field	∼100 Myr	Hanasz et al. (2004)
Fast quenching in Simba	$\sim 0.01\tau_H \approx 100$ Myr	Rodríguez Montero et al. (2019)
AGN feedback time-scale	$\lesssim$0.2 Gyr	Kaviraj et al. (2011)
Recycling time-scale	$\propto M_{\rm halo}^{-1/2} \sim 300$ Myr to 3 Gyr	Oppenheimer et al. (2010)
Crossing time	∼300 Myr to 1 Gyr	Bothun (1998)
Median recycling time-scale (with large dispersion)	∼350 Myr	Anglés-Alcázar et al. (2017a)
Mean depletion time	∼470−490 Myr	Tacchella et al. (2016)
Recycling time-scale	$\propto M_*^{-0.19} \sim 400$ Myr to 1 Gyr	Mitra et al. (2016)
Exponential growth of B field (gas disc)	∼500−800 Myr	Khoperskov & Khrapov (2018)
Enhanced SF after merger (IllustrisTNG)	∼500 Myr	Hani et al. (2020)
Median recycling time-scale (galactic fountains)	∼500 Myr	Grand et al. (2019)
Halo dynamical time-scale	$\sim 0.1\tau_H \approx 0.5$−2 Gyr	Torrey et al. (2018)
Morphological transformations in IllustrisTNG	∼500 Myr to 4 Gyr	Joshi et al. (2020)
Galaxy mergers (fitting formula)	∼500 Myr to 10 Gyr	Jiang et al. (2008)
Effective viscous time-scale	$\approx$600 Myr $f_g^{2/3} R_{10} V_{200}^{-1} \dot{M}_{*,100}^{2/3}$	Krumholz & Burkert (2010)
Morphological transformation – quenching delay	∼0.5 Gyr (gas rich), ∼1.5 Gyr (gas poor)	Joshi et al. (2020)
Quenching in IllustrisTNG (colour-transition time-scale)	∼700 Myr to 3.8 Gyr	Nelson et al. (2018b)
Recycling time-scale (half the outflow mass)	∼1 Gyr	Christensen et al. (2016)
Slow quenching in Simba	$\sim 0.1\tau_H \approx 1$ Gyr	Rodríguez Montero et al. (2019)
Merger time-scales (VELA)	$\mathcal{O}(1)$ Gyr	Lotz et al. (2011)
Metallicity evolution time-scale ($z \sim 0$)	∼1.8 to 2.2 Gyr	Torrey et al. (2018)
Recycling times (weak feedback)	up to ∼3 Gyr	Übler et al. (2014)
Merger time-scales (dynamical friction)	∼(1−10) Gyr	Boylan-Kolchin et al. (2008)
Oscillations around the SFMS	~ 0.2−$0.5\tau_H \approx 2$−5 Gyr	Tacchella et al. (2016)
Quenching in Illustris (satellites)	∼2−5 Gyr	Sales et al. (2015)
Quenching in EAGLE	∼2.5−3.3 Gyr, extending out to τ_H	Wright et al. (2019)
Recycling times (strong feedback)	up to ∼11 Gyr	Übler et al. (2014)

This paper has been typeset from a TEX/LATEX file prepared by the author.